Bayesian Nonlinear Finite Element Model Updating of Bridge Columns considering Bond-slip and Rebar Buckling using Experimental and Simulated Data

by

Zhenning Liu

A thesis submitted in partial fulfillment of the requirements for the degree of

Master of Science

in

STRUCTURAL ENGINEERING

Department of Civil and Environmental Engineering
University of Alberta

ABSTRACT

Reinforced concrete (RC) bridges are key elements in modern transportation system. Therefore, the serviceability and safety of such structures after earthquakes have become an area of great interest. Developing an accurate FE model that is capable of representing the important mechanics of RC structures subjected to earthquakes is important, for example, in post-event damage assessment. In particular, an updated FE model based on recorded response of an instrumented structure during an earthquake can be used to infer the hidden damage structures experienced. Among various finite element model updating (FEMU) strategies, Bayesian parameter inference (e.g., unscented Kalman filter approach) has been well received in the past decades.

This study focused on the Bayesian nonlinear FEMU of a shake-table tested full-scale RC bridge column, with particular emphasis on learning advanced modeling aspects (e.g., bond-slip and steel rebar buckling). Using prior knowledge about the design information of the column, a nonlinear fiber-based finite element model was developed in the open-source FE software framework (*OpenSees*). Due to the unknown/uncertain modeling aspects, the initially developed FE model was inaccurate. It was found that the perfect bonding assumption was inappropriate, and bond-slip needed to be taken into account. Furthermore, the dynamic response data from the shake-table tests were utilized for the nonlinear FEMU to help achieve an accurate prediction on the structural behavior. Potential parameters for updating were selected by combining the in-site observations and relative importance of the model parameters, which were determined through a comprehensive sensitive analysis. The credibility of the updated model was validated by comparing FE predictions with the experimental measurements during each ground motion, in both local (i.e. strain) and global (i.e. drift ratio) scale. Moreover, damage evolution of the RC bridge column in a sequence of earthquake ground motions were also studied. The update results affirmed that the nonlinear FEMU was capable of identifying multiple unknown/uncertain modeling aspects (e.g., bond-slip related parameters) from experimental observations and showed that stochastic FEMU approach was capable of enhancing the modeling accuracy with measurements.

Considering that the RC column expressed steel rebar buckling in the shake-table test, the buckling effect of steel rebar was further introduced into the FE model. Thus, this study also applied the

FEMU approach to RC bridge columns considering both bond-slip and steel rebar buckling. With different steel material models available to incorporate the asymmetrical behavior due to steel rebar buckling, material coupon test data collected from the literature were used to assess their material model performance. With the most versatile buckling steel material model, the FE model considering both bond-slip and steel rebar buckling was used to simulate noisy seismic response data considering measurement error. Nonlinear FEMU was then conducted to examine the capability of the nonlinear FEMU approach in learning the buckling-related modeling parameters in addition to other unknown parameters (e.g., bond-slip parameters). The FEMU results have proven that the stochastic FEMU approach was capable of identifying buckling related parameters based on recorded seismic response data. This implies its potential applications for post-event damage assessment.

ACKNOWLDEGEMENTS

Foremost, I would like to express my sincere gratitude to my supervisor, Dr. Yong Li, who guided me throughout this project. His patience, guidance, enthusiasm, and invaluable knowledge have been the most valuable fortune throughout my graduate program. He set a perfect exemplar of a professional scholar and an engineer. What I have learnt from him in the past two and half years will benefit me for the rest of my life.

I am deeply grateful to my colleague, Shaghayegh Abtahi, who provided me valuable technical support. Her meticulous comments on my research were an enormous help to me go over the obstacles throughout my program. My special thanks also go to Dr. Rodrigo Astroza from Universidad de los Andes, in Chile, for providing me valuable suggestions on my research topic. Additionally, I would like to acknowledge the financial support through NSERC Discovery Grant, which makes this study possible.

I would like to thank my friends, Vahab Esmaeili, Mehrdad Palizi, and Saher Attia and others, for all the fun we have had in the past two years. It is my honor to be accompanied with such a group of inspiring and knowledgeable people. Lastly, I owe my deepest gratitude to the members of my family. They are the role models in both scientific research and life in general and my strongest backup that encouraged me going through all the difficulties in the past.

TABLE OF CONTENTS

LIST OF TABLES

LIST OF FIGURES

CHAPTER 1: INTRODUCTION

1.1 Background

Reinforced concrete (RC) bridges play an important role as part of the modern transportation system, and thus their serviceability and safety are critical for social and economical development. However, RC bridges are vulnerable during destructive earthquakes. As reported in the post hazard assessment from historical earthquakes, various damage and failure modes can be observed in different bridge structural components (i.e. bearings, girders, expansion joins, bridge pier columns, abutments) [1]. Among these damage or failure modes, the failure in bridge pier columns is among the most common ones observed from historical events [2] [3]. As shown in Figure 1-1, the failure of a bridge column often arises with spalling on the cover concrete, crushing of the core concrete, as well as the buckling of the longitudinal reinforcement and potential bond-slip at the bottom of RC columns. It is worth mentioning that pier columns are more vulnerable in earthquakes than other components [4].

The post-hazard report from the 1995 Kobe earthquake has revealed that old RC bridges (e.g., built in 1960s and 1970s) are more vulnerable during destructive earthquakes [5]. In Canada, aging of bridges is becoming a concern, because many bridges are built in the last century. For example, in Quebec, more than 75% of the bridges are more than 30 years old [6] and are approaching their design life. As such, it is important to have analytical tools for post-hazard evaluation for bridge structures, which can be achieved by using seismic responses recorded during earthquakes. To this end, developing an appropriate analytical model, such as accurate nonlinear finite element (FE) models that are capable of representing the true state or condition of bridge structures, is highly needed.

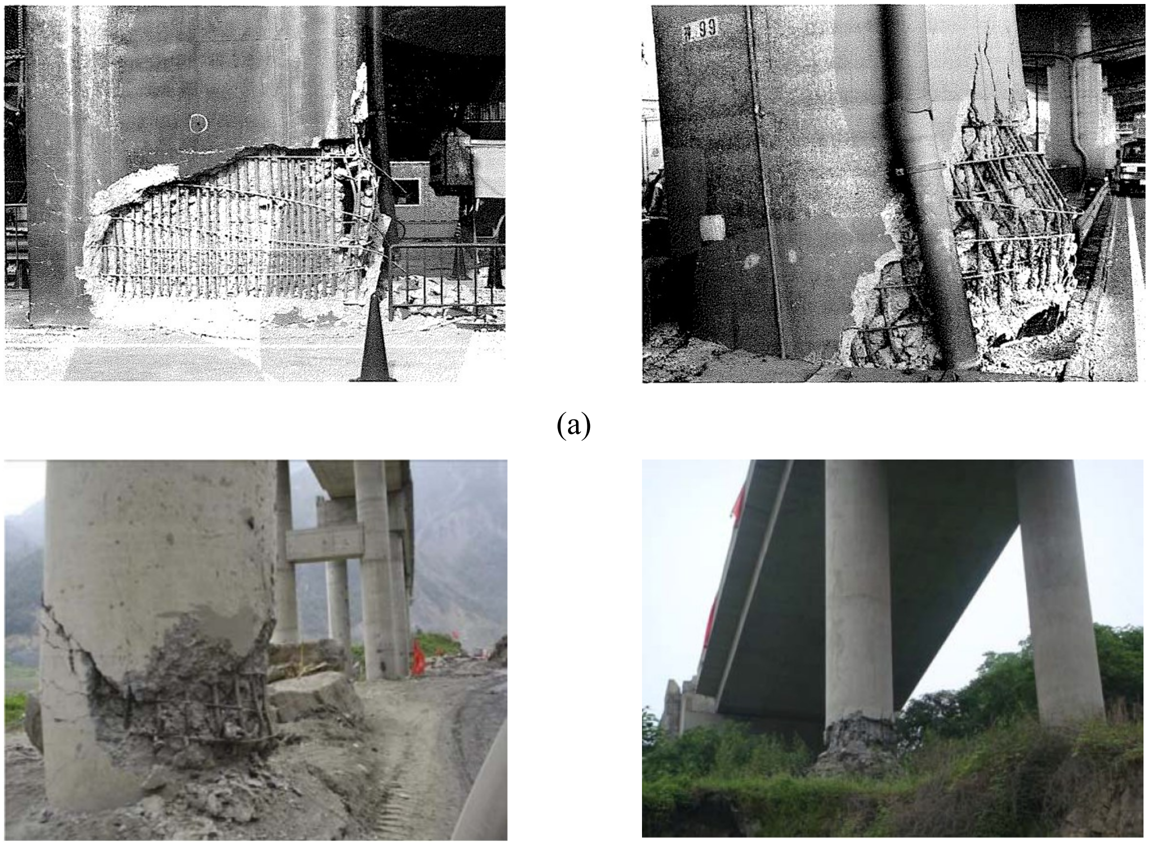
(a)

(b)

Figure 1-1: Photos of the damaged bridge pier columns from (a) Kobe earthquake 1995 [5], and (b) Wenchuan earthquake, 2008 [1]

1.2 Problem statement and motivation

The unknown modeling aspects, especially the advanced modeling aspects such as bond-slip and steel rebar buckling, complicate the process of developing accurate models that can be used to reconstruct or reproduce the bridge column response during earthquakes. Thus, the major problem addressed in this thesis is to identify or estimate the unknown or uncertain model parameters in the development of FE models using seismic response data. A common practice to tackle this problem is to utilize empirical equations to approximate the unknown modeling parameters. Such an approach highly relies on the historical studies on the behavior of a certain material under very specific circumstances, and the resulted model can rarely represent the real structural system well, especially when observation noise exists in the measurements. Therefore, an inverse FE modelling process, known as nonlinear finite element model updating (FEMU), is needed. FEMU is more commonly confronted in the field of structural health monitoring where more unknown aspects need to be explored. In this thesis, stochastic Bayesian filtering (e.g., unscented Kalman filtering), which have proved to be an alternative approach to estimating modeling parameters (e.g., steel or concrete material parameters), is used to study the advanced modeling aspects (i.e., bond-slip and rebar buckling) of RC columns using experimental and simulated seismic data.

The RC bridge column studied in this thesis is a full-scale bridge pier column tested on the shake-table located in University of California, San Diego, in 2015. The test specimen was subjected to 10 ground motion (GM) acceleration series in a sequential manner. During the experiment, the column showed complex physical behavior such as the concrete crushing, bond-slip, steel rebar buckling, etc. The seismic response of this bridge column was well recorded via densely arranged sensors. Those experimental data contained valuable information on the behavior of RC column under sequential destructive ground motions and provided a solid basis for the finite element model updating as presented in this thesis.

1.3 Objectives and methodology

The overall objective for this study is to perform finite element model updating to obtain accurate FE models of the shake-table tested bridge column studied in this research project, by performing finite element model updating that integrating an FE software framework *OpenSees* [7] with the stochastic Bayesian inference approach. Since the shake-table test of the RC column revealed the importance of the bond-slip effect and the buckling failure mode of the reinforcing steel under strong earthquakes, these two modeling aspects are considered instead of assuming perfect bonding and non-buckling for steel rebars as in the conventional modeling of RC columns. This could further break down into two sub-objectives: nonlinear FE modeling and updating of the model when (1) considering bond-slip and (2) considering bond-slip and rebar buckling simultaneously. The sub-objective (1) is focused on the GMs with relatively low intensities, where the buckling effect of steel is absent while the bond-slip effect presents. In contrast, the sub-objective (2) is to focus on the GMs with relatively high intensities, where both bond-slip and buckling effect are considered.

For the subobjective (1), the potential parameters for updating are selected by combining the information from in-site material coupon tests and relative importance of the model parameters, which are determined through a comprehensive sensitive analysis. The dynamic response data from the shake-table tests are then utilized for the FE model updating to help achieve an accurate prediction on the structural behavior. Since the model updating in this group is performed based on experimental data, the credibility of the updated model should be verified by different measurements. Note that the experimental data were collected under a sequence of seismic loading, and pre-existing damage accumulated from earlier earthquake GMs will naturally change the structure states for a certain GM and complicate the nonlinear FE model updating.

For the sub-objective (2), more focus is placed on the modeling of the buckling effect of the steel. To fulfill the requirement of the model updating, where a robust and accurate material model is necessary to account for the buckling effect, a detailed study is first performed on the different buckling steel material models under different buckling levels to assist the material model and parameter selection. Furthermore, nonlinear FEMU is conducted using noisy seismic data simulated to examine the capability of the finite element model updating approach in learning the buckling-related modeling parameters in addition to other unknown parameters (e.g., bond-slip parameters).

To achieve the goal of this research with the aforementioned methodology, the research tasks are presented as follows:

1. Perform a literature review on the previous studies for the modeling of the RC columns (with or without considering bond-slip and steel rebar buckling) and the nonlinear FE model updating strategies;

2. Establish a robust and effective FE model updating framework that combines the stochastic Bayesian inference method and the nonlinear finite element modeling tool (i.e., *OpenSees*);

3. Conduct nonlinear FE model updating when considering bond-slip for the bridge column subjected to GMs with relatively low intensities using experimental data. Additionally,

comprehensive parametric analyses on the modeling parameters and damage evolution analysis of the column during the tests are studied;

4. Assess the performance of different buckling steel material models commonly used in the literature based on experimental data of material coupon tests using the stochastic Bayesian inference approach;

5. Conduct nonlinear FE model updating when considering buckling behaviour of steel rebars for the bridge column subjected to GMs with relatively high intensities using simulated data with noise and verify the ability of model updating approach on identifying the buckling-related parameters.

1.4 Organization of thesis

This thesis consists of six chapters as follows:

- Chapter 1 provides the general information of the background, problem statement, motivation, objectives, methodology, and specific tasks of this research.
- Chapter 2 provides a literature review on the related experimental and modeling aspects of RC columns, as well as different approaches on the finite element model updating.
- Chapter 3 describes the framework of the finite element model updating approach used in this study and investigations into the analysis efficiency of the approach.
- Chapter 4 presents the finite model updating for the bridge column with bond-slip considered using the experimental data collected during GM1, GM2, GM3, and GM4, following a local sensitivity analysis to reveal the relative importance of various modeling parameters.
- Chapter 5 presents a performance comparison among different buckling steel material models, and nonlinear FE model updating for the bridge column with both bond-slip and buckling steel considered using the simulated data.
- Chapter 6 summarizes the conclusion of this study and recommendations for the future research.

CHAPTER 2: LITERATURE REVIEW

2.1 FE modeling of RC bridge pier columns

Complementary to experimental testing, finite element (FE) analysis is a widely adopted approach to gain a deeper understanding of the mechanical behavior of structures. For example, a FE model, which is capable of reproducing the experimental measurements during either static or dynamic tests in the field or laboratory, can be serve as a digital twin of the physical structure. Three-dimensional (3D) continuum elements are commonly adopted for modeling large-scale RC structures. Such elements can work together with sophisticated constitutive material models to represent the mechanics of structures. Such an approach can be found in many applications (e.g., [8] [9] [10]).

However, FE analysis with 3D continuum elements is usually accompanied with high computational cost, as the number of degree-of-freedom (DOF) increases exponentially with the mesh refinement. As such, to reduce the computational cost and simplify the element formulation, Kaba and Mahin [11] introduced a refined modeling approach for the RC columns and frames. In this study, a section-node-element relationship was established for modeling columns and frame structures, where a multi-slice fiber model was proposed to represent the physical aspects of structural members. This approach integrated the mechanical behavior of concrete and steel in a fiber section that was assigned to each integration point in one element. Such a fiber-based element showed its ability of representing the physical behavior of frame structures accurately with significantly limited degree of freedom. This type of fiber-based beam-column elements are now available in an open-source finite element software framework (*OpenSees*) and are well received in the literature.

As an example, Sadrossadat et al. [12] used the fiber-based modeling strategy to model the experimentally tested 4-span bridge structure. By comparing the FE model prediction with the experimental data, the authors concluded that the analytical model predicted the measured response with reasonable accuracy and affirmed the effectiveness of the fiber-based model in modeling RC frame-type structures. Lee and Billington [13] utilized the fiber-based FE modeling approach to study the dynamic behavior of a shake-table tested RC bridge pier column. The author compared the drift ratio of the column recorded during the experiment test with the FE model prediction and found that the FE model achieved an accurate representation of both local and global behavior of the column.

As can be observed from the literature where the fiber-based FE modeling strategy was used, this approach has a low computation cost due to the low number of degree-of-freedom. However, many of the studies such as Kaba and Mahin [11] revealed the limitations of the fiber-based modeling approach, such as its incapability of considering bond-slip due to the plain-section assumption (i.e., fibers at the same section assumed to remain in plane throughout the analysis). In order to take advantage of this modeling approach, special techniques need to be used to enhance the fiber-based FE models for RC columns.

2.1.1 Uniaxial concrete material models

Different formulations were developed for the uniaxial stress-strain behavior of concrete and the Kent-Scott-Park concrete model [14] is among the most widely adopted formulations. The compression backbone curve of Kent-Scott-Park concrete model combines three major segments: a parabolic hardening branch, a linear softening branch, and a constant crushing branch, as shown in Figure 2-1 (a). This relatively simple model only requires four parameters to define its compression envelope, including the compressive strength ($f_c{}'$), the concrete strain at peak strength (ε_c), the concrete crushing strength (f_{cu}'), and crushing strain (ε_{cu}). Later modification on this formulation (i.e. *Concrete01* in *OpenSees*, see Figure 2-1 a) with degraded linear unloading/reloading stiffness as per Karsan and Jirsa [15] and no tensile strength enables a more accurate representation of the cover concrete behavior. To improve the representation of cyclic behavior and the tensile behavior of the confined concrete (e.g., concrete core), *Concrete02* is introduced in *OpenSees* with reference to Mohd and Yassin [16], see Figure 2-1 (b).

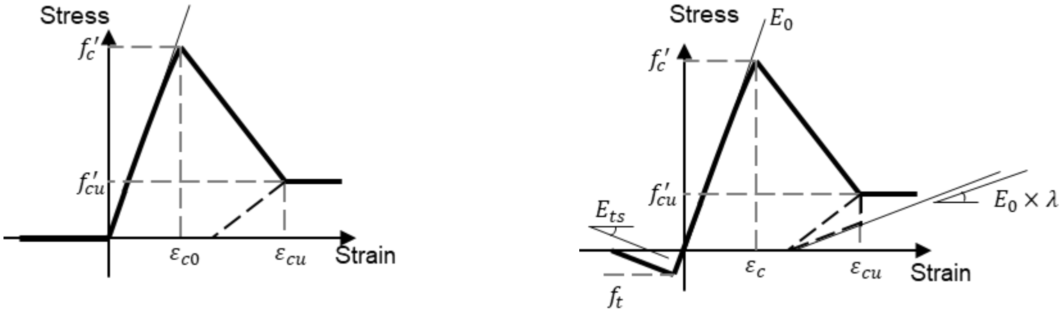

(a) (b)

Figure 2-1: Stress-strain relationship for (a) *Concrete01* in *OpenSees*, and (b) *Concrete02* in *OpenSees*

Compared with unconfined concrete, confined concrete in the core of RC column has a much higher strength and ductility. However, direct measurement of the physical properties of the confined concrete inside RC columns is difficult and thus the stress-strain relationship is usually obtained indirectly based on Mander et al. [17]. They developed an empirical relationship for the material properties between the unconfined and the confined concrete. As summarized in this study, the compressive strength, the concrete strain at peak strength, the concrete crushing strain, and the crushing strength can be approximated by empirical formulas that can take the confinement properties (stirrup spacing, confinement area, etc.) into consideration. The effectiveness of the proposed formulation was verified by the author, since a great correlation was observed between the material prediction and an experimental test on RC column conducted by Mander et al. in 1988 [18]. However, the accuracy of the empirical predictions is not guaranteed, and it could affect the accuracy of the FE prediction of concrete structures.

2.1.2 Uniaxial steel material models with and without buckling effect

Among various uniaxial stress-strain models for steel, the Giuffré-Menegotto-Pinto (GMP) constitutive law is among the most widely used ones for the longitudinal steel rebars in RC structures. The formulation of the GMP steel model was first developed by Giuffrè [19] based on a set of steel coupon tests and was further improved by Menegotto and Pinto [20], enhancing the performance to achieve a better accuracy compared to other formulations such as Ramberg and Osgood developed in 1943 [21] as well as Dafalias and Popov developed in 1975 [22].

Furthermore, Filippou et al. [23] introduced isotropic hardening into the formulation, further improving the performance of the formulation under high-strain amplitudes.

However, the original GMP material formulation is not capable of representing the asymmetrical behavior, which is essential of modeling the buckling effect of steel rebars. In order to include the asymmetry behavior into the GMP steel, Monti and Nuti [24] developed an advanced steel material model that modified the compression backbone curve of the GMP model. The formulation of the compressive behavior was derived from the monotonic and cyclic steel tests conducted by Monti and Nuti in 1989 [35] and 1991 [36], which provided a detailed stress-strain relationship for steel rebars with different levels of buckling effect. Later comparison between the model prediction and experimental observations proved that the proposed model could deliver an accurate simulation of the uniaxial stress-strain for steel rebars under various levels of buckling.

Another buckling steel material model developed by Kashani et al. [25] had considered the buckling of the steel rebars with much higher slenderness ratios (i.e. specimen with *L/D* up to 20). The formulation of the compressive behavior of such a material model was derived based on the experiments conducted by the same author in 2013 [26]. The developed material also showed excellent accuracy on the inelastic buckling for low corrosion level. However, this model is not appropriate for steel rebars with low slenderness ratios.

2.1.3 Steel rebar bond-slip material models

The bond-slip effect, which refers to the relative displacement between the steel rebars and the surrounding concrete, is a common physical phenomenon for RC columns under cyclic loadings (i.e. earthquakes). The bond-slip effect is often neglected when modeling RC structures since perfect bonding between the concrete and steel is commonly assumed to reduce the complexity in the modeling. However, such an assumption is invalid for the RC structures under high-intensity earthquake ground motions; neglecting the bond-slip effect could result in overestimation of the column stiffness and lead to inappropriate engineering judgements [27].

Some early studies, such as the work by Ngo and Scordelis [28], modeled bond-slip using elastic spring elements, which were created to connect a node of a concrete element with a node of steel element with a constant stiffness. Such formulation was a simple representation of bond-slip and not capable of representing the stress-slip relationship when the stress on the contact surface between the concrete and the steel is high. In 1982, Eligehausen et al. [29] developed a more complicated stress-slip formulation based on a series of bar pull-out tests. This nonlinear stress-slip formulation was then introduced into the FE analysis by works such as Monti and Spacone [30]. In that study, the bond-slip effect was modelled within the plastic hinge zone and a nonlinear spring element was inserted between steel fibers and concrete fibers. They compared the FE predictions of the monotonic and cyclic behavior of the tested column with the experimental data and concluded that the implementation of the bond-slip modeling methodology improved the FE model prediction.

However, it is challenging to implement the nonlinear spring approach in fiber-section-based FE models, where a plane section is assumed to enforce the compatible deformation of steel rebars and concrete on the same plane section. To overcome such limitation, a different modeling approach is developed by Zhao and Sritharan [31], where the authors introduced a fixed-end rotational flexibility by integrating the local stress-slip relationship to address the bond-slip effect in RC structures (see Figure 2-2).

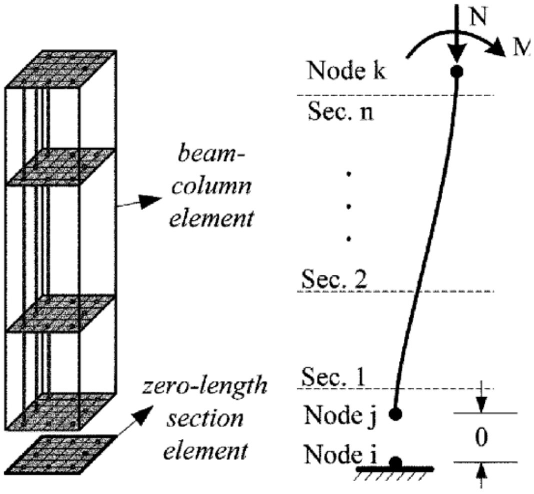

Figure 2-2: Modeling scheme of bond-slip using a zero-length section element [31]

In this approach, an additional zero-length section element was inserted at the end of RC members to represent the equivalent fix-end rotation contributed by bond-slip. The material model assigned to steel was defined by a steel model with bond-slip developed from series of bar pullout tests, and concrete material at that section are regularized with a perfectly plastic behavior. By comparing the FE predictions with the experimental measurements, the author concluded that this approach can successfully represent the mechanical behaviors of RC frame structures, including deflections, force versus displacement hysteresis responses, strains in the longitudinal steel rebar, and section curvatures.

2.2 Nonlinear finite element model updating

When developing a FE model that aimed to reproduce the physical aspects of an experimental tested structure, the uncertainties in the material parameter values are widely present and need to be properly addressed. For example, the value of many modeling parameters could not obtain directly from the experiment, which are evaluated from empirical equations or estimated by engineering judgements. Apart from that, direct use of the values obtained from the in-site material coupon tests, which contain the measurement error, also contributes to the uncertainty in the FE model prediction and greatly affects the modeling accuracy. Last but not the least, some model parameter values need to be adjusted to account for the model uncertainty (inaccuracy) as well. With the presence of such modeling uncertainties, FE models need to be updated to achieve accurate representation of structural systems. This is essentially an inverse FE modeling problem and can be solved by a FE model updating (FEMU) process. This problem is commonly confronted in the field of structural health monitoring, where nonlinear FEMU can be used to infer the damage-related parameters [32] for damage detection of civil structures.

The FEMU analysis takes advantage of both the prior knowledge about FE modeling and the structure response measurements to minimize the discrepancy between the FE prediction and the measured responses. Various FEMU approaches exist in the literature by utilizing different global or local optimization techniques. The global optimization methods, such as the genetic algorithm [33] and the simulated annealing [34], were successfully applied to problems of different complexity levels [35] [36] [37] [38]. The advantage of global optimization methods is the updating accuracy of certain approach is not sensitive to the initial guess of the parameters and a global optimum point can be guaranteed within the parameter threshold. However, global optimization methods require a large number of evaluations on the finite element model, making it significantly computational expensive for FEMU. To address such drawback, local optimization methods were used to reduce the computational at the risk of achieving a local minimum and is thus sensitive to the initial value. Some methods, such as the least-square error (LSE) algorithm, were used for the model updating [40] [43].

In the recent years, Kalman filtering (KF) developed by R.E. Kalman [40] is becoming one of the most popular approach for parameter estimation or FEMU problems. This approach is capable of combining the information contained in the historical observations and the model prediction of a dynamic system, and it is also capable of dealing with noisy observations and predictions. However, the original Kalman filter is limited to linear problems. To address this limitation, modified Kalman filters, such as extended Kalman filter (EKF) [41], unscented Kalman filter (UKF) [42], and particle filter (PF) [43], were developed and further expanded the application of KF into nonlinear systems.

Chatzi and Smyth [43] applied the PF approach to the parameter identification problems. This approach was verified by the author via two simple problems, including the parameter estimation of a nonlinear system defined by a numerical function and a three-mass damped system. The PF successfully identified the uncertain parameters of each nonlinear system. Xue et al. [44] applied APF (auxiliary particle filtering) to a structural damage detection problem, where a 2-story shear-beam building under seismic excitation was studied. The measurement used for FEMU was generated based on data simulated from a FE model and further polluted with artificial noise at various levels to account for the measurement error. They successfully identified all five unknown damage-related modeling parameters with excellent accuracy.

Foun [45] implemented EKF on system identification of linear and nonlinear structures subjected to acceleration excitations recorded from the El Centro earthquake. Like the majority of existing studies, observations used for the FEMU were generated by adding gaussian white noise to the simulated data. Sen and Bhattacharya [46] applied dual extended Kalman filter (DEKF) to parameter identification problems in the field of civil engineering. A 3D truss structure was artificial damaged by changing the material properties (i.e. elastic modulus) and dimensions of the cross-section (i.e. cross-sectional area) of truss members. The damage-related aspects were identified by the DEKF using the measurements.

As seen above, the PF can predict the unknown system parameters. However, as the PF uses the Monte Carlo sampling to approximate the probability density, the computational cost is high. On the other hand, the EKF requires much less computational effort compared to PF, but EKF usually has a low accuracy compared to PF particularly when the problem is strongly nonlinear. This is because EKF relies on first-order approximation of the system equations.

To reach a trade-off between accuracy and computational cost, the UKF has attracted significant interest in academia in recent years. Xie and Feng [47] have applied the UKF algorithm in system identification problem based on a civil structure system. This study considered a 1 degree-of-freedom (DOF) nonlinear system, a 2 DOF linear system, and a two-storey nonlinear elastic system. For each case, 5, 4, and 6 parameters were considered as unknown or uncertain. The measurement data was generated based on FE simulation and was polluted by an additive Gaussian white noise with root mean square (RMS) at 2% and 5% of the signal to account for the measurement error. The UKF successfully identified the unknown parameters of all three cases with different accuracy, showing the robustness of the UKF at different complexities.

More recently, Astroza et al. [48] performed system identification on much more complex civil structures under seismic loading. In this study, a three-dimensional 4-story 2-by-1 bay steel frame structure and a 5-story 2-by-1 bay reinforced concrete frame was studied. The UKF successfully identified the true values of all 6 unknown parameters for the steel frame and 9 unknown parameters for the RC frame. Furthermore, an excellent agreement between the unobserved local response recorded from the updated model and their counterparts in the true measurement was achieved, further verifying the credibility of the updated model.

By comparing the applications of different stochastic filtering methods (i.e., PF, EKF, and UKF) in the literature, the UKF is considered as more suitable for the FEMU of complex civil structures. However, the vast majority of the existing studies (i.e. [48]–[50]) focused on developing and verifying techniques for concerns of accuracy and efficiency, or challenges for high-dimensional parameter space [51]. Parameter-wise, the updated parameters in the majority of the FEMU cases are not carefully chosen in terms of the sensitivity and uncertainty, making the updating process less efficient. Furthermore, limited work has devoted to the use of nonlinear FEMU to study the advanced modeling aspects, e.g., the bond-slip effect and the steel buckling effect. Nevertheless, the advanced modeling aspect such as bond-slip was found to play a significant role in RC structures under extreme loadings, as evidenced by historical failure events and laboratory testing [13] [23]. In terms of the measurement data, one assumption inherent in many existing studies is that the prediction model is completely accurate so that the exact response can be associated with the correct model parameters. However, for the FE model aiming at reproducing the physical behavior of real-world structures, the model uncertainty is inevitable. As such, it is necessary to practice the nonlinear FEMU using the experimental data in the field or laboratory to explore the practicability of nonlinear FEMU approaches.

Shake-table testing is a widely practiced approach aiming to examine the mechanical behavior of structures under seismic excitations. Chen et al. [53] tested a four-span tall-pier bridge system on a shake-table, where the targeted structure was scaled down to 1/7 of its original dimension. The bridge system was then subjected with Rinaldi ground motion from the 1994 Northridge earthquake with different scaling factors. During the test, the structural response such as displacement, acceleration, and local strain histories were recorded by sensors along the column. Based on the experimental observations, the relationship between higher-mode effects and the structural damage for tall-pier RC bridges was discussed. Similarly, many other works tested RC columns with scaled-down specimen [54]–[56]. Compared to the reduced-scale testing, the full-scale models could accurately reproduce the actual behavior of bridge columns [57] [52]. As reported by Schoettler et al. [52], a full-scale RC bridge was tested under a series of earthquake ground motions (GMs) at various intensities. Sensors along the heavily instrumented column had provided detailed dynamic responses at both global (i.e. displacement, acceleration) and local (i.e. bond-slip length and steel strain) levels. It was found that bond-slip effect was important in the RC bridge column. However, as revealed by many researchers ([58] [59] [60]), the FE prediction of seismic response of this RC column was challenging, and the correlation between the model predictions in the literature and the experimental data was poor, even for the first few GMs (see Figure 2-3).

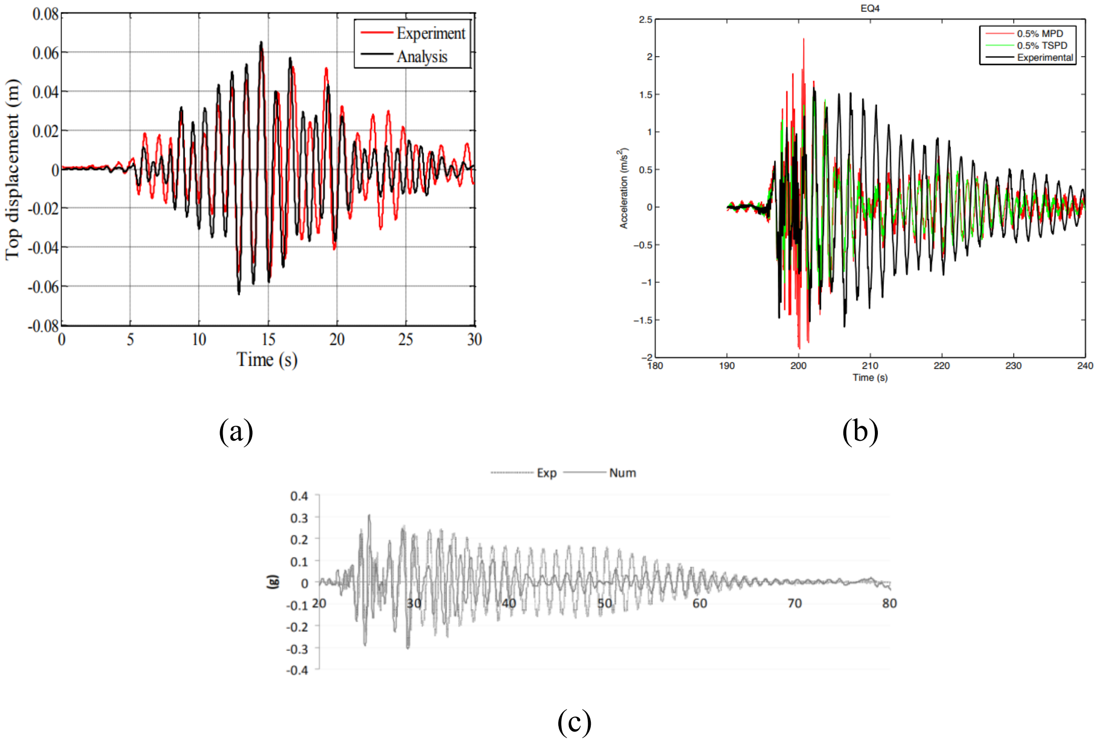

(a)

(b)

(c)

Figure 2-3: Blind prediction results on shake-table tested RC bridge pier columns by (a) Bianchi et al. [58], (b) Sousa et al. [59], and (c)Vila-Pouca et al. [60]

CHAPTER 3: BAYESIAN ESTIMATION USING UNSCENTED KALMAN FILTER

3.1 Introduction

Understanding the dynamic behavior of structures is one of the key problems encountered in the field of structural engineering. To tackle such a problem, finite element (FE) modeling is widely used along with dynamic experiments. Ideally, the modeling parameters required are determined from measurements (e.g., material coupon tests). Based on the information provided, an accurate FE model is developed to simulate the dynamic behavior of a structure. This method, often referred as forward modeling, has limited predictability for complex dynamic systems, where some modeling aspects are either inaccurate (e.g., due to uncertainty in measurements of properties) or unavailable (e.g., parameters that can not be measured directly). To improve the model accuracy for better interpretability or predictability, the undetermined parameters can be estimated using the system response observed, which leads to inverse modeling. The improved model can be further used for damage detection or prognosis in the field of structural health monitoring.

Specifically, inverse FE modelling, or finite element model updating (FEMU), has evolved as a popular research area in recent years [61] [62]. Various approaches can be used for FEMU, including least-square [39], hybrid Monte Carlo [63], simulated annealing, Kalman filter (KF) methods. Among those methods, KF-based stochastic parameter estimation methods, such as extended Kalman filter (EKF), unscented Kalman filter (UKF), and particle filter (PF), have been widely used due to their capability in handling uncertainties (e.g., model or measurement error). Many of these methods have seen successful applications in FEMU in the field of civil engineering (e.g.,[61], [62]). Among these studies, UKF have been widely used for nonlinear FEMU under seismic excitations (e.g.[36], [49], [64], [65]), which have proven that UKF is robust for identifying unknown model parameters in complex civil structures. One of advantages of UKF over other methods (e.g., EKF) is that UKF does not require the gradient information. In addition, compared to other gradient-free methods (e.g., PF), UKF has a relatively lower computational cost while maintaining acceptable accuracy [43].

However, though many successful applications of UKF have demonstrated its capability for nonlinear FEMU in the literature, the algorithm robustness, or the role of the algorithmic parameters in UKF is rarely discussed in depth. Experience with the choice of these parameters are required and of significant importance for the performance of UKF. To this end, this chapter will briefly summarize the theoretical aspects of nonlinear FEMU using UKF, followed by a simple academic example to demonstrate this method. After that, using the same example, the role of algorithmic parameters is assessed in terms of the overall performance of UKF for FEMU, including the convergence rate, accuracy of the mean estimation, uncertainty estimation (e.g., width of confidence interval). Such assessment will serve as the basis for applications of UKF in nonlinear FEMU presented in following chapters.

3.2 Unscented Kalman filter for FEMU

3.2.1 Kalman filter from a Bayesian point of view

Kalman filter, as the backbone of UKF, is described here first. In general, KF is a stochastic filtering method that combines the inaccurate prediction of future system state with the noisy measurement to estimate the uncertain aspects (i.e., states or model parameters) of the system. For such a system, the state vector ($\boldsymbol{x}_k$) at the current time step k can be derived from the prediction (or state-transition) equation as shown in Eq. (3–1):

$$\boldsymbol{x}_k = \boldsymbol{f}(\boldsymbol{x}_{k-1}, \boldsymbol{u}) + \boldsymbol{w} \tag{3–1}$$

where, $\boldsymbol{u}$ is system input vector that contains deterministic inputs, and $\boldsymbol{w}$ is the noise vector, which represents the uncertainty in predicting vector $\boldsymbol{x}_k$ using the state transition function $\boldsymbol{f}(\boldsymbol{x}_{k-1}, \boldsymbol{u})$. On the other hand, the measurement vector $\boldsymbol{y}_k$, representing the observation from the dynamic system at the current time step k, can be related to the state vector $\boldsymbol{x}_k$ via the measurement equation as shown in Eq. (3–2):

$$\boldsymbol{y}_k = \boldsymbol{h}(\boldsymbol{x}_k, \boldsymbol{u}) + \boldsymbol{v} \tag{3–2}$$

where, $\boldsymbol{h}$ represents the measurement function, and $\boldsymbol{v}$ represents the measurement noise vector. Similar as the state transition equation, the measurement equation has a zero-mean, Gaussian distributed noise vector $\boldsymbol{v}$ represent the uncertainty on predicting vector $\boldsymbol{y}_k$. Note that the 'state vector' $\boldsymbol{x}_k$ can contain both the state variables and/or unknown model parameters. For example, for parameter estimation in FEMU problems as studied in this research, it contains the unknown parameters only.

In a stochastic context, the estimation of $\boldsymbol{x}_k$ can be converted to obtaining the posterior probability density function (PDF) of $\boldsymbol{x}_k$ ($p(\boldsymbol{x}_k \mid \boldsymbol{y}_{1:k})$ from a Bayesian point of view.) Such a kind of problem with prior PDF of state vector $\boldsymbol{x}_{k-1}$. For this purpose, a two-step prediction-correction scheme can be applied. As presented by [66], the Bayesian prediction step that relates the PDF of $\boldsymbol{x}$ at step *k-1* and *k* can be expressed through the Chapman-Kolmogorov equation as shown in Eq. (3–3):

$$p(\boldsymbol{x}_k \mid \boldsymbol{y}_{1:k-1}) = \int p(\boldsymbol{x}_k \mid \boldsymbol{x}_{k-1}) p(\boldsymbol{x}_{k-1} \mid \boldsymbol{y}_{1:k-1}) d\boldsymbol{x}_{k-1} \tag{3–3}$$

The correction step, which computes the posterior PDF $p(\boldsymbol{x}_k \mid \boldsymbol{y}_{1:k})$, can be obtained through the Bayes' theorem [66] as per Eq. (3–4)

$$p(\boldsymbol{x}_k \mid \boldsymbol{y}_{1:k}) = \frac{p(\boldsymbol{y}_k \mid \boldsymbol{x}_k, \boldsymbol{y}_{1:k-1}) p(\boldsymbol{x}_k \mid \boldsymbol{y}_{1:k-1})}{p(\boldsymbol{y}_k \mid \boldsymbol{y}_{1:k-1})} = \frac{p(\boldsymbol{y}_k \mid \boldsymbol{x}_k) p(\boldsymbol{x}_k \mid \boldsymbol{y}_{1:k-1})}{\int p(\boldsymbol{y}_k \mid \boldsymbol{x}_k) p(\boldsymbol{x}_k \mid \boldsymbol{y}_{1:k-1}) d\boldsymbol{x}_{k-1}} \tag{3–4}$$

In the Kalman filter framework, $\boldsymbol{w}$ is assumed as a zero-mean Gaussian random vector with a covariance matrix $\boldsymbol{Q}$, and the state vector $\boldsymbol{x}_k$ is assumed as a Gaussian random vector with a mean vector $\bar{\boldsymbol{x}}_k$ and a covariance matrix $\boldsymbol{P}_{\boldsymbol{k}}^{\boldsymbol{xx}}$. As such, the posterior PDF of $\boldsymbol{x}_{k-1}$ given by $\boldsymbol{y}_{1:k-1}$ is characterized by a Gaussian distribution, see Eq. (3–5):

$$p(\boldsymbol{x}_{k-1} \mid \boldsymbol{y}_{1:k-1}) = N(\boldsymbol{x}_{k-1}; \bar{\boldsymbol{x}}_{k-1|k-1}, \bar{\boldsymbol{P}}_{k-1|k-1}^{\boldsymbol{xx}}) \tag{3–5}$$

where $N(\boldsymbol{x}_{k-1}; \bar{\boldsymbol{x}}_{k-1|k-1}, \bar{\boldsymbol{P}}_{k-1|k-1}^{\boldsymbol{xx}})$ denotes a multivariate Gaussian distribution of $\boldsymbol{x}_{k-1}$ given $\boldsymbol{y}_{1:k-1}$ with a mean vector $\bar{\boldsymbol{x}}_{k-1|k-1}$ and a covariance matrix $\bar{\boldsymbol{P}}_{k-1|k-1}^{\boldsymbol{xx}}$. By substituting Eq. (3–1), Eq. (3–3), and Eq. (3–5), the posterior distribution of $\boldsymbol{x}_k$ given $\boldsymbol{y}_{1:k-1}$, with mean $\bar{\boldsymbol{x}}_{k|k-1}$ and the matrix $\bar{\boldsymbol{P}}_{k|k-1}^{\boldsymbol{xx}}$ could be predicted according to Eq. (3–6) and (3–7), respectively.

$$\bar{\boldsymbol{x}}_{k|k\text{-}1} = \int \boldsymbol{f}_k(\boldsymbol{x}_{k-1}, u_{k-1}) N(\boldsymbol{x}_{k-1}; \bar{\boldsymbol{x}}_{k-1|k-1}, \bar{\boldsymbol{P}}_{k-1|k-1}^{\boldsymbol{xx}}) d\boldsymbol{x}_{k-1} \tag{3–6}$$

$$\bar{\boldsymbol{P}}_{k|k-1}^{\boldsymbol{xx}} = \int \boldsymbol{f}_k(\boldsymbol{x}_{k-1}, u_{k-1}) \boldsymbol{f}_k^T(\boldsymbol{x}_{k-1}, u_{k-1}) N(\boldsymbol{x}_{k-1}; \bar{\boldsymbol{X}}_{k-1|k-1}, \bar{\boldsymbol{P}}_{k-1|k-1}^{\boldsymbol{xx}}) d\boldsymbol{x}_{k-1} - \bar{\boldsymbol{x}}_{k|k-1} \bar{\boldsymbol{x}}_{k|k-1}^T + \boldsymbol{Q} \tag{3–7}$$

Similarly, in the KF framework, the measurement noise vector $\boldsymbol{v}$ is also be assumed zero-mean Gaussian defined by a covariance matrix $\boldsymbol{R}$. The measurement vector $\boldsymbol{y}_k$ given by is assumed as Gaussian with a mean vector $\bar{\boldsymbol{y}}_k$ and a covariance matrix $\bar{\boldsymbol{P}}^{\boldsymbol{yy}}_{k|k-1}$. Considering the posterior distribution of $\boldsymbol{x}_k$ given $\boldsymbol{y}_{1:k-1}$ can be characterized with a Gaussian distribution, see Eq. (3–8):

$$p(\boldsymbol{x}_k \mid \boldsymbol{y}_{1:k-1}) = N(\boldsymbol{x}_k ; \bar{\boldsymbol{x}}_{k|k-1}, \bar{\boldsymbol{P}}^{\boldsymbol{xx}}_{k|k-1}) \qquad (3\text{–}8)$$

and, the posterior PDF of $\boldsymbol{y}_k$ given $\boldsymbol{y}_{k-1}$, defined by the mean vector $\bar{\boldsymbol{y}}_{k|k-1}$ and covariance matrix $\bar{\boldsymbol{P}}^{yy}_{k|k-1}$ can evaluated according to Eq. (3–9) and Eq. (3–10), respectively.

$$\bar{\boldsymbol{y}}_{k|k\text{-}1} = \int \boldsymbol{h}_k(\boldsymbol{x}_k , \ddot{u}^g_{1:k}) N(\boldsymbol{x}_k ; \bar{\boldsymbol{x}}_{k|k-1}, \bar{\boldsymbol{P}}^{xx}_{k|k-1}) d\boldsymbol{x}_k \qquad (3\text{–}9)$$

$$\bar{\boldsymbol{P}}^{\boldsymbol{yy}}_{k|k\text{-}1} = \int \boldsymbol{h}_k(\boldsymbol{x}_k , u_k) \boldsymbol{h}^T_k(\boldsymbol{x}_k , u_k) N(\boldsymbol{x}_k ; \bar{\boldsymbol{x}}_{k|k-1}, \bar{\boldsymbol{P}}^{xx}_{k|k-1}) d\boldsymbol{x}_k - \bar{\boldsymbol{y}}_{k|k-1} \bar{\boldsymbol{y}}^T_{k|k-1} + \boldsymbol{R}_k \qquad (3\text{–}10)$$

The cross-covariance matrix between $\boldsymbol{x}_k$ and $\boldsymbol{y}_k$ could be calculated by Eq. (3–11):

$$\bar{\boldsymbol{P}}^{\boldsymbol{xy}}_{k|k\text{-}1} = \int \boldsymbol{x}_k \boldsymbol{h}^T_k(\boldsymbol{x}_k , u_k) N(\boldsymbol{x}_k ; \bar{\boldsymbol{x}}_{k|k-1}, \bar{\boldsymbol{P}}^{\boldsymbol{xx}}_{k|k-1}) d\boldsymbol{x}_k - \bar{\boldsymbol{x}}_{k|k-1} \bar{\boldsymbol{y}}^T_{k|k-1} \qquad (3\text{–}11)$$

With the posterior PDF of vectors $\boldsymbol{x}_{k|k\text{-}1}$, $\boldsymbol{y}_{k|k\text{-}1}$ and cross-covariance matrix $\boldsymbol{P}^{\boldsymbol{xy}}{}_{k|k\text{-}1}$ are defined, the correction step is then being performed to estimate the posterior PDF of the state vector $\boldsymbol{x}_k$ given by $\boldsymbol{y}_{1:k}$ as per Eq. (3–12) and (3–13), respectively. [67]

$$\bar{\boldsymbol{x}}_{k|k} = \bar{\boldsymbol{x}}_{k|k-1} + \boldsymbol{K}_k (\boldsymbol{y}^{Obs}_{1:k} - \bar{\boldsymbol{y}}_{k|k-1}) \qquad (3\text{–}12)$$

$$\bar{\boldsymbol{P}}^{\boldsymbol{xx}}_{k|k} = \bar{\boldsymbol{P}}^{\boldsymbol{xx}}_{k|k-1} - \boldsymbol{K}_k \bar{\boldsymbol{P}}^{\boldsymbol{yy}}_{k|k\text{-}1} \boldsymbol{K}^T_k \qquad (3\text{–}13)$$

where, $\boldsymbol{y}^{Obs}_{1:k}$ represents the actual measurement vector at time step k and $\boldsymbol{K}_k$ denotes the Kalman gain matrix, which could be obtained by Eq. (3–14)

$$\boldsymbol{K}_k = \bar{\boldsymbol{P}}^{\boldsymbol{xy}}_{k|k\text{-}1} (\bar{\boldsymbol{P}}^{\boldsymbol{yy}}_{k|k\text{-}1})^{-1} \qquad (3\text{–}14)$$

3.2.2 Unscented transformation

In the case of FEMU, where the finite element model is chosen as the prediction function, it is hard to solve the integral in the Eq. (3–6), (3–7), (3–9), (3–10) and (3–11), which are utilized to approximate the distribution. As such, the unscented transformation (UT) is utilized to approximate those PDF predictions.

For vector $\boldsymbol{x}_{k-1}$, as a n_x-dimensional random vector with mean $\boldsymbol{\mu}^{\boldsymbol{x}}_{k-1|k-1}$ and covariance matrix $\boldsymbol{P}^{\boldsymbol{xx}}_{k-1|k-1}$ after previous analysis step (k-1). Such information is utilized to predict the prior distribution of state vector. To achieve this, a set of sigma points (SPs) are generated based on the prior covariance matrix of state vector ($\boldsymbol{P}^{\boldsymbol{xx}}_{k-1|k-1}$). The value of each SP is defined by the equation below:

$$\boldsymbol{X}^{i}_{k-1|k-1} = \begin{cases} \boldsymbol{\mu}^{x}_{k-1|k-1} & i=0 \\ \boldsymbol{\mu}^{x}_{k-1|k-1} + [(\gamma\sqrt{\boldsymbol{P}^{xx}_{k-1|k-1}})_i]^T & i=1,2,\ldots,n_x \\ \boldsymbol{\mu}^{x}_{k-1|k-1} + [(\gamma\sqrt{\boldsymbol{P}^{xx}_{k-1|k-1}})_{i-n_x}]^T & i=n_x+1,\ldots,2n_x \end{cases} \tag{3–15}$$

where $(\sqrt{\boldsymbol{P}^{\boldsymbol{xx}}_{k-1|k-1}})_i$ represents the i^{th} row of the square root of $\boldsymbol{P}^{\boldsymbol{xx}}_{k-1|k-1}$ and γ is a factor that controls the 'spread' of the SPs.

3.2.3 Unscented transformation example

To demonstrate the prediction accuracy of the unscented transform (UT), a simple nonlinear transformation example is studied by comparing the estimation of the first and second order moments (i.e., mean vector, and covariance matrix) estimated by UT and the Monte Carlo sampling.

Consider a nonlinear transform, $\boldsymbol{y} = \boldsymbol{f}(\boldsymbol{x})$, defined as Eq. (3–16), in which $\boldsymbol{x} = [x_1 \quad x_2 \quad x_3]$ is a Gaussian distributed random vector. Thus, $\boldsymbol{x}$ is defined by a mean $\overline{\boldsymbol{x}} = [1 \quad 2 \quad 3]$ and the covariance matrix $\boldsymbol{P}^{\boldsymbol{xx}} = \begin{bmatrix} 1 & 0.2 & 0.5 \\ 0.2 & 1 & 0.4 \\ 0.5 & 0.4 & 1 \end{bmatrix}$. The nonlinear transform $\boldsymbol{y} = \boldsymbol{f}(\boldsymbol{x})$ involves complex nonlinear mapping, including a polynomial, a trigonometric, and an exponential function.

$$\boldsymbol{y} = \boldsymbol{f}(\boldsymbol{x}) = \begin{bmatrix} x_1^3 + 2x_2^2 \\ x_1^2 + \sin(x_3) \\ x_1^3 + 2x_1x_2 + e^{x_3} \end{bmatrix} \tag{3–16}$$

To approximate the first two statistical moments (mean and the covariance) of vector $\boldsymbol{y}$, 100,000 sample points are simulated in the Monte Carlo sampling (MCS) method, while the UT only uses 7 sigma points according to Eq. (3–15). The mean and covariance information estimated for $\boldsymbol{y}$ from UT and MCS is summarized in the Table 3-1.

Table 3-1: Comparison of estimation results between Monte Carlo simulation method and unscented transform

	Mean			Covariance matrix					
Statistics	$\bar{y}_1$	$\bar{y}_2$	$\bar{y}_3$	σ_{y1}	σ_{y2}	σ_{y3}	δ_{12}	δ_{13}	δ_{23}
MCS	13.99	2.09	41.48	11.51	2.27	49.61	0.63	0.60	0.43
UT	14.00	2.07	38.53	11.05	2.17	41.90	0.59	0.62	0.36

The results reveal that the UT can approximate the first- and second-order statistics of a nonlinear function with only limited SPs. This implies the efficiency of the UT in approximating a nonlinear function of a random vector, which can be potentially used to improve the Kalman filter.

3.2.4 Updating step of unscented Kalman filter

The prediction step and the updating steps as described in previous section could then be infused with the UT. As such, the estimation equation for the mean $\bar{\boldsymbol{x}}_{k|k\text{-}1}$, Eq. (3–6), and covariance matrix $\bar{\boldsymbol{P}}_{k|k-1}^{\boldsymbol{xx}}$, Eq. (3–7), can then be combined with UT as shown in Eq. (3–17) and Eq. (3–18) below:

$$\bar{\boldsymbol{x}}_{k|k\text{-}1} = \sum_{i=0}^{2n_x} \boldsymbol{W}_{\boldsymbol{m}}^i \boldsymbol{f}_k(\boldsymbol{X}_{k\text{-}1|k\text{-}1}^i) \tag{3–17}$$

$$\bar{\boldsymbol{P}}_{k|k-1}^{\boldsymbol{xx}} = \sum_{i=0}^{2n_x} \boldsymbol{W}_c^i [\boldsymbol{f}_k(\boldsymbol{X}_{k\text{-}1|k\text{-}1}^i) - \bar{\boldsymbol{x}}_{k|k-1}][\boldsymbol{f}_k(\boldsymbol{X}_{k\text{-}1|k\text{-}1}^i) - \bar{\boldsymbol{x}}_{k|k\text{-}1}]^{\boldsymbol{T}} + \boldsymbol{Q} \tag{3–18}$$

The $\boldsymbol{W_m}$ and $\boldsymbol{W_c}$ above are corresponding weight factors for the estimation on mean and covariance matrix at each SP, which are defined as shown in Eq. (3–19).

$$\boldsymbol{W}_{\boldsymbol{m}}^{i}=\begin{cases}\lambda/(n_{\boldsymbol{x}}+\lambda) & i=0\\ 1/2(n_{\boldsymbol{x}}+\lambda) & i\neq 0\end{cases}$$

$$\boldsymbol{W}_{c}^{\boldsymbol{i}}=\begin{cases}\lambda/(n_{\boldsymbol{x}}+\lambda)+(1-\alpha^{2}+\beta) & \boldsymbol{i}=0\\ 1/2(n_{\boldsymbol{x}}+\lambda) & \boldsymbol{i}\neq 0\end{cases} \tag{3–19}$$

where λ is a factor to reduce the higher order error of the approximation, defined by equation $\lambda = \alpha^2(n_x + \kappa) - n_x$, where α and κ are system factors of the UT that controls the sampling of the SPs.

In terms of the FEMU, the unknown modeling aspects chosen for update are assumed as time-invariant. As such, the prediction function of $\boldsymbol{x}$ can be rewritten as Eq. (3–20):

$$\boldsymbol{x}_{k}=\boldsymbol{f}_{k}(\boldsymbol{x}_{k-1})=\boldsymbol{x}_{k-1} \tag{3–20}$$

With the prediction function of $\boldsymbol{x}$ is determined, the prior mean and covariance matrix for current analysis step can be determined and their value are equals to the posterior value of state vector in previous analysis steps, represented by Eq. (3–21)

$$\bar{\boldsymbol{x}}_{k|k\text{-}1}=\bar{\boldsymbol{x}}_{k\text{-}1|k\text{-}1}$$

$$\bar{\boldsymbol{P}}_{k|k-1}^{\boldsymbol{xx}}=\bar{\boldsymbol{P}}_{k\text{-}1|k-1}^{\boldsymbol{xx}} \tag{3–21}$$

The prior estimation of measurement vector $\boldsymbol{y}$ can be calculated with similar approach in Eq. (3–22) and Eq. (3–23):

$$\bar{\boldsymbol{y}}_{k|k\text{-}1}=\sum\nolimits_{i=0}^{2n_{x}}\boldsymbol{W}_{\boldsymbol{m}}^{i}\boldsymbol{h}_{k}(\boldsymbol{X}_{k|k\text{-}1}^{i},\ddot{u}_{1:k}^{\boldsymbol{g}}) \tag{3–22}$$

$$\bar{\boldsymbol{P}}_{k|k-1}^{\boldsymbol{yy}}=\sum\nolimits_{i=0}^{2n_{x}}\boldsymbol{W}_{\boldsymbol{c}}^{i}[\boldsymbol{h}_{k}(\boldsymbol{X}_{k|k\text{-}1}^{i},\ddot{u}_{1:k}^{\boldsymbol{g}})-\bar{\boldsymbol{y}}_{k|k\text{-}1}][\boldsymbol{h}_{k}(\boldsymbol{X}_{k|k\text{-}1}^{i},\ddot{u}_{1:k}^{\boldsymbol{g}})-\bar{\boldsymbol{y}}_{k|k\text{-}1}]^{\boldsymbol{T}}+\boldsymbol{R} \tag{3–23}$$

Function $\boldsymbol{h}_k$ denotes the FE analysis for current analysis iteration and the $\ddot{u}_{1:k}^{\boldsymbol{g}}$ represents the external boundary conditions for the FEA (acceleration, etc.). Considering the mean and covariance of the state vector are the same before and after the UT, the definition of each SPs ($\boldsymbol{X}_{k|k\text{-}1}^{i}$) in Eq. (3–17) and Eq. (3–18) are kept the same. As such, the cross-covariance matrix can be estimated as follows:

$$\bar{\boldsymbol{P}}^{xy}_{k|k-1} = \sum\nolimits_{i=0}^{2n_x} \boldsymbol{W}_c^i [\boldsymbol{f}_k(\boldsymbol{X}_k^i, \ddot{u}^g_{1:k}) - \bar{\boldsymbol{x}}_{k|k\text{-}1}][\boldsymbol{h}_k(\boldsymbol{X}_k^i, \ddot{u}^g_{1:k}) - \bar{\boldsymbol{y}}_{k|k\text{-}1}]^T \tag{3–24}$$

As such. the flowchart of the combination between *MATLAB* and *OpenSees* are shown as Figure 3-1 below:

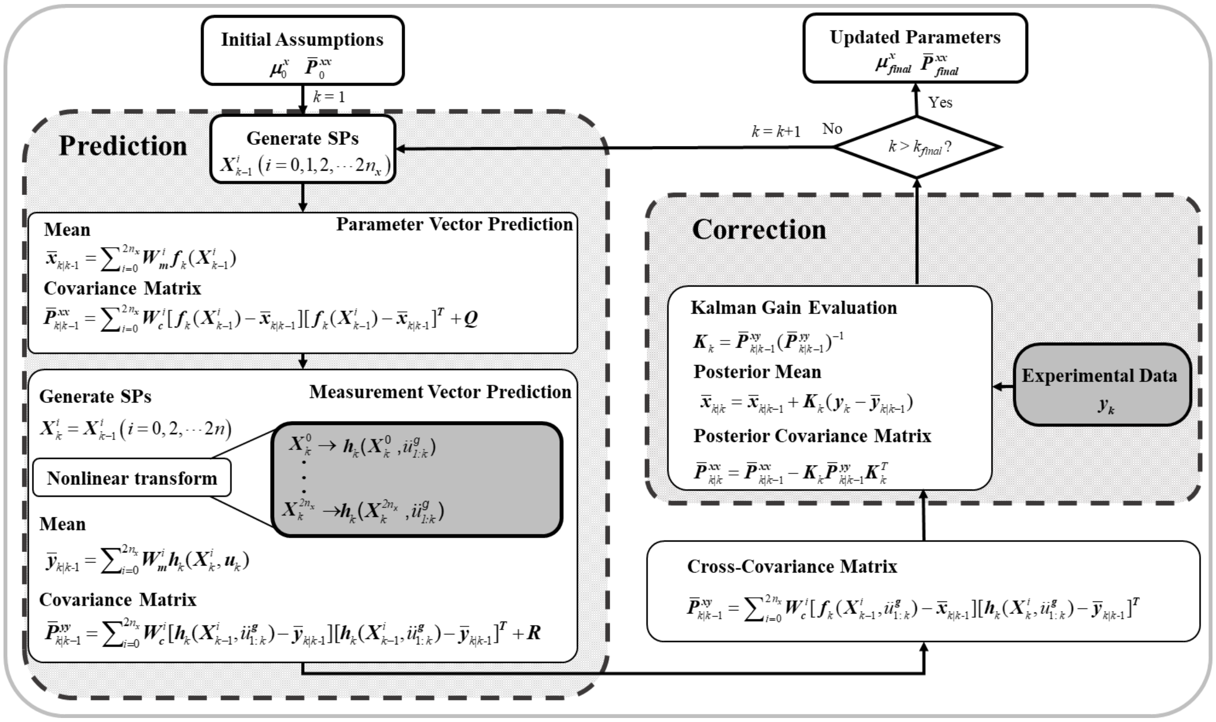

Figure 3-1: Adopted framework of unscented Kalman filter-infused FEMU approach

3.3 Refinements on the FEMU algorithm

3.3.1 Parallel computing

As can be noticed, for each iteration at the FEMU, a FEA is performed at each SP, which means the computation cost can grow exponentially during the updating process since the total number of analysis steps increases with the FEMU iterations). Furthermore, the total number of SPs at UT is equal to $(2n_x + 1)$ where n_x is the dimension of the state vector $\boldsymbol{x}$, indicating that more runs are required for each FEMU iteration when more parameters need to be estimated. Thus, it is important to increase the efficiency of the algorithm. To this end, considering all SPs are independent of each other, paralleling the FEA for all SPs could greatly reduce the computational cost. The parallel computing command from the communication toolbox in *MATLAB* provides an integrated solution, which allows the user to construct a local parallel pool to optimize the computing procedure, by allowing the FEA for each SP being processed on separate cores of the computer CPU.

Time taken by the pre-process (generating SPs, etc.), FE analysis (for the runs at all SPs) and post-process (gathering FEA results, update parameters etc.) is evaluated within a simple FEMU. It is found that the FE analysis takes the largest portion of the total analysis time. By introducing parallel computing, the total analysis duration can be reduced effectively, depending on the computer configurations and the number of SPs.

3.3.2 Measurement data cutting and skipping for updating

As a common phenomenon for structures under dynamic loads, the response magnitude in the beginning and the end of the measurement is low in terms of signal-to-noise ratio (SNR). As such, data that lacks valuable information for FEMU can be cut out of the original measurement to reduce the total analysis steps and therefore improve the updating efficiency.

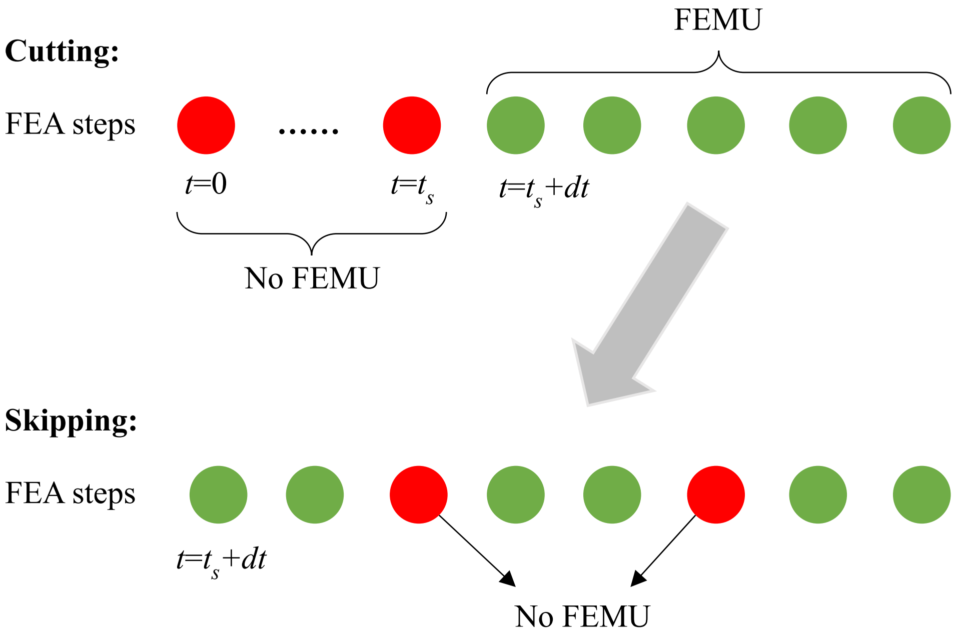

Figure 3-2: Measurement data cutting-skipping strategy adopted in the proposed FEMU framework

In addition, for some dynamic analysis that has a high sampling rate, the information provided by adjacent analysis steps are highly correlated and thus redundant. To this end, some analysis steps can be skipped to increase the overall efficiency of FEMU, while maintaining sufficient information for the FEMU. In this study, both approaches are implemented in the FEMU process and the brief demonstration on the measurement data cutting-skipping strategy is summarized as shown in Figure 3-2.

3.4 Algorithm verification

A two-dimensional (2D) RC frame model is developed to demonstrate and examine the ability of the proposed FEMU framework in estimating the uncertain modeling aspects. As shown in Figure 3-3, the 2D frame is modeled using three displacement-based fiber beam-column elements, each with 5 integration points. On each of the integration points, a fiber section is assigned, consisting of 16 × 8 concrete fibers and 3 × 2 reinforcing steel fibers.

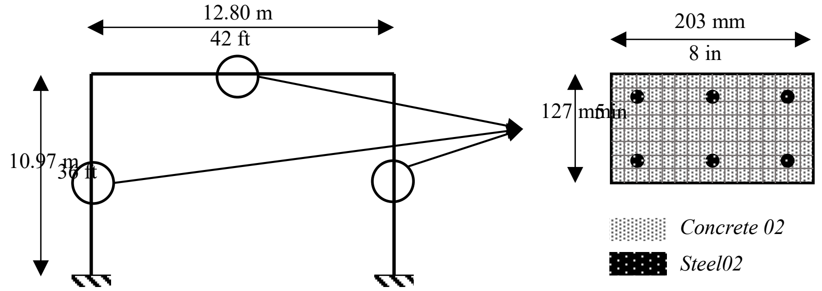

Figure 3-3: The 2D RC frame model used to demonstrate and examine the capability of the proposed FEMU framework

Different material models in the *OpenSees* library, namely *Steel02* and *Concrete02*, are assigned to the reinforcement and the concrete fiber in the section, respectively. The definitions for each material model are shown in Table 3-2, where the true values of each material property are assumed in accordance of the material coupon test results performed by Schotter et al. [52]. As for the concrete material model, the maximum compressive strength f_c' is assumed as 40.9 MPa and the corresponding strain ε_c is assumed as 0.0026. The concrete crushing strength f_{cu}' and the crushing strain ε_{cu} are assumed as $20\% f_c'$ and $3\varepsilon_c$, respectively. The tensile behavior for the core concrete is defined with the tensile strength f_t= 10%f_c' , the unloading stiffness ratio λ = 0.1, and the tension softening stiffness E_{ts} = 10% of the elastic modulus of concrete. As for steel material model, the yield strength f_y , the elastic modulus E_s , and the post-yield hardening ratio b_{sh} are assumed as 520 MPa, 196 MPa and 0.01, respectively. Furthermore, values of elastic-plastic transition parameters R_0, r_1, and r_2 are assumed as recommended by Filippou et. al [23].

The true measurement is then generated by recording the horizontal drift history of the frame while subjecting the structure with the ground motion acceleration recorded from the Kobe earthquake in 1995, with the peak ground acceleration (PGA) at 0.49 m/s^2.

Table 3-2: Material model parameter definitions of the material models assigned at the fiber sections

Concrete fiber material (*Concrete02*)						
f_c'	ε_c	f_{cu}'	ε_{cu}	λ	f_t	E_{ts}
40.9 MPa	0.0026	10 MPa	0.0078	0.1	4.1 MPa	1.88 GPa
Steel fiber material (*Steel02*)						
f_y	E_s	b_{sh}	R_0	r_1	r_2	
520 MPa	196 GPa	0.1	20	0.925	0.15	

The FEMU framework is used to update the FE model using the simulated seismic data by assuming three modeling parameters (f_c' , E_s, and b_{sh}) are unknown. As presented in Figure 3-4, the FEMU framework successfully estimated the true value for each parameter with a narrow 95% confidence interval. The successful parameter identification showed that the capability of the FEMU estimating parameters in a nonlinear FE model. Note that the updating of the strain hardening ratio for steel is relatively later than the other two parameters because the steel did not yield at the beginning and thus no information regarding b_{sh} is contained in the measurement.

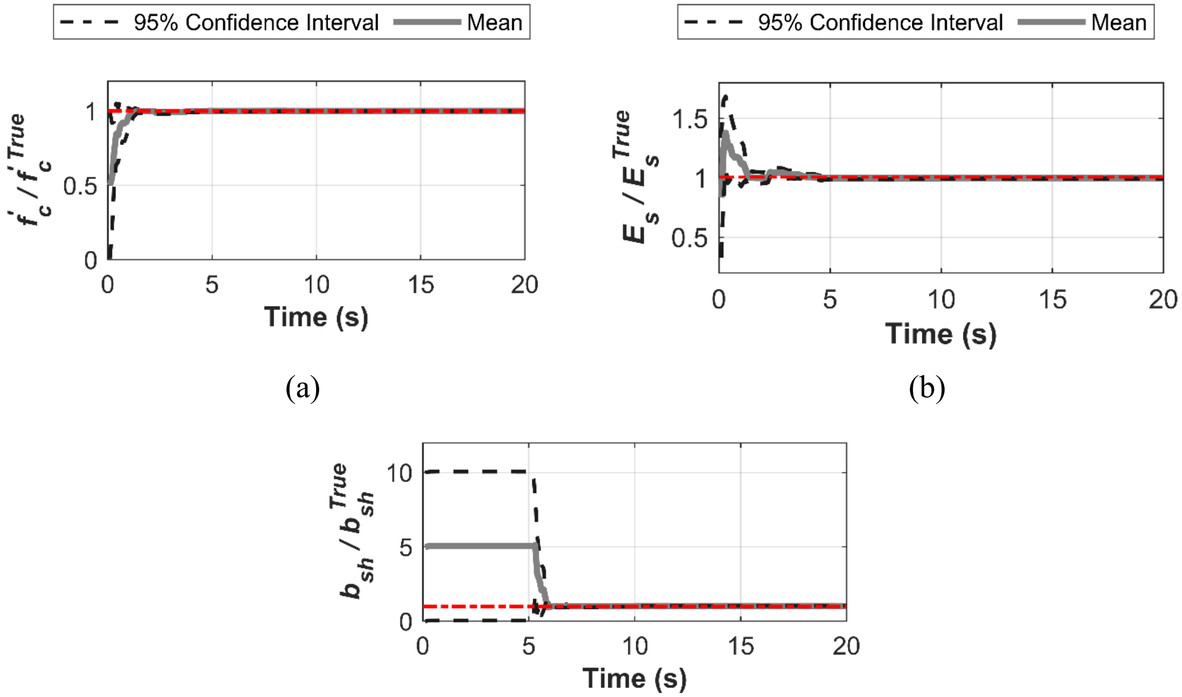

(a)

(b)

(c)

Figure 3-4: Parameter update history of material parameters normalized by the corresponding true values: (a) $f_c' / f_c'^{True}$, (b) E_s/E_s^{True}, and (c) b_{sh}/b_{sh}^{True}

3.5 Study of algorithmic parameters in UKF-based FEMU

In addition to the initial estimate or prior mean of the parameters, three algorithmic matrices need to be defined for UKF-based FEMU approach. They are the initial covariance matrix $\boldsymbol{P}$, the measurement noise matrix $\boldsymbol{R}$, and the process noise matrix $\boldsymbol{Q}$. To explore their optimal settings for a successful FEMU, a detailed parameter study is performed in this section. Thus, a simple example with an elastic FE model is used as the test bed to evaluate the FEMU efficiency under different algorithmic parameters.

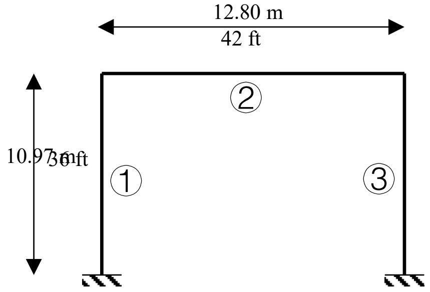

Figure 3-5: Schematic view of the FE model of elastic frame system used to study the algorithmic parameters in UKF-based FEMU

A 2D elastic frame model, as shown in Figure 3-5, is developed, which consists of three elastic elements. For each element, three parameters are used to define their physical aspects, including the cross-sectional area, the moment of inertia, and the elastic modulus as described in Table 3-3.

Table 3-3: Parameter definition of each elastic element for the FE model of elastic frame system used to study the algorithmic parameters in UKF-based FEMU

Element	Area (A)	Moment of inertia (I)	Elastic modulus (E)
#1	2.32 m^2	0.45 m^4	29.14 GPa
#2	2.32 m^2	0.45 m^4	29.14 GPa
#3	3.72 m^2	1.84 m^4	29.14 GPa

Structure response is recorded by subjecting the 2D elastic frame model with an acceleration series recorded during the Kobe earthquake in 1995, with the peak ground acceleration (PGA) at 0.49m/s^2. To take the measurement error into account, a zero-mean additive Gaussian white noise (AGWN) is added to the recorded structural response and different noise levels are considered in terms of the variance of the AGWN, e.g., 0 for zero noise, 1×10^{-8} in^2 (6.5×10^{-12} m^2) for high level of noise, and 1×10^{-10} in^2 (6.5×10^{-14} m^2) for low level of noise. The elastic modulus of member #3 is selected to be updated with initial value assumed as 80% of its true value ($E_{ini} = 0.8\ E_{true}$) to ensure a fair comparison among different cases.

To begin with, the relationship between the updating accuracy and the values of matrix $\boldsymbol{Q}$ and $\boldsymbol{R}$ is studied considering they affect the value of $\boldsymbol{P}_{k|k-1}^{\boldsymbol{xx}}$ and $\boldsymbol{P}_{k|k-1}^{\boldsymbol{yy}}$ in Eq. (3–18) and Eq. (3–23). Therefore, 13 different process noise levels, ranging from $1 \times 10^{-12} \times E_{ini}$ to $1 \times 10^{0} \times E_{ini}$, and 13 different measurement noise levels, ranging from 1×10^{-12} in^2 (6.5×10^{-16} m^2) to 1×10^{0} in^2 (6.5×10^{-4} m^2), are considered, leading to 169 cases with different combinations of $\boldsymbol{Q}$ and $\boldsymbol{R}$. For each case, the FEMU is performed for the frame system to identify the values of the unknown parameters until convergence is reached.

$$RRMSE = \frac{\sqrt{\frac{1}{\mathrm{n}}\sum_{\mathrm{i}=1}^{\mathrm{n}}\left(\boldsymbol{y}_{Mea}^{i} - \boldsymbol{y}_{FEA}^{i}\right)^{2}}}{\sum_{\mathrm{i}=1}^{\mathrm{n}}\boldsymbol{y}_{Mea}^{i}} \tag{3–25}$$

To quantify the performance of the FEMU, the relative root mean square error (*RRMSE*) between the updated model response ($\boldsymbol{y}_{FEA}^{\boldsymbol{i}}$) and the true measurement ($\boldsymbol{y}_{Mea}^{\boldsymbol{i}}$) is evaluated at each of 169 cases as represented by Eq. (3–25).

As can be observed, the prediction accuracy of the UKF increases with a decreasing value of the variance in the measurement noise ($\boldsymbol{R}$) for the case with zero AGWN (see Figure 3-6 a). For the updating cases with either low or high AGWN in the measurements, a significantly high prediction accuracy can be clearly observed if the assumed variance of the measurement noise is within a certain range (Figure 3-6 b and c). Further examination revealed that the measurement noise assumption is related to the prediction accuracy. Specifically, an accurate prediction on the structural response can be observed when variance of the measurement noise is assumed within the range from 1×10^{-7} in^2 (6.5×10^{-11} m^2) to 1×10^{-9} in^2 (6.5×10^{-13} m^2) and 1×10^{-9} in^2 (6.5×10^{-13} m^2) to 1×10^{-11} in^2 (6.5×10^{-15} m^2) when the true variance of the measurement error is 1×10^{-8} in^2 (6.5×10^{-12} m^2) and 1×10^{-10} in^2 (6.5×10^{-14} m^2), respectively. As such, it implies that with better assumption of the magnitude of measurement error, better accuracy of FEMU could be achieved and the initial assumption of the variance of the measurement noise is recommended to be within the range of 10^{-7} to 10^{-11} for this problem.

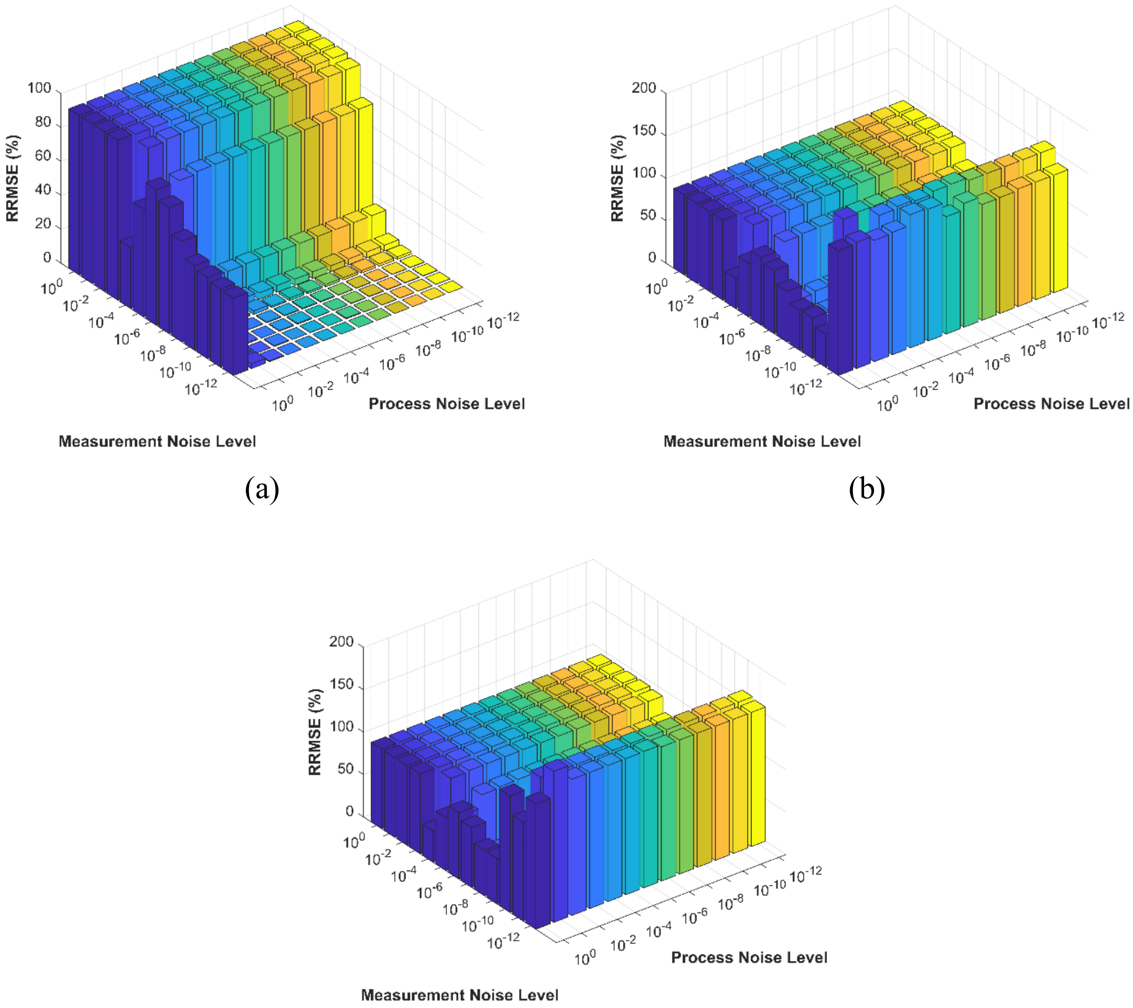

(a)

(b)

(c)

Figure 3-6: Accuracy comparison between different combination of process noise matrix (***Q***) and measurement noise (***R***) at (a) zero AGWN, (b) low level AGWN, and (c) high level AGWN

However, in general, the prediction accuracy of FEMU is not sensitive to the magnitude of the process noise matrix ***Q*** as no significant trend can be observed from the all three cases as depicted in Figure 3-6. This is because the vector ***x*** is assumed as time independent in the FEMU algorithm. Still, the poor assumption of ***Q*** leads to inaccurate prediction for extreme cases as shown in Figure

3-6 and the magnitude of the variance is recommended within the range between 1×10^{-4} (6.5×10^{-8} m^2) and 1×10^{-12} (6.5×10^{-16} m^2).

3.6 Summary

In this chapter, a FEMU framework that combines the UKF and nonlinear FE analysis is introduced. Different strategies, such as parallel computing and data preprocessing through cutting and skipping are integrated into the framework to reduce the computational cost. The accuracy and the efficiency of the FEMU framework is verified by case studies with different application examples, from simple linear elastic to nonlinear FE models. In addition, a parametric study is performed to explore the algorithmic parameters for the UKF-based FEMU, including the covariance matrix of the process noise $\boldsymbol{Q}$, and covariance matrix of the measurement noise $\boldsymbol{R}$. Such analysis provided reference values for the choice of $\boldsymbol{Q}$ and $\boldsymbol{R}$ when the UKF-based FEMU is applied to more complex problems.

CHAPTER 4: NONLINEAR FE MODEL UPDATING FOR BRIDGE COLUMN WITH BOND-SLIP

4.1 Introduction

Detection of structure damage, often refers to the identifying changes of local properties (i.e. bonding) or system properties (e.g., frequency, damping ratio), is one of the major problems in the field of structure health monitoring (SHM). With the development of computing technologies, finite element model updating (FEMU) is increasingly applied to identify the structural damage in complex structures. In this chapter, the FEMU framework introduced in Chapter 3 is utilized to capture the damage-related parameters of a reinforced concrete (RC) bridge pier column subjected to a series of earthquake excitations during a shake-table test. As the key component in modeling the structural behavior, bond-slip between steel rebars and surrounding concrete in RC columns is taken into consideration to increase the modeling accuracy. To be practical in the FEMU, the updating parameters are carefully chosen based on the information available from material coupon tests and the relative importance of modeling parameters learned from a local sensitivity analysis. Along with the FEMU on the bridge pier column, the damage evolution during the sequence of ground motions (GMs) is also analyzed. To demonstrate the accuracy of the update FE model, the FE predictions and the measured responses are compared in terms of the time histories and the transfer functions estimated for the system. Furthermore, the predictability of the updated FE model based on seismic response data from an individual GM is assessed in simulating the responses of the tested RC bridge pier column under following GMs at various intensities.

4.2 Shake-table tested bridge column

The full-scale RC bridge pier column considered was tested in 2010 at the University of California, San Diego. During the test, the specimen was subjected to a sequence of 10 earthquake GMs [52]. The design of the specimen was targeted to represent a regular single-column bent from typical highway bridges in California, U.S., according to the Caltrans Seismic Design Criteria [68]. The bridge pier column specimen, as shown in Figure 4-1, consists of three major components: the RC column body, the footing at the bottom, and a superstructure mass block seated on the column top. Dimension wise, the RC column body is 7.32 m (24.0 ft) tall, measured from the top surface of the footing to the top of the column. It has a circular cross-section with a diameter of 1.22 m (4.0 ft), 50.8 mm (2.0 in) thick concrete cover, and 18 #11 longitudinal steel rebars, which are confined with double #6 stirrups spaced at 152 mm (6.0 in) along the column. Material wise, the concrete mix was designed to have a nominal strength of 27.6 MPa (4.0 ksi) and a weight density at 23.6 kN/m^3 (150 pcf), while the material for the longitudinal steel rebars and transverse stirrups in this column are Grade 60 steel with a nominal yield strength of 414 MPa (60 ksi). For the other components of the test specimen, the concrete footing is fixed with the shake-table using post-tensioned bars to prevent the relative displacement; the superstructure mass block was designed to provide a vertical axial load (236.493 ton with an axial load ratio at 5.3%) on the bridge pier, and a rotational mass inertia ($2.5\times10^{10}\,\text{kNm}\cdot\text{s}^2$) to trigger the second order effect.

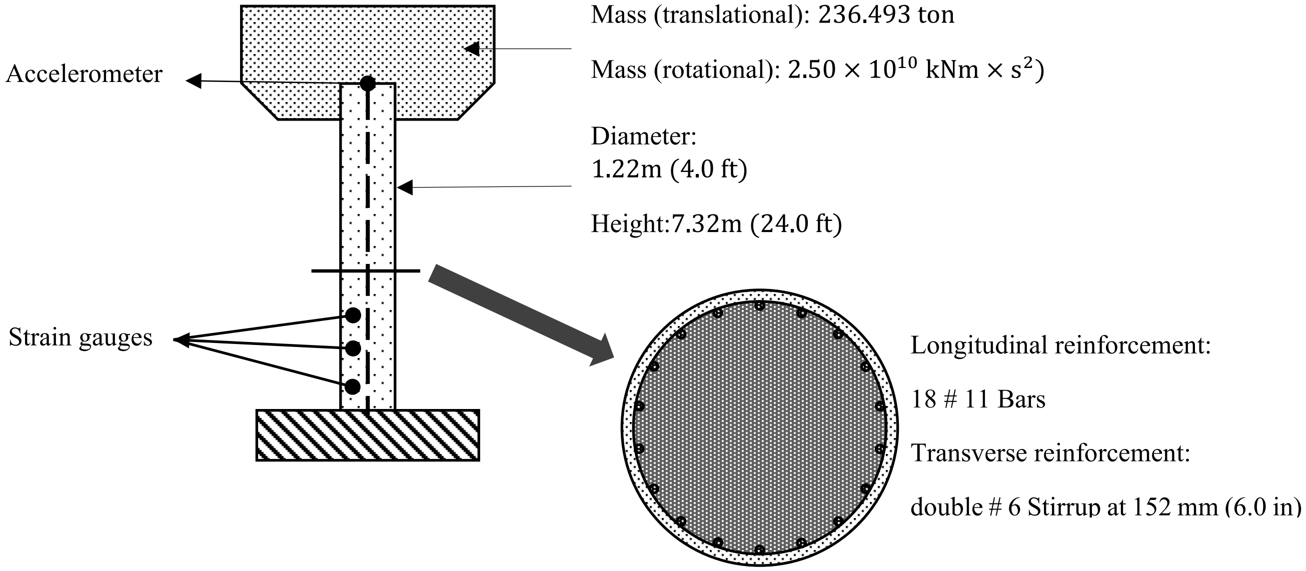

Figure 4-1: Schematic view of the full-scale RC bridge pier column tested on the shake-table

4.2.1 Shake-table test on the RC bridge pier column

The ten GMs used in the shake-table test can be characterized into two categories according the damage observed in the RC column: the first four GMs (less damage) and the last six GMs (more damage). The first four GM acceleration series were recorded at different stations (i.e., Agnew State Hospital, Corralitos, LGPC, and Corralitos) from the Mw 6.9 Loma Prieta earthquake in 1989, as summarized in Table 4-1. Among the four GMs, GM1 had the lowest peak ground acceleration (PGA), and it would be used first to inform the FE modeling of the bridge column with no visible damage during the test. After GM1, GM2 was applied, which had a higher PGA just enough to drive the structure into a slightly nonlinear stage, including minor cracking of concrete and slight yielding of extreme steel rebars. Compared to GM2, GM3 had an even higher PGA, leading to non-negligible plastic deformation as implied by a residual drift ratio of 0.87% and visible damage on the concrete. Instead of testing the column with a stronger earthquake, GM4 was then introduced to simulate an aftershock following GM3. Note that GM4 had an identical acceleration series as GM2, and thus a smaller PGA than GM3. The four GMs served different roles: GM1 was used to identify the material parameter values for the intact bridge column before other damaging earthquake GMs. GM2, GM3, and GM4 were used to explore the change in the behavior of the structure subjected to earthquakes of varying intensity levels.

After GM4, six more GMs (i.e. GM5, GM6, GM7, GM8, GM9, and GM10) were used in the shake-table test. In this study, GM10 is neglected considering that the column was significantly damaged in this GM. According to the design of the experiment, the GM5 and GM6 represented another set of mainshock-aftershock combination, where GM5 had a higher PGA (0.533g) compared to previous GMs, and the GM6 had a relatively lower PGA (0.512g). The GM5 was also the first GM tested that was beyond the seismic design level for the RC column. The original testing scheme only consisted of the first 6 GMs and the other 4 GMs were planned with higher intensities considering the good structural integrity after the first 6 GMs. The acceleration series for GM7 to GM10 were taken from the Takatori station recording during the Kobe earthquake. The GM7 represented the unscaled record and the accelerations for GM8 ~ GM10 were scaled up by 20%.

Table 4-1: Summary of the shake-table tests with the sequence of 10 Earthquake GMs [52].

GMs	Earthquake	Station	Moment magnitude	PGA (g)	Scale factor	Residual drift (before/after)	Experimental observations
GM1	Loma Prieta (1989)	Agnew State Hospital	6.9	-0.199	1.0	(0.01%/0.01%)	No observable damage in the column
GM2	Loma Prieta (1989)	Corralitos	6.9	+0.409	1.0	(-0.01%/0.05%)	Minor nonlinearity observed.
GM3	Loma Prieta (1989)	LGPC	6.9	+0.526	1.0	(0.05%/-0.87%)	Concrete cover spalled; significant nonlinearity observed.
GM4	Loma Prieta (1989)	Corralitos	6.9	+0.454	1.0	(-0.84%/-0.81%)	Minor nonlinearity observed.
GM5	Kobe (1995)	Takatori	6.9	-0.533	-0.8	(-0.81%, 1.43%)	Severe concrete spalling
GM6	Loma Prieta (1989)	LGPC	6.9	-0.512	1.0	(1.41%, 0.68%)	Severe concrete spalling
GM7	Kobe (1995)	Takatori	6.9	+0.646	1.0	(0.69%, -1.98%)	Longitudinal rebars exposed. Buckling of the rebars
GM8	Kobe (1995)	Takatori	6.9	-0.829	-1.2	(-1.97%, 1.33%)	Buckling and fracture failure of two rebars
GM9	Kobe (1995)	Takatori	6.9	+0.819	1.2	(1.33%, 3.07%)	Two more rebars fractured
GM10	Kobe (1995)	Takatori	6.9	+0.851	1.2	(3.06%, -0.33%)	Concrete core crushed

4.3 Finite element modeling of the bridge column

4.3.1 Structural geometry modeling

The tested RC bridge column is modeled in *OpenSees*, an open-source FE software framework, taking advantage of the efficient and accurate fiber beam-column elements and well-established uniaxial steel and concrete material models. In this study, two different bridge pier column models are developed: one considering fixed-end condition (i.e., the model without bond-slip) as assumed in the majority of the RC column modeling [69], and the other one considering strain penetration (i.e., the model with bond-slip) at the bottom of the bridge column. These two models are the same except the additional zero-length section element at the bottom to take into account the anchorage bond-slip [70]. Figure 4-2 shows the schematic view of the FE models of the shake-table tested RC bridge pier column. The column body is represented by 10 displacement-based fiber beam-column elements. For each element, 5 integration points (IPs) are defined using the Gaussian Lobatto integration, which has two IPs coinciding with the element end sections. On each IP, the cross-sectional behavior is represented by a discretized fiber section, including 40 (i.e., 20 × 2) unconfined concrete fibers, 280 (i.e., 20 × 14) confined concrete fibers and 18 steel fibers. Each fiber represents the behavior of the realistic uniaxial materials models, notably the stress-strain relationships for the corresponding material. Particularly, the unconfined concrete fiber is assigned with the *Concrete01* material, a uniaxial Kent-Scott-Park concrete material model that neglects the tensile strength of the concrete and has a degraded linear unloading/reloading stiffness in compression [15]. In contrast, the tensile behavior of the confined concrete is not negligible, thus the *Concrete02* material, which has a linear tension-softening branch to consider tension stiffening effect, is considered. The steel fiber to represent the longitudinal steel rebars are modeled by *Steel02*, a uniaxial Giuffre-Menegotto-Pinto steel material model, which is capable of representing the isotropic strain hardening. Note that the fiber-section for the displacement-based fiber beam-column elements assume perfect bonding between steel and the surrounding concrete in the column body. Furthermore, perfect bonding is also assumed in the column-footing connection for the model without bond-slip, and thus the bottom of the column is fixed.

By contrast, the model with bond-slip contains a zero-length section element, which is introduced to take into account the bond-slip or strain penetration effects in the column bottom-footing connection, namely the fixed-end rotation ([31] [70]). This element has a conventional fiber section based on perfect bonding with the plane section assumption enforced, but it requires regularized uniaxial material models as proposed by Zhao and Sritharan [31]. Specifically, the *Steel02* material model in steel fiber is replaced by the *bond-SP01* material model, which is to characterize the stress-slip relationship. To accommodate the large deformation or rotation in the zero-length section element, the concrete model (i.e., the *Concrete02* material) is regularized to have a larger strain capacity or crushing strength due to additional confinement effects expected from the footing.

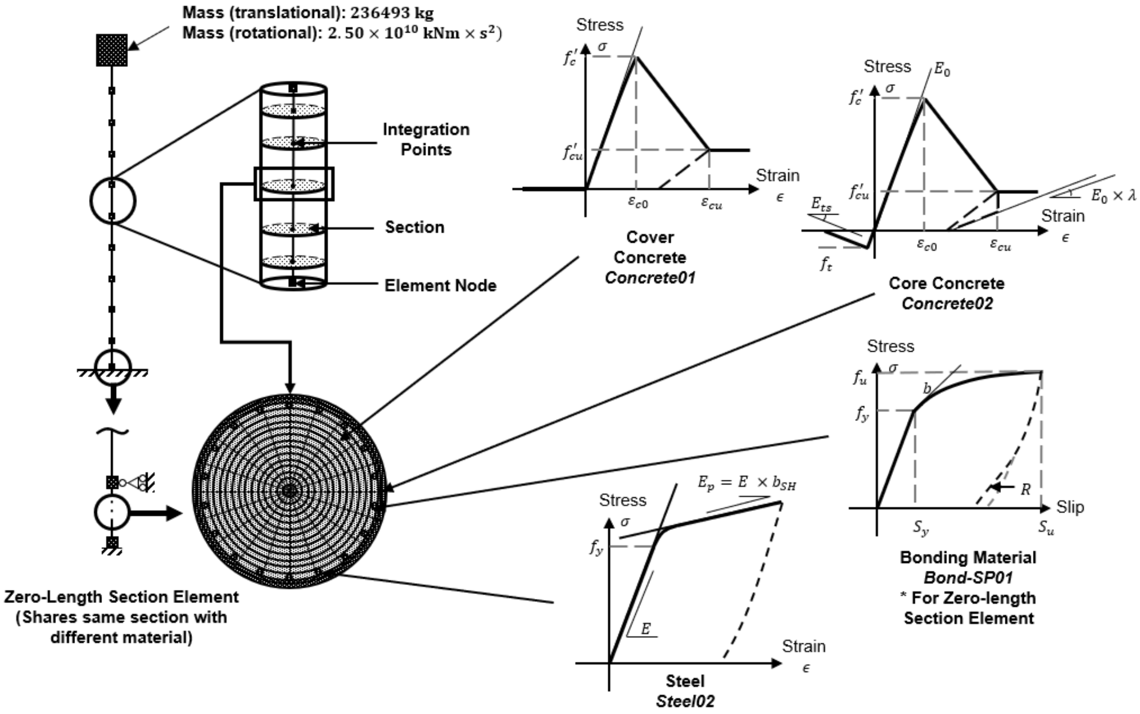

Figure 4-2: Schematic view for the FE model of the shake-table tested RC bridge pier column

The aforementioned modeling scheme provides relevant information for the FE model to determine the restoring force due to the deformation of the dynamic system, i.e., the bridge pier column subjected to earthquake excitations. The inertia of superstructure, represented by the concrete block in the test, is modeled by a concentrated mass and a rotational mass of inertia at the top of the column. The mass of the column is discretized and distributed to each node of the column according to the tributary length and the concrete mass density (2403 kg/m^3). The energy dissipation of the dynamic system is modeled by a Rayleigh damping model with mass and initial-stiffness proportional components defined based on the first two vibration modes with a damping ratio of 2.0% each. This is to account for the additional energy dissipation apart from the hysteretic energy embodied in the nonlinear material models. The acceleration series of the aforementioned earthquake records will be used as the seismic inputs as a uni-directional excitation at the bottom of the column.

4.3.2 Material model parameters

As typical forward FE modeling, the material properties obtained from the coupon tests in the shake-table test program is fully utilized to define the material models, here mainly for steel bars and the unconfined concrete (i.e., cover). Thus, the known model parameters include the elastic modulus E_s, the yield strength f_y, and the post-yield hardening ratio b_{sh} for the steel rebar, as well as the maximum compressive strength f_c' and the corresponding strain ε_c for the unconfined concrete.

Since no experimental test was performed to determine the material properties of the confined core concrete in the test program, well-known empirical relationships [17] are used here to determine the initial estimate of confined concrete behavior. Based on the confinement status and unconfined concrete properties, the two key material parameters: the peak compressive strength $f'_{c/core}$ and the corresponding strain $\varepsilon_{c/core}$ for confined concrete are estimated according to Eq. (4–1) and Eq. (4–2), respectively,

$$f'_{c/core} = f'_c\left(2.254\sqrt{1+\frac{7.94f'_l}{f'_c}}-2\frac{f'_l}{f'_c}-1.254\right) \tag{4–1}$$

$$\varepsilon_{c/core} = \varepsilon_c\left[1+5\left(\frac{f'_c}{f'_{c/core}}-1\right)\right] \tag{4–2}$$

where f'_l represents the effective lateral confining stress, defined by the confinement status characterized by the confined area of concrete, the yield strength, the bar diameter, and the spacing of stirrups.

Additionally, other material model parameters associated with the post-peak behavior and the tensile behavior of concrete are determined empirically. As such, the concrete crushing strength f'_{cu} and ε_{cu} of the unconfined and confined concrete are assumed to be 20% of the corresponding peak compressive strength and three times as the strain at the peak compressive stress, respectively. The tensile behavior for the core concrete is defined (as shown in Figure 4-2) with the tensile strength f_t= 10% of the maximum compressive strength, the unloading stiffness ratio λ = 0.1, and the tension softening stiffness E_{ts} = 10% of the elastic modulus of concrete. To sum up, the initial material model parameters for the fiber-based FE model without bond-slip are summarized in Table 4-2.

Table 4-2: Material parameter definition for column fiber section

	Column section	Zero-length section
Cover concrete fiber material	*Concrete01*	*Concrete01*
Maximum compressive strength (f_c')	40.9 MPa [1]	40.9 MPa [1]
Strain at maximum strength (ε_c)	0.0026 [1]	0.0026 [1]
Concrete crushing strength (f_{cu}')	8.18 MPa [2]	8.18 MPa [2]
Strain at crushing strength (ε_{cu})	0.0078 [2]	0.0078 [2]
Core concrete fiber material	*Concrete02*	*Concrete01*
Maximum compressive strength (f_c')	50 MPa [3]	50 MPa [3]
Strain at maximum strength (ε_c)	0.0055 [3]	0.0055 [3]
Concrete crushing strength (f_{cu}')	10 MPa [2]	10 MPa [2]
Strain at crushing strength (ε_{cu})	0.0165 [2]	0.0165 [2]
Unloading stiffness ratio (λ)	0.1 [2]	-
Tensile strength (f_t)	5 MPa [2]	-
Tension softening stiffness (E_{ts})	3102.64 MPa [2]	-
Steel fiber material	*Steel02*	*bond-SP01*
Yield strength (f_y)	519 MPa [1]	519 MPa [1]
Elastic modulus (E_s)	196 GPa [1]	-
Initial hardening ratio (b_{sh})	0.01 [1]	-
Slip at yield strength (S_y)	-	0.762 mm [3]
Ultimate strength (f_u)	-	706 MPa [1]
Slip at ultimate strength (S_u)	-	33.7 mm [2]
Hardening ratio of slip vs. stress response (b)	-	0.4 [2]
Pinching factor (R)	-	0.7 [2]
Note: [1]: In-site material tests [2]: Empirical estimation [3]: Formulation estimation		

The model parameters for the zero-length section element used to account for bond-slip are not directly observable or measurable. As recommended by Zhao and Sritharan [31], the fiber section for the bond-slip element is similar to the fiber section for the column body except the *bond-SP01* material for steel fibers and the larger value of the crushing strength ($f'_{cu} = 0.8f'_c$) of the cover and core concrete. The yield strength for *bond-SP01* is the same as that for steel, and the slip at the yield strength, S_y, is estimated based on Eq.(4–3):

$$S_y(\text{mm}) = 254\times[\frac{d_b(\text{mm})}{8437}\frac{f_y(\text{MPa})}{\sqrt{f_c'}(\text{MPa})}(2\alpha+1)]^{1/\alpha}+0.34(\text{mm}) \qquad (4\text{–}3)$$

in which, d_b = the rebar diameter in mm, f_y = the yield strength of steel in MPa, f'_c= the compressive strength of the surrounding concrete in MPa, and α = the local bond-slip relation factor of 0.4 in accordance with CEB-FIP Model Code 90.

4.3.3 Comparison of FE models with and without considering bond-slip

To evaluate the improvement on modeling accuracy after considering bond-slip, nonlinear FE models with and without considering bond-slip was developed to simulate the dynamic response of the bridge column subjected to GM1. For each model, the FE predicted drift response was compared with the experimental data.

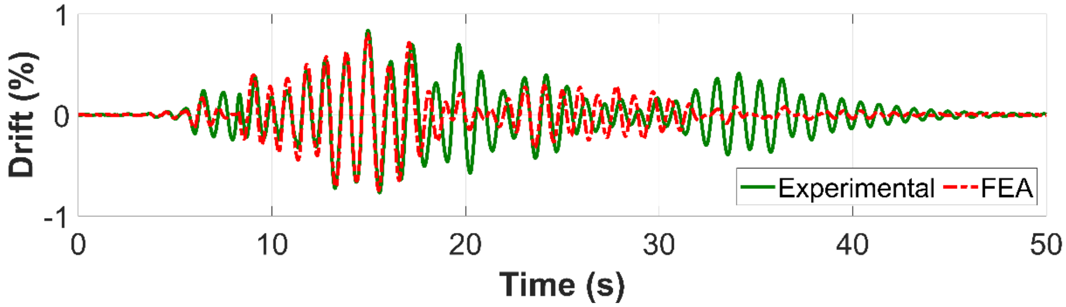

Figure 4-3: Comparison of simulated response of the FE model without considering bond-slip and recorded experimental response

As can be observed in Figure 4-3, the FE prediction from the model without considering bond-slip failed to achieve good correlation with measurement during the GM1. Specifically, the prediction accuracy is low for the seismic response after 18 seconds, where the prediction is out of phase and the structural response is underestimated from 30 to 40 seconds.

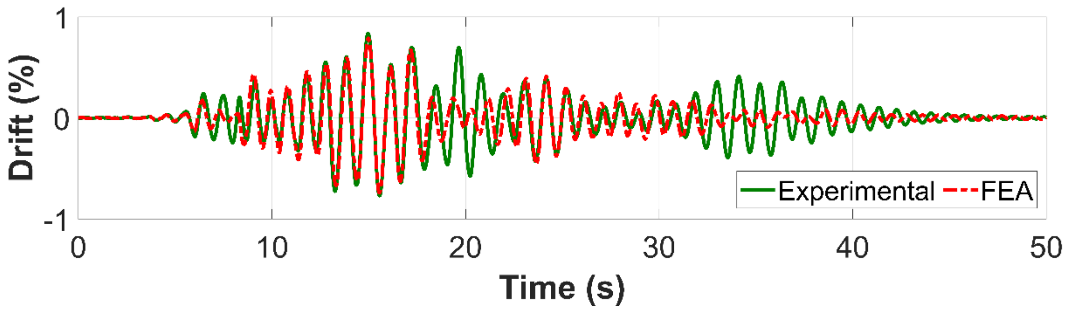

Figure 4-4: Comparison of simulated response of the FE model considering bond-slip and recorded experimental response

On the other hand, a slightly higher prediction accuracy can be observed for the model considering bond-slip (see Figure 4-4), where the first 18 seconds has achieved a slightly better matching comparing to the model without considering bond-slip. Moreover, such model also achieved a good match with the experimental data in 22-32 seconds.

To better assess the prediction accuracy of each model, the *RRMSE* (relative root mean square error as defined in Eq. (4–4)) is introduced to quantify the discrepancy between the simulated and experimental responses:

$$RRMSE = \sqrt{\frac{\sum_{\mathrm{i=1}}^{\mathrm{n}}\left(\boldsymbol{y}_{Exp}^{i} - \boldsymbol{y}_{FEA}^{i}\right)^{2}}{\sum_{\mathrm{i=1}}^{\mathrm{n}}\left(\boldsymbol{y}_{Exp}^{i}\right)^{2}}} \tag{4–4}$$

where $\boldsymbol{y}_{Exp}^{\boldsymbol{i}}$represents the experimental response and $\boldsymbol{y}_{FEA}^{\boldsymbol{i}}$ represents the FE model response. It can found that the model with bond-slip reduced the *RRMSE* Such decrease in the *RRMSE* shows that the accuracy of the model has improved after the inclusion of the bond-slip effect and implies the accuracy of the FE model relies on appropriate modeling of bond-slip.

4.4 FE model updating with simulated data

Considering the measurement error in the experimental data and inaccuracies in the FE modeling, it is important to verify the performance of the FEMU framework using simulated data before proceeding to FEMU using experimental data. To this end, nonlinear FEMU is conducted for the bridge column model considering bond-slip using simulated data for GM1 and GM2.

The measurements used in the FEMU are the displacement history at the top of the column (or drift ratio) and the strain responses from extreme core concrete fibers located at 527 mm, 1143 mm, and 1746 mm above the upper surface of the footing. They are generated by contaminating the FE simulated responses with additive Gaussian white noise (AGWN) of three different noise levels: the noise standard deviation = 5%, 7%, and 10% of the peak responses (see Figure 4-5 for the simulated measurements of drift ratios during GM1 and GM2).

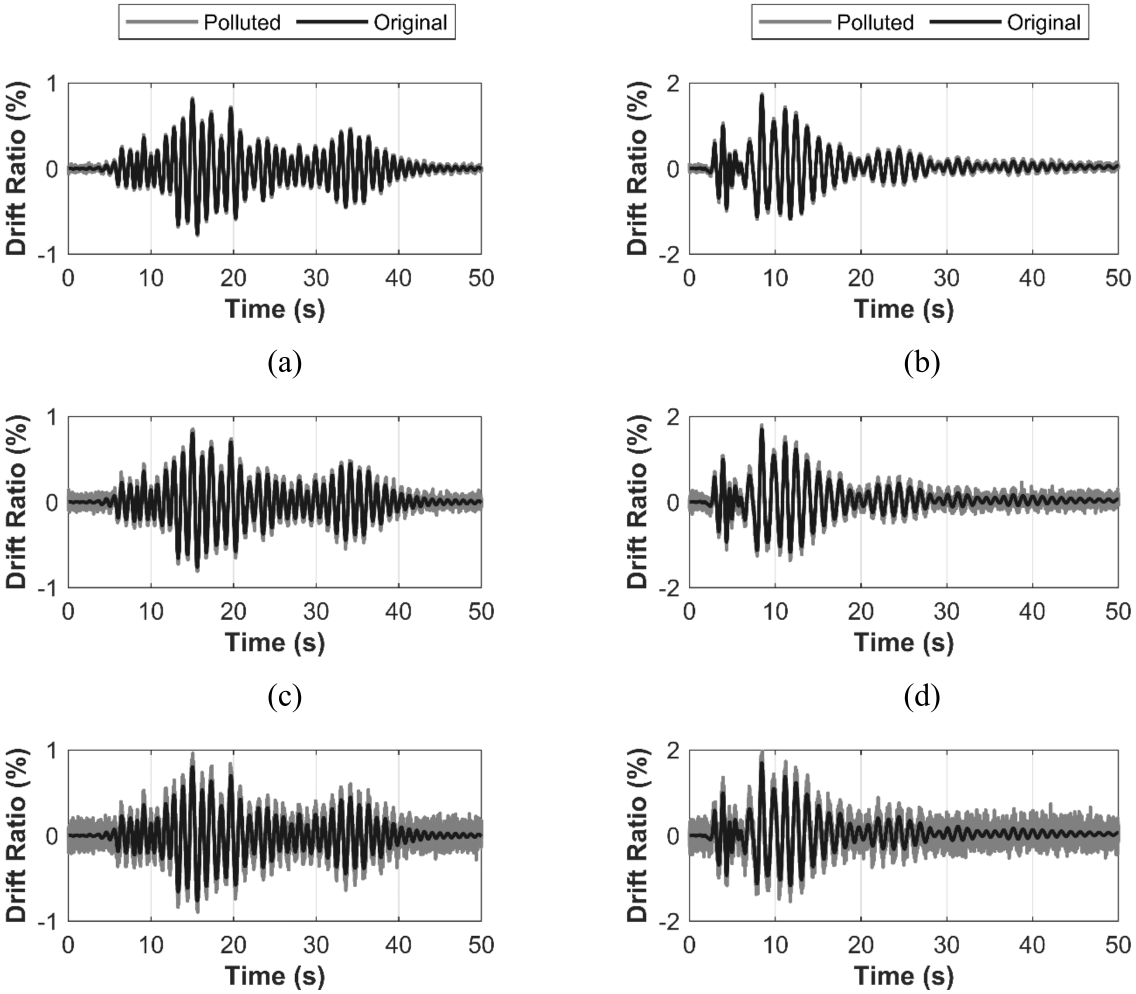

(a) (b)

(c) (d)

(e) (f)

Figure 4-5: Simulated drift ratio measurements used for FEMU with low noise level (5%) (a) GM1, (b) GM2; medium noise level (7%), (c) GM1, (d) GM2; and high noise level (10%) (e) GM1, (f) GM2

For the FEMU cases considered here, the core concrete parameter ε_c and bond-slip parameter S_y are selected to be estimated (i.e., assumed unknown), i.e., $\mathbf{X} = [\varepsilon_c, S_y]$. In FEMU, the initial model parameters considered (i.e., $\mathbf{X}^{ini} = [0.00312, 94.36\ mm]$) , and the other algorithmic parameters for the FEMU framework are defined as shown in Table 4-3. Note that the covariance matrix $\boldsymbol{P}_0^{xx}$ can be defined using the initial guess of the mean vector of $\mathbf{X}^{ini}$ and the coefficients of variation for ε_c and S_y i.e.,δ_1 and δ_2, respectively, and the initial correlation coefficient between the two parameters ρ_{12}.

Table 4-3: Algorithmic parameter values of FEMU for the bridge pier column using simulated data

	$\boldsymbol{P}_0^{xx}$			$\boldsymbol{Q} = \mathbf{X}^{ini}\mathbf{diag}(\mathrm{Q}_1, \mathrm{Q}_2)$		$\boldsymbol{R} = \mathbf{diag}(\mathrm{R}_1, \mathrm{R}_2, \mathrm{R}_2, \mathrm{R}_2)$	
Factor	δ_1	δ_2	ρ_{12}	Q_1	Q_2	R_1	R_2
GM1	0.1	0.1	0.01	10^{-10}	10^{-10}	10^{-8}	10^{-16}
GM2	0.1	0.1	0.01	10^{-10}	10^{-10}	10^{-8}	10^{-16}

Note: $\mathbf{X}^{ini}$ in FEMU with GM2 as input is defined as $\mathbf{X}^{ini} = [0.00234, 80.88\ mm]$ for low noise level, $\mathbf{X}^{ini} = [0.00234, 50.55\ mm]$ for medium noise level, and $\mathbf{X}^{ini} = [0.00234, 16.85\ mm]$ for high noise level.

The parameter updating histories for the three cases using seismic data from GM1 are shown in Figure 4-6, including the mean values of the material parameters and the boundaries of the 95% confidence interval. As can be observed, the mean values of parameters ε_c and S_y at all three cases successfully converged to the true values.

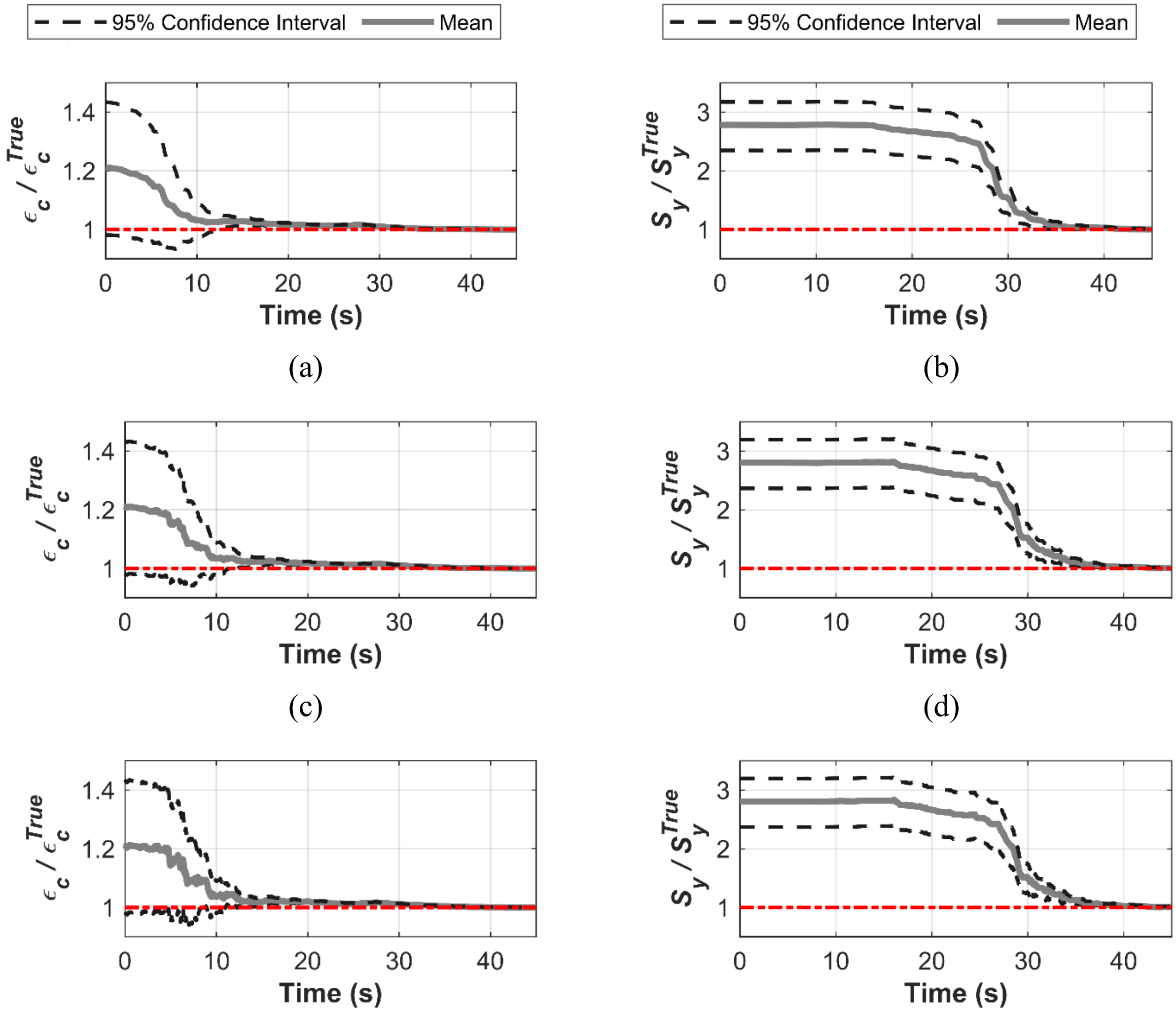

(a) (b)

(c) (d)

(e) (f)

Figure 4-6: Model parameter updating histories under GM1 using simulated data with low noise level (5%): (a) ε_c, (b) S_y; medium noise level (7%): (c) ε_c, (d) S_y; and high noise level (10%): (e) ε_c, (f) S_y

In the FEMU cases using simulated data from GM2, various initial guesses are studied to verify the performance of the FEMU framework. The initial values of the modeling parameters at each case are chosen intentionally far from their true values to various degrees. The updating histories for the three cases are shown in Figure 4-7, where all parameters converged to the true values with narrow 95% confidence intervals, even different initial guesses for the parameters are used.

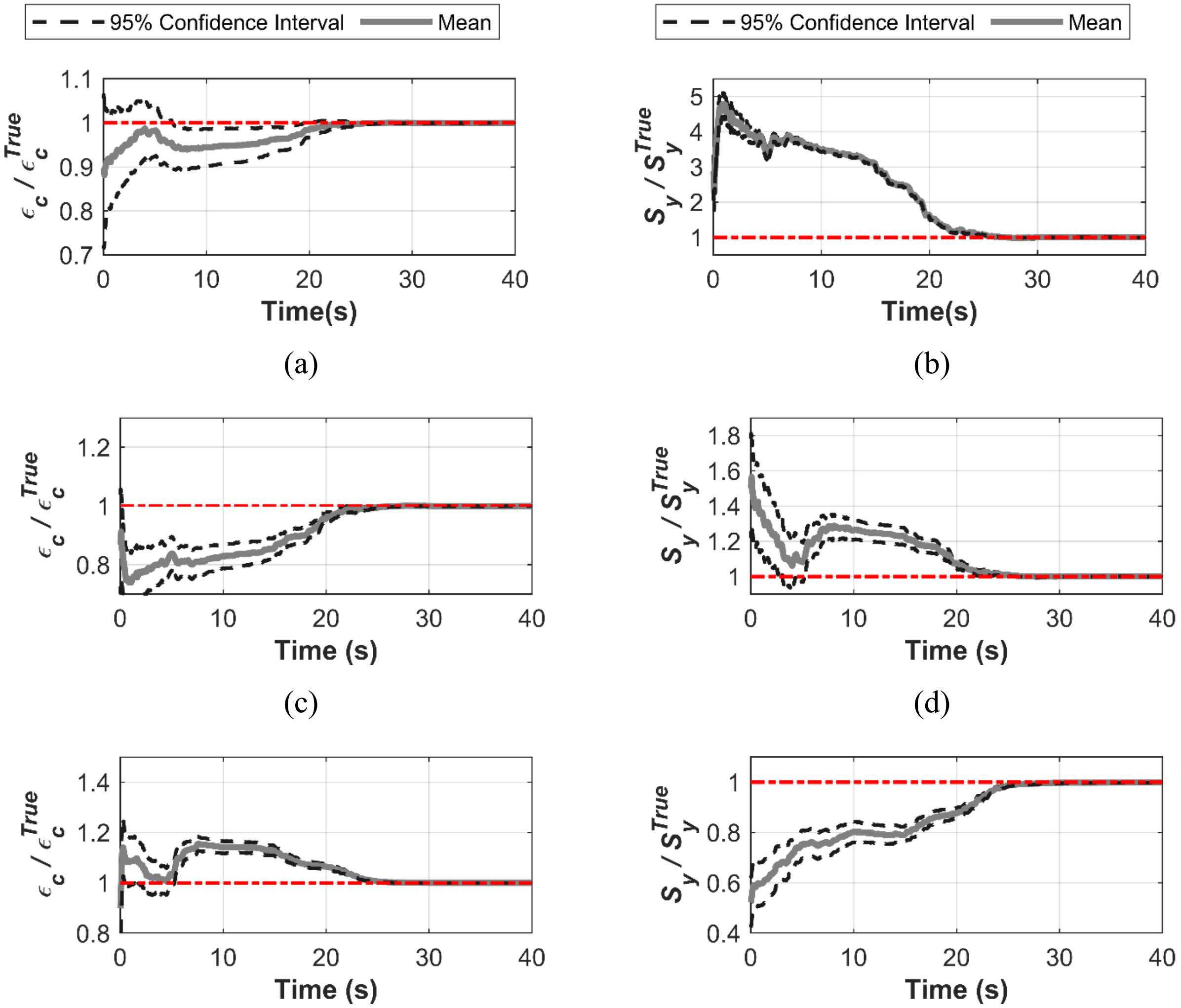

(a) (b)

(c) (d)

(e) (f)

Figure 4-7: Model parameter updating histories under GM2 using simulated data with low noise level (5%): (a) ε_c, (b) S_y; medium noise level (7%): (c) ε_c, (d) S_y; and high noise level (10%): (e) ε_c, (f) S_y

4.5 FE modeling updating with experimental measurements

4.5.1 FE model selection and updating for GM1

Two alternative FE models (i.e., model with bond-slip and model without bond-slip) are considered in this section. They are both updated using the experimental data from the shake-table test subjected to GM 1 to illustrate the importance of considering bond-slip in FE modeling for the tested bridge column. For the model with bond-slip, a comprehensive set (30 in total) of model parameters include 3 material model parameters for *Steel02*, 12 (= 4 × 3) and 7 (= 7 × 1) material parameters for *Concrete01* and *Concrete02* (for bond-slip element and column body elements), respectively, 6 material parameters for *bond-SP01*, and 2 Rayleigh damping parameters. For the model without bond-slip, there are a total of 16 model parameters by excluding those for the bond-slip element. Although the inclusion of all model parameters in the model updating process would increase the model flexibility, it would also increase the computational cost and the difficulty in identifiability and interpretability. As such, a one-at-a-time sensitivity analysis is performed to determine the relative importance of model parameters in predicting the seismic response for GM 1, and a minimum number of model parameters will be updated to achieve higher processing speed and a better model interpretability.

In the sensitivity analysis, each model parameter (θ) is perturbed by $\pm\Delta\theta$ around the center value ($\theta = \theta_0$). Sequentially, the FE model is evaluated at $\theta = \theta_0 \pm \Delta\theta$ for each model parameter when other parameters are fixed at the center values. The simulated response (e.g., pier top drift), y^p, is compared with the reference response, y^c, which is obtained from the FE model evaluated at $\theta = \theta_0$. The difference is defined by the relative root-mean-square error (*RRMSE*), see Eq (4–5), as a measure of sensitivity with respect to the parameter θ.

$$RRMSE = \sqrt{\frac{\sum_{\mathrm{i=1}}^{\mathrm{N}}\left(y_i^p - y_i^c\right)^2}{\sum_{\mathrm{i=1}}^{\mathrm{N}}(y_i^c)^2}} \tag{4–5}$$

in which the subscript i indicates the analysis time step, and *N* represents the total analysis steps for seismic response simulations. For a fair comparison, the perturbation $\Delta\theta$ is taken as one standard deviation of the parameter for those variables with statistics available, such as the yield strength of steel, the peak compressive strength of concrete among others (e.g.,[71]–[74]). In contrast, 10% of its center value is used for those variables without statistical information available, such as the unloading stiffness ratio (λ) for concrete.

The sensitivity analysis results for the models without and with bond-slip are shown through the tornado plots in Figure 4-8 (a) and (b), respectively. It is observed that the elastic modulus of the steel (E_s), the concrete cover parameters (f_c' and ε_c), and the core concrete parameters (f_c' and ε_c), play significant roles for both models under GM 1 with a low intensity level. This is because these parameters highly affect the initial stiffness of the column. However, for the model without bond-slip, the tensile strength (f_t) and the tension softening stiffness (E_{ts}) of the core concrete are the additional two important parameters. By contrast, for the model with bond-slip, the following important parameters are the bond-slip yield strength (f_y) and the corresponding slip (S_y).

According to the sensitivity analysis results discussed above and properties obtained from material coupon tests available from the same experimental program, the main parameters for nonlinear FEMU are selected. Specifically, the elastic modulus of steel (E_s), the yield strength of steel (f_y), the peak compressive strength of concrete (f_c'), and the corresponding strain (ε_c) can all be determined directly from the measurements. For the core concrete model parameters (f_c' and ε_c), they are both related to the stiffness of the core concrete and thus only one (ε_c) is considered for updating when the seismic intensity is low (e.g. GM1).

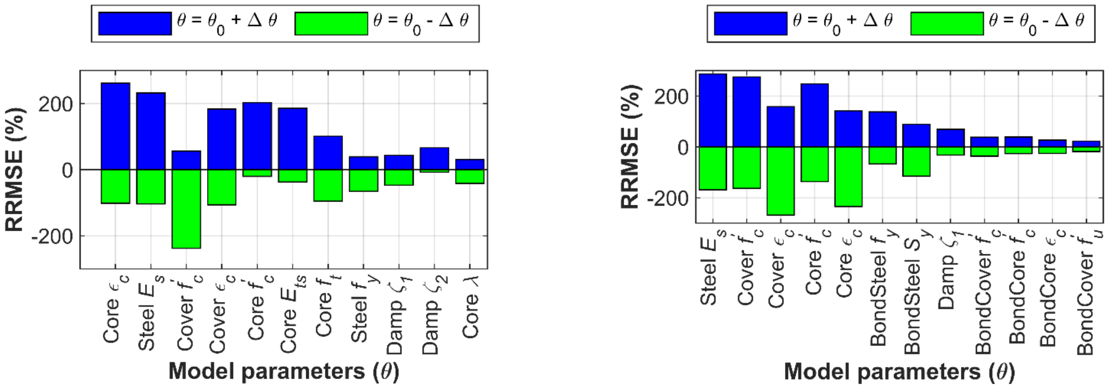

(a) (b)

Figure 4-8: Sensitivity analysis results for the two alternative models under GM1 for: (a) the model without bond-slip, and (b) the model with bond-slip

For the model without bond-slip, the other two model parameters of secondary importance are also included for FE modal updating. For the model with bond-slip, the bond-slip yield strength (f_y) and the corresponding slip (S_y) of secondary importance are closely related to the stiffness of the bond-slip, and only one (e.g., S_y) is considered for updating when the seismic intensity is low (e.g. GM1).

Using the UKF-based updating method presented earlier, the two models considered in this section are updated using the experimental data during the shake-table test for GM1. Four response measurements are used as experimental observations, including the displacement history at the bridge pier top and the three strain histories along the bridge bottom at various locations. Note that to reduce the computational cost, only 50 seconds of GM1 with strong signal values were used.

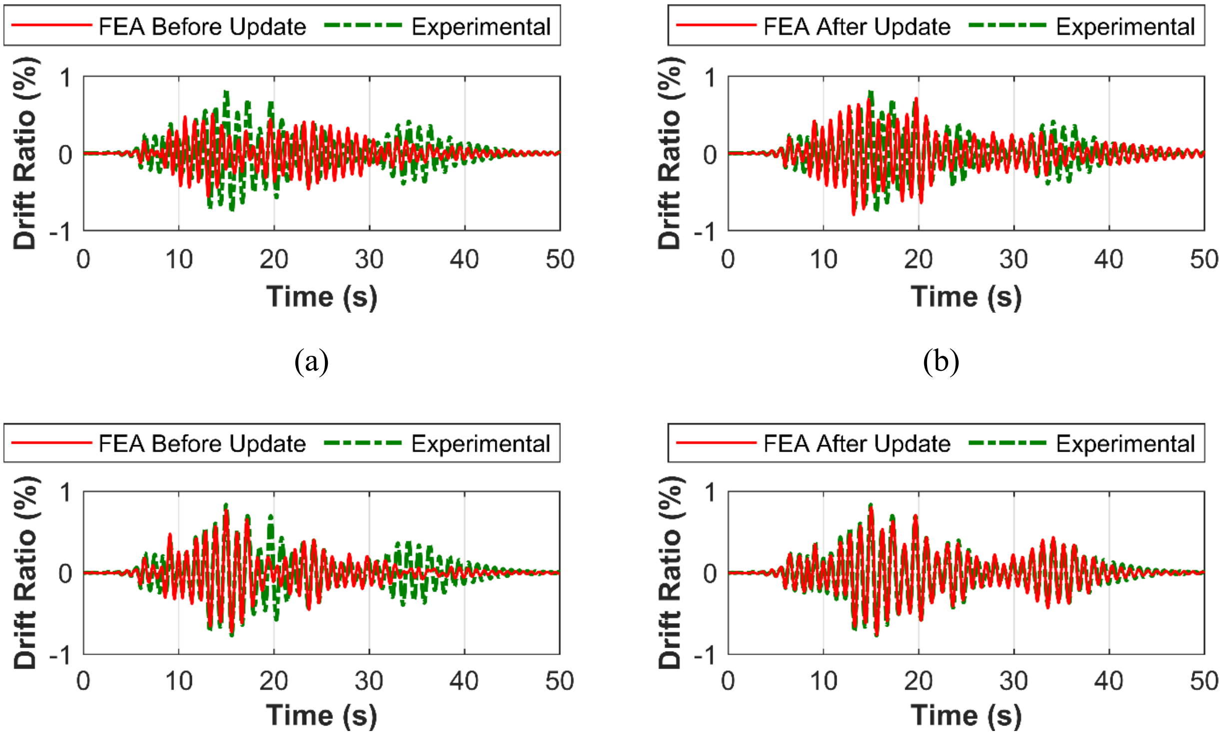

(a) (b)

(c) (d)

Figure 4-9: Comparison of the nonlinear FEMU results by means of the bridge pier drift ratio history: RC column model without bond-slip (a) before update, (b) after update; RC column model with bond-slip (c) before update, (d) after update

The comparison of the bridge pier drift ratio histories before and after the FEMU are shown in Figure 4-9 (a) and (b) for the model without bond-slip, and similar results are shown in Figure 4-9

(c) and (d) for the model with bond-slip. It is observed that the UKF-based updating method improved the FE-prediction using the model without bond-slip compared with the initial FE-prediction before update, but no satisfactory prediction is achieved. In contrast, the updated FE-prediction using the model with bond-slip provides nearly perfect correlation with the experimental observation. It is worth noting that the initial model with bond-slip even provided better prediction than the initial and updated model without bond-slip. The comparison shows that the importance of model updating and the significance of considering bond-slip in this column modeling.

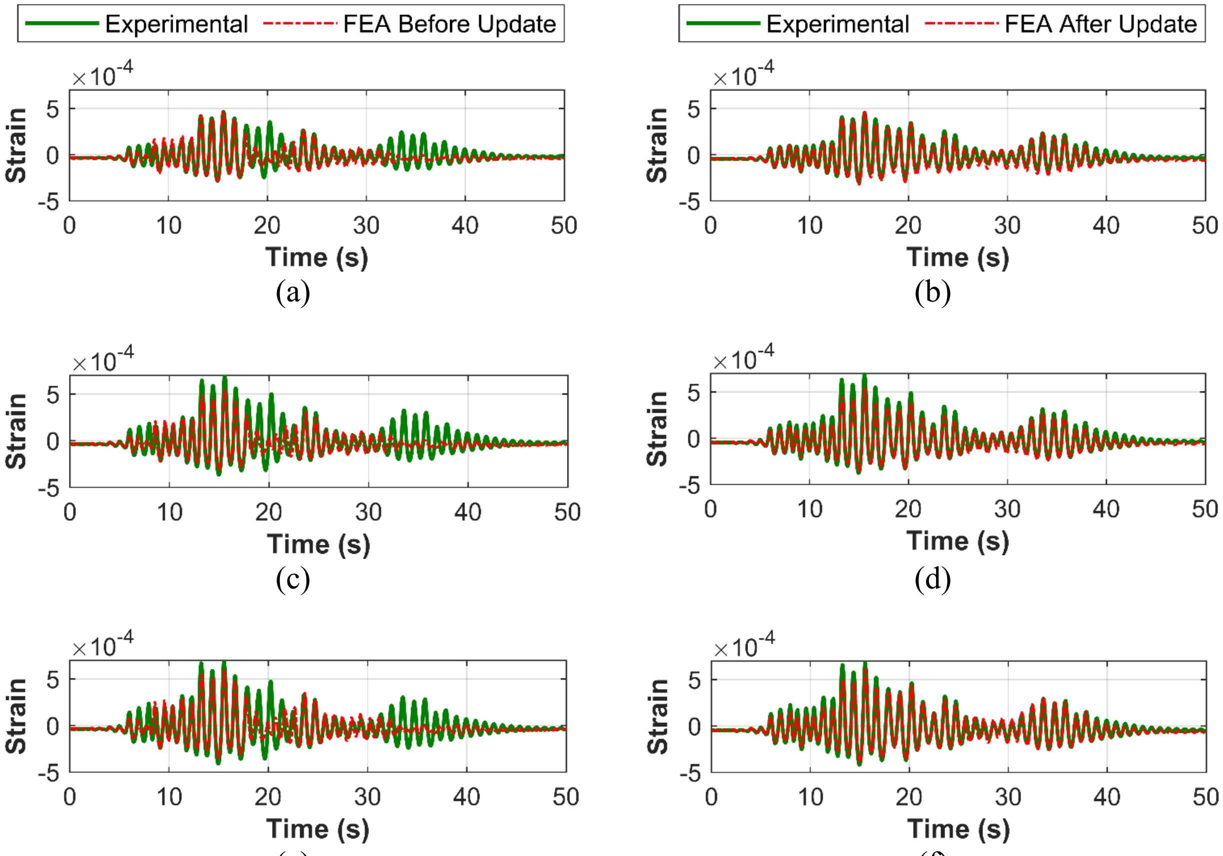

(a) (b) (c) (d) (e) (f)

Figure 4-10: Comparison of the FE-predicted and measured strain histories at three different locations in GM1: 1746 mm above footing (a) before update, (b) after update; 1143 mm above footing (c) before update, (d) after update; and 527 mm above footing (e) before update, (f) after update

To further show the accuracy achieved using the updated model with bond-slip, Figure 4-10 presents the comparison of the FE prediction and experimental measurements by means of the local strain histories. It shows the updated FE model with bond-slip also significantly improved the prediction of the strain histories recorded, and it reproduced nearly perfectly correlated results with the experimental observations. This observation also confirms the better predictability and interpretability of the model with bond-slip considered.

Figure 4-11 shows the updating history for the two parameters considered in the FE model with bond-slip, namely, the strain corresponding the peak compressive strength of core concrete ε_c, and the slip corresponding to the yield of the bond-slip yield strength (S_y). As shown in Figure 7 (a), the value of ε_c almost doubled after the updating for GM1, which indicates an over-estimation of empirical relationship expressed in Mander's equation [17]. As for the bond-slip parameter, no significant change was observed on the value of S_y after the updating of GM1, indicating the equation proposed by Zhao and Sritharan [31] provided an accurate approximation on the slip value of S_y. Note that initial guess of the uncertainty in the two model parameters was reduced by the measurements as well.

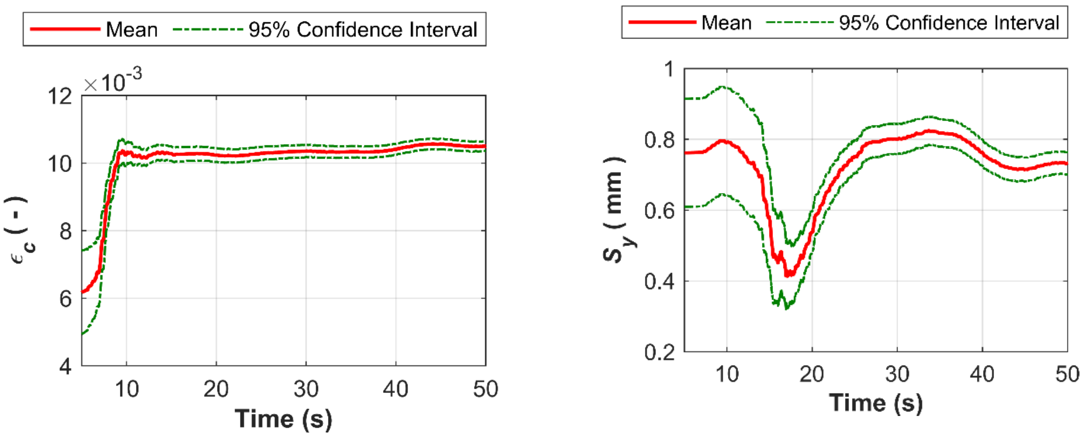

(a) (b)

Figure 4-11: Model parameter updating histories in GM1 for: (a) core concrete strain at maximum strength (ε_c), and (b) bond-slip at yield strength (S_y)

4.5.2 Nonlinear FE model updating for other GMs

4.5.2.1 Parameter sensitivity analysis

To select the critical parameters for update in the model with bond-slip subject to the GMs with various intensity levels, a sensitivity analysis is performed to quantify the importance of the modeling parameters. The sensitivity analysis results for the FE model adopted (i.e., model with bond-slip) subject to GM2, GM3, and GM4, are shown through the tornado plots in Figure 4-12 (a), (b), and (c), respectively. It is observed that the most important parameters (i.e., the top eight) are the same except the slight change in the ranking for GM2 and GM4 with relative low intensities. Following the same reasoning as for GM1, the two important and uncertain parameters, the strain corresponding the peak compressive strength of core concrete (ε_c) and the slip (S_y) corresponding to the bond-slip yield strength, are considered for updating.

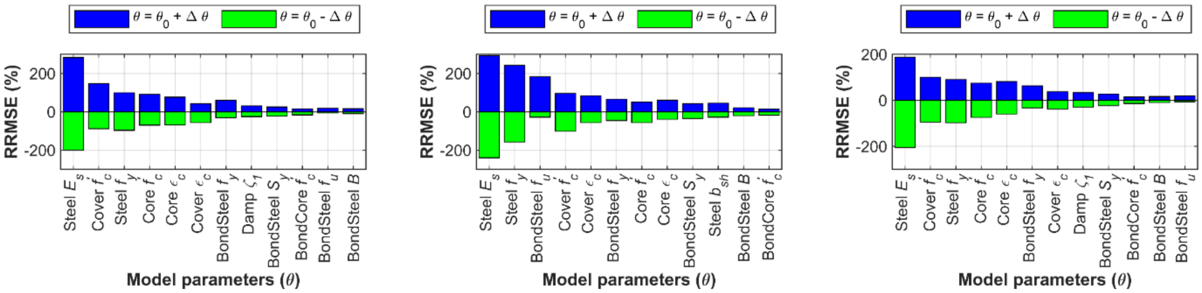

(a) (b) (c)

Figure 4-12: Sensitivity analysis results for the model with bond-slip under: (a) GM2, (b) GM3, and (c) GM4

Different from GM1, in which the bridge column was considered as damage-free, the bridge column subjected to sequential GMs (e.g. GM2, GM3, and GM4) are considered as degraded structures with micro-damage due to earlier GMs applied. Note that model parameters are considered as time-invariant within one GM record, but they are allowed to vary from record to record to indirectly account for the softening effect caused by the pre-existing damage to core concrete and the bond-slip behavior (e.g., through a different ε_c and S_y).

4.5.2.2 Nonlinear FE model updating for GM2

Similar to the case for GM1, half of the 100-second GM2 was considered and the FEMU analysis was terminated early to reduce the computational cost. Figure 4-13 shows FE-predicted responses before and after FE model updating with comparison to the experimental measurements for GM2. The initial model with the updated parameters from GM1 showed poor predictions (see Figure 4-13 a, b, c, and d).

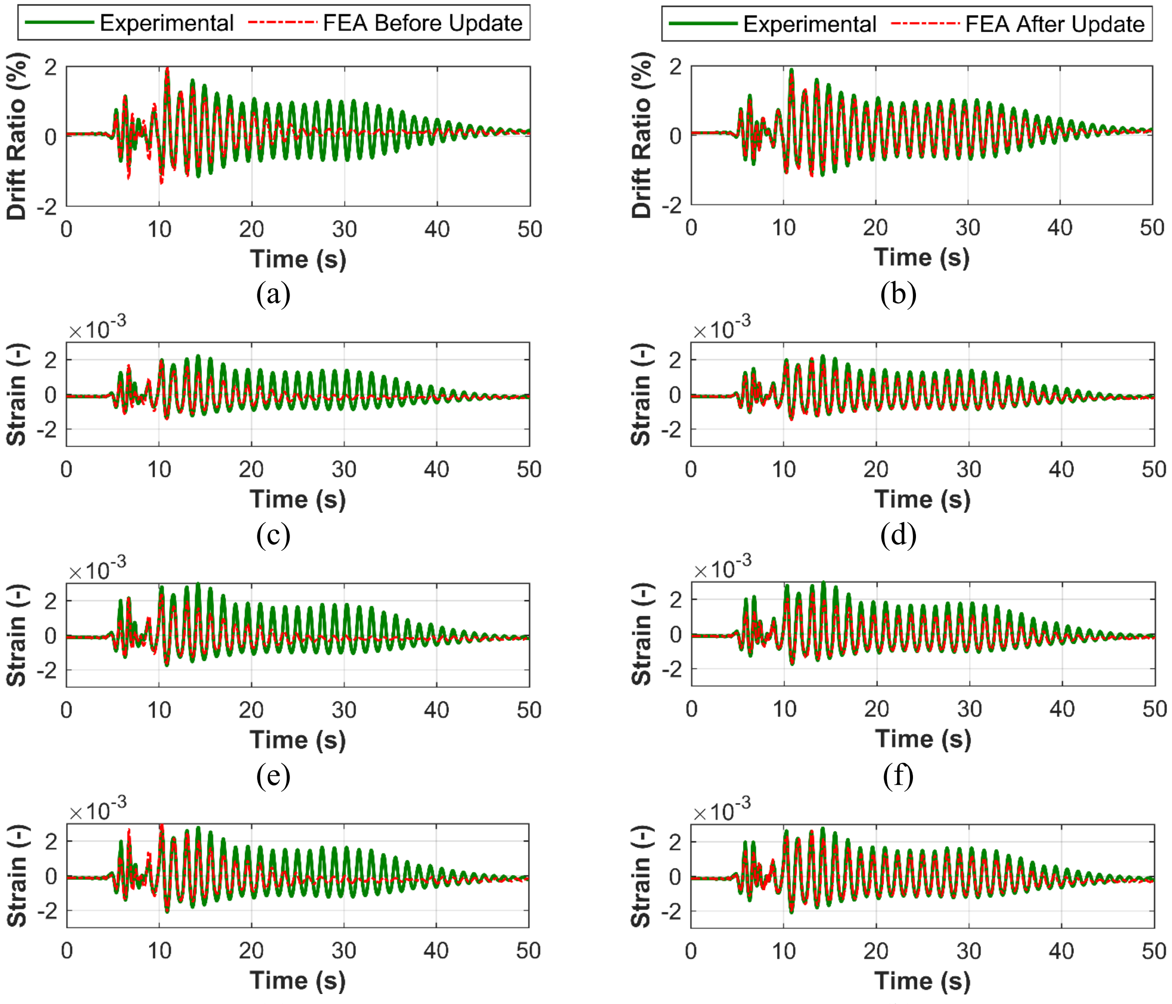

(a) (b) (c) (d) (e) (f) (g) (h)

Figure 4-13: Comparison of the FE-predicted and measured strain histories at three different locations under GM2: 1746 mm above footing (a) before update, (b) after update; 1143 mm above footing (c) before update, (d) after update; and 527 mm above footing (e) before update, (f) after update

The FEMU has improved the FE-predictions significantly, and both the global response (i.e., drift ratio) and the local responses (i.e., strains at three locations) are predicted excellently well in frequency contents, except a slight overall underprediction in amplitude. The parameter updating histories are shown in Figure 4-14, which shows that the estimation of both parameters almost converged with large increments compared to the initial values or the updated parameter values from GM1.

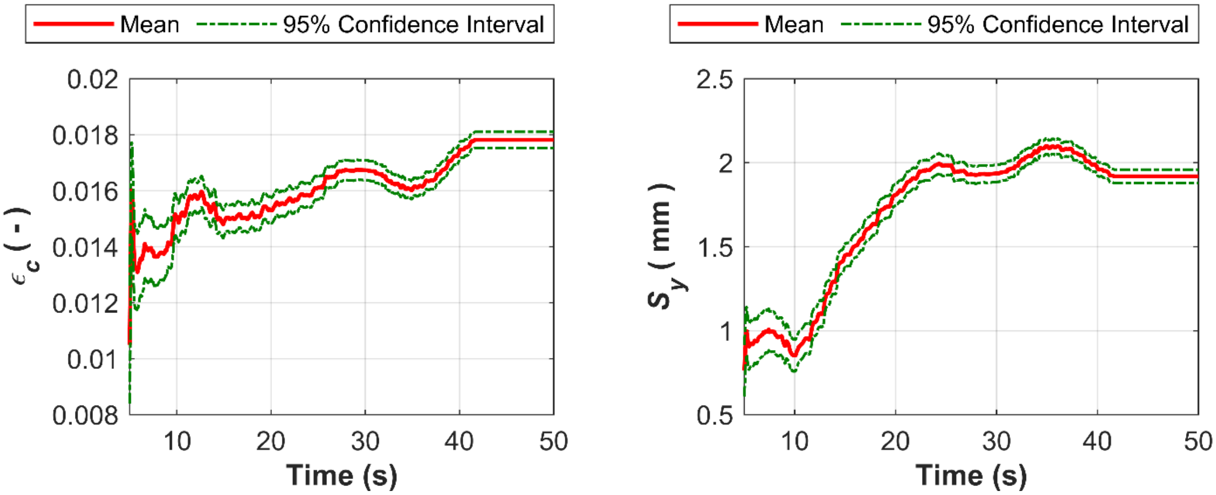

(a) (b)

Figure 4-14: Model parameter updating histories in GM2 for: (a) core concrete strain at maximum strength (ε_c), and (b) bond-slip at yield strength (S_y)

4.5.2.3 Nonlinear FE model updating for GM3

Similarly, a subset (50 seconds) of GM3 acceleration series is considered by cutting off the original record with negligible magnitude. Figure 4-15 shows FE-predicted responses before and after FEMU with comparison to the experimental measurements for GM3. The FE model with initial model parameters (with the updated parameters estimated from GM2) showed reasonably good predictions of the drift ratio history and the strain response at GLEN08I, but the significant underprediction of the other two strain responses (see Figure 4-15 a, c, e, and g). The implementation of the FEMU framework has slightly improved the FE-predictions in the response amplitude, including the residual drift ratio (see Figure 4-15 b, d, f, and h).

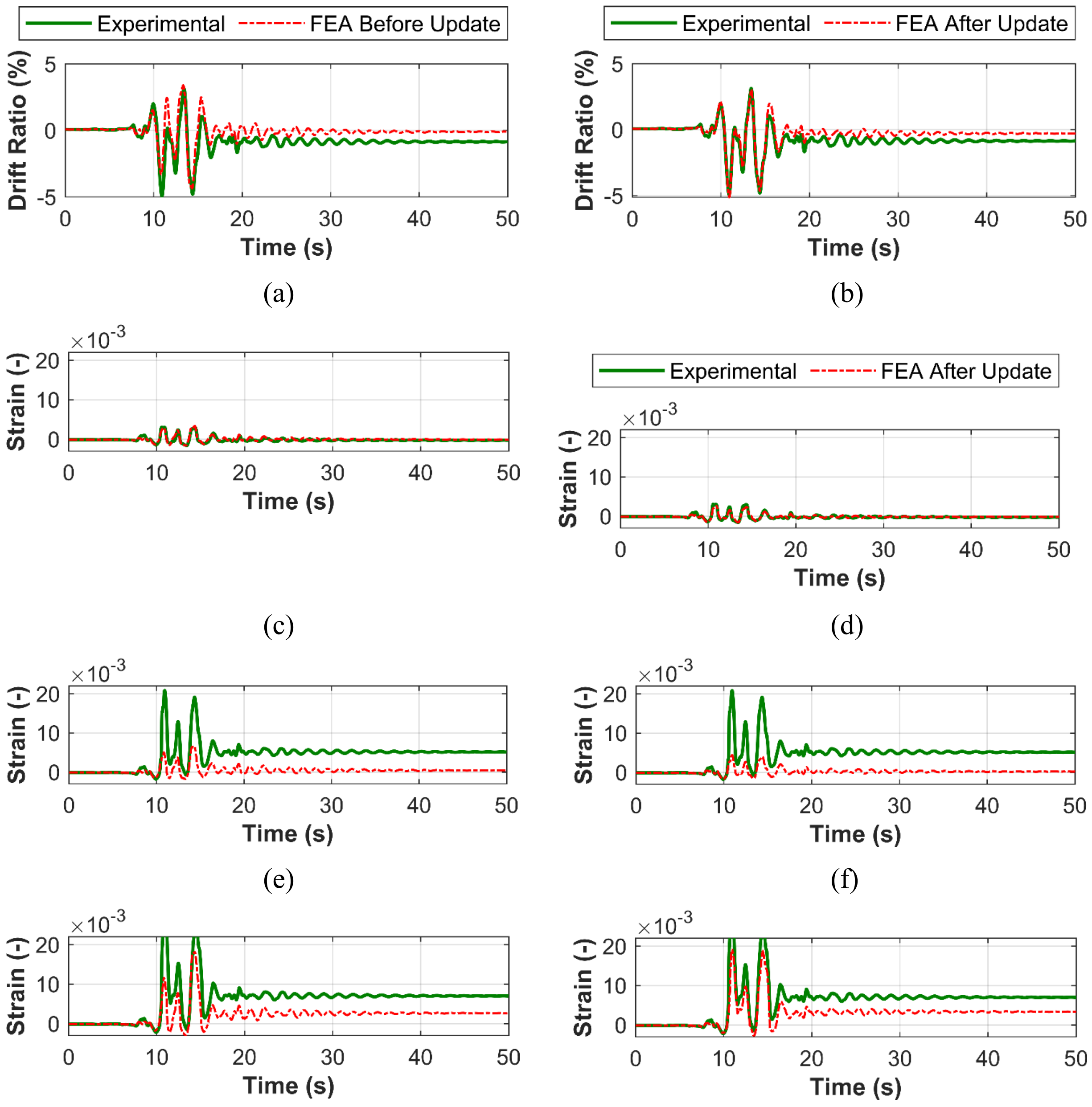

(a) (b)

(c) (d)

(e) (f)

(g) (h)

Figure 4-15: Comparison of the FE-predicted and measured strain histories at three different locations under GM3: 1746 mm above footing (a) before update, (b) after update; 1143 mm above footing (c) before update, (d) after update; and 527 mm above footing (e) before update, (f) after update

The parameter updating histories are summarized in Figure 4-16, which shows that the estimation of three parameters stabilized with large increments. Note that the newly added parameter b_{sh} for steel fiber converged to the empirical value of 0.01. The value of the other two parameters, ε_c for the core concrete and S_y for the bond steel, showed similar trends as the updating history in GM2, where the value of ε_c reached a similar value as it in GM2 but the value of S_y was converged at almost 2 times as the GM2 updated value.

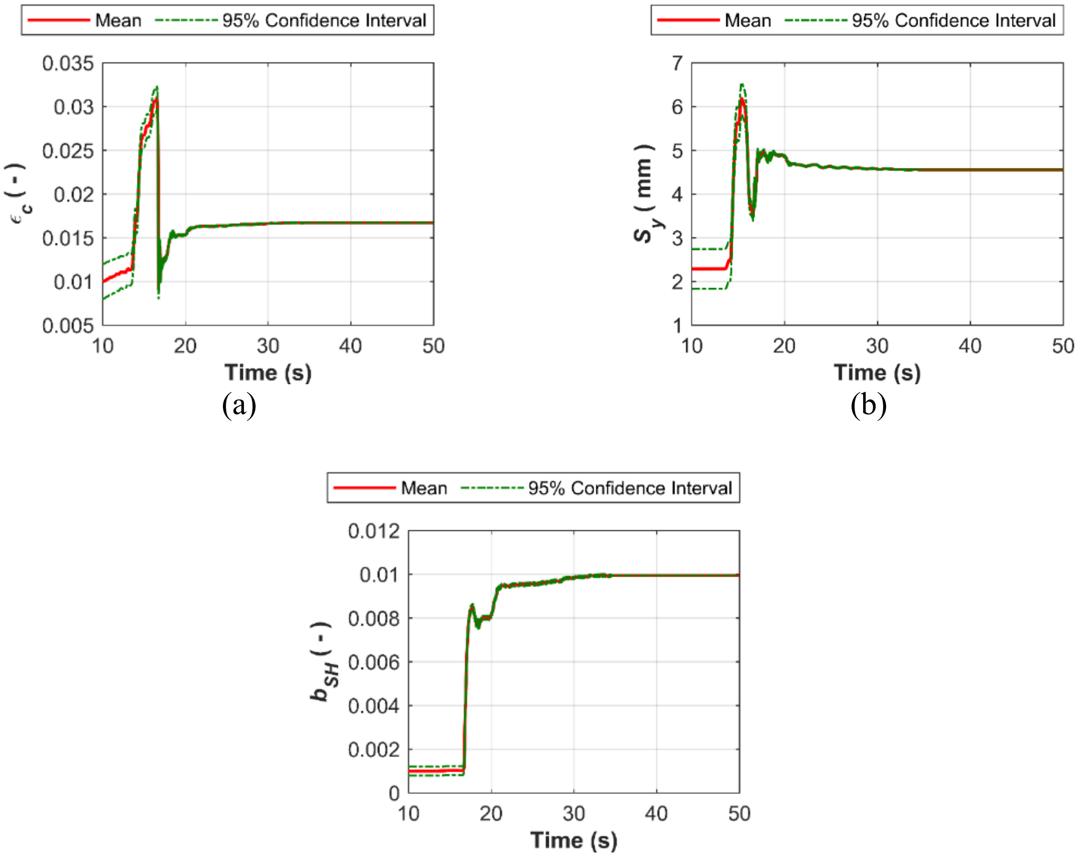

(a) (b)

(c)

Figure 4-16: Model parameter updating histories in GM3 for: (a) core concrete strain at maximum strength (ε_c), (b) bond-slip at yield strength (S_y), and steel post-yield hardening ratio (b_{sh})

4.5.2.4 Nonlinear FE model updating for GM4

Experimental data showed that the seismic response of the bridge column under GM4 was largely different from that under GM2 and the FE model after GM3 FEMU will be further updated using the experimental data from GM4. Note that the ineligible residual (plastic) strains as recorded in the bottom three strain gauges after GM3 was removed before being used for model updating for GM4, to fulfill the non-damage assumption of the model. After a 12000-step FEMU, the FEA prediction and the parameter update history are shown in Figure 4-17 and Figure 4-18, respectively.

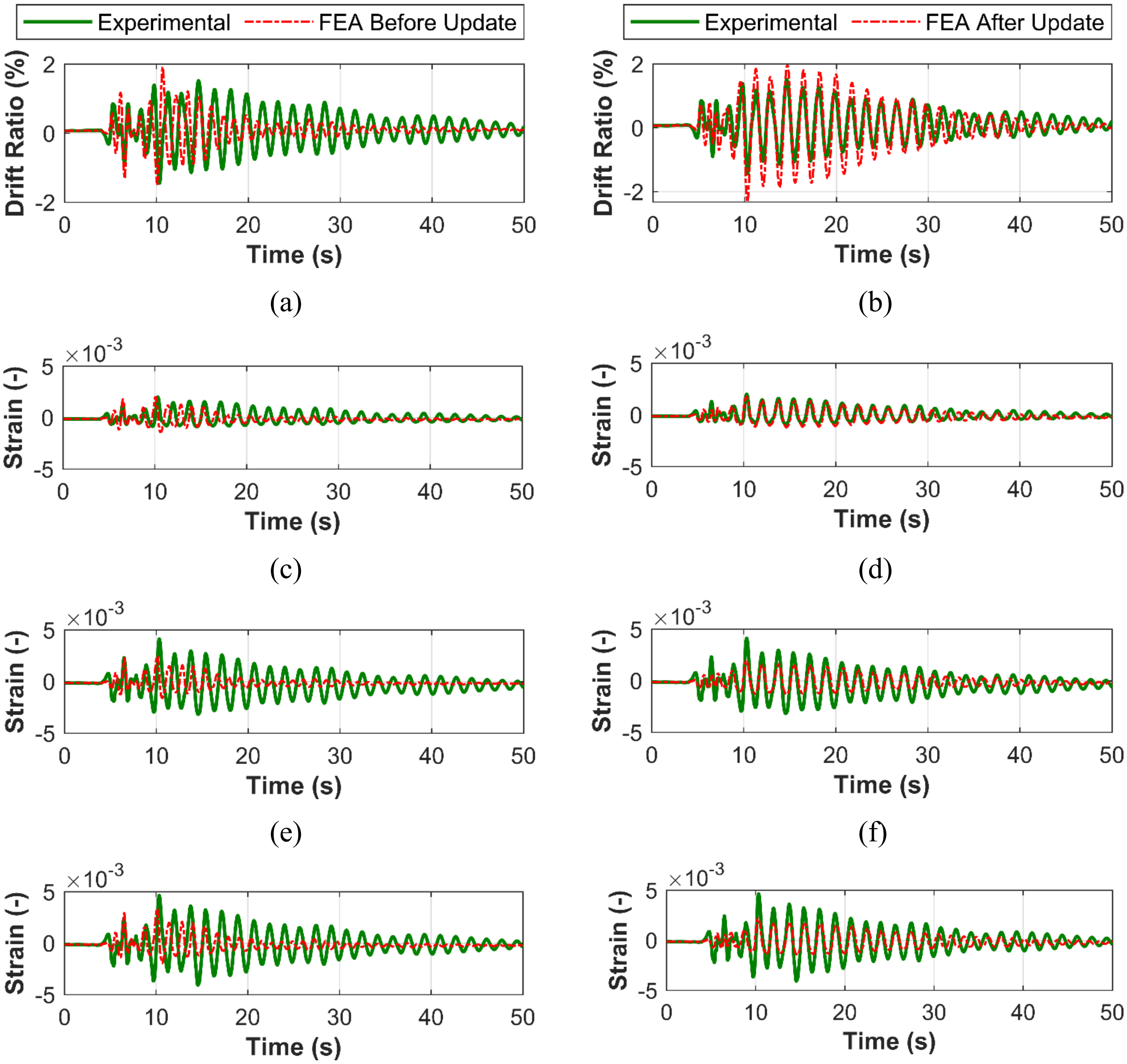

(a) (b)

(c) (d)

(e) (f)

(g) (h)

Figure 4-17: Comparison of the FE-predicted and measured strain histories at three different locations under GM4: 1746 mm above footing (a) before update, (b) after update; 1143 mm above footing (c) before update, (d) after update; 527 mm above footing (e) before update, (f) after update

The accuracy of the FEA prediction still improved during the FEMU for GM4 but the prediction accuracy is degraded comparing to the FEMU results for GM1, GM2, and GM3. Especially, the matching of the two strain gauges (Figure 4-17 f and h) are relatively off. Furthermore, the final estimate of the material parameters led to a more flexible column with larger values for ε_c in the core concrete and S_y for the bond steel (Figure 4-18 a and b).

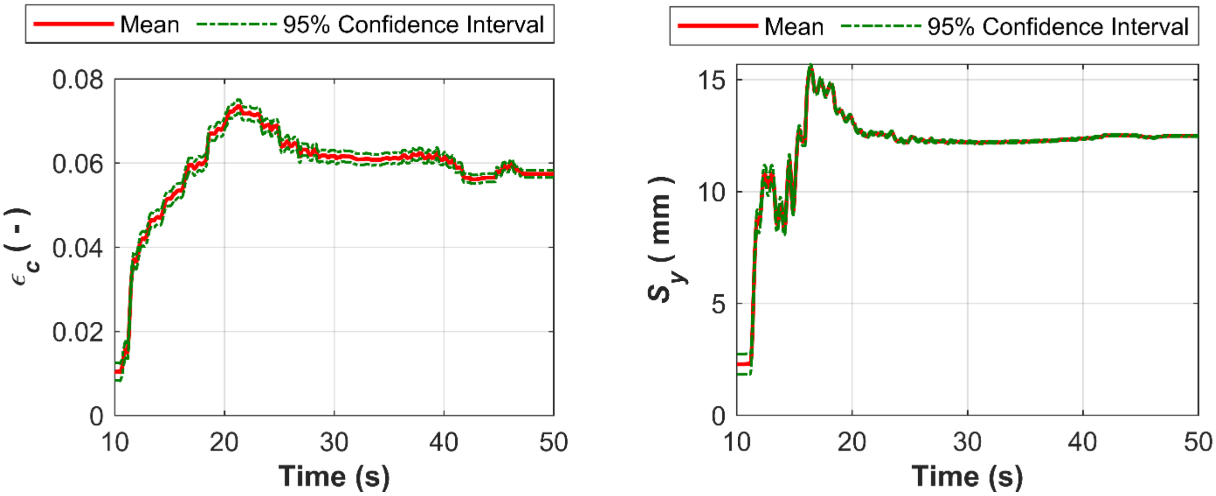

(a) (b)

Figure 4-18: Model parameter updating histories in GM4 for: (a) core concrete strain at maximum strength (ε_c), and (b) bond-slip at yield strength (S_y)

4.6 Discussion of the updated FE models

Four updated FE models are obtained based on the measured seismic data from GM1 ~ GM4. The FE-predictions and measurements for the responses used for updating were compared in previous sections. In this section, the updated models are assessed in terms of (1) damage analysis (e.g., change of damage properties) during the GM used for updating and (2) predictability analysis for unobserved response quantities during the GMs used for updating and drift responses during other GMs, respectively.

4.6.1 Damage analysis

4.6.1.1 Transfer function analysis

Transfer function, which refers to a mathematical function that describes the input (i.e. GM acceleration input) and the output of a system (i.e. acceleration measurement). Such function is capable of reveal the physical properties of a complex structure (i.e. natural frequency of RC column). The signal processing toolbox in *MATLAB* provides an integrated solution, which allows the user to estimate the transfer function between two vectors (i.e. input and measurement).

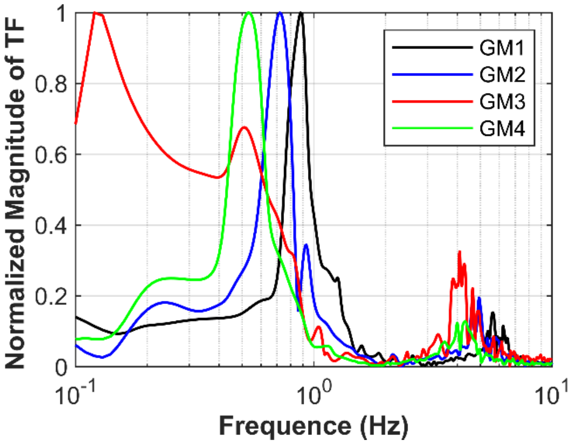

Figure 4-19: Comparison of the magnitudes of the transfer functions of the tested bridge column using seismic data during GM1 ~ GM4

By implementing the transfer function estimate method, the frequency response of GM1 ~ GM4 based on the experimental measurement are plotted together for a better comparison (see Figure 4-19). For GM1, two major peaks can be observed, representing the natural frequency of the first and second mode. By comparing the peaks among GM1 ~ GM3, the frequencies corresponding the first mode decreased over the series of GMs, indicating damage evolution over the three GMs. In addition, due to the decreasing excitation intensity from GM3 to GM4, the first mode frequency did not change much, implying limited additional damage during GM4.

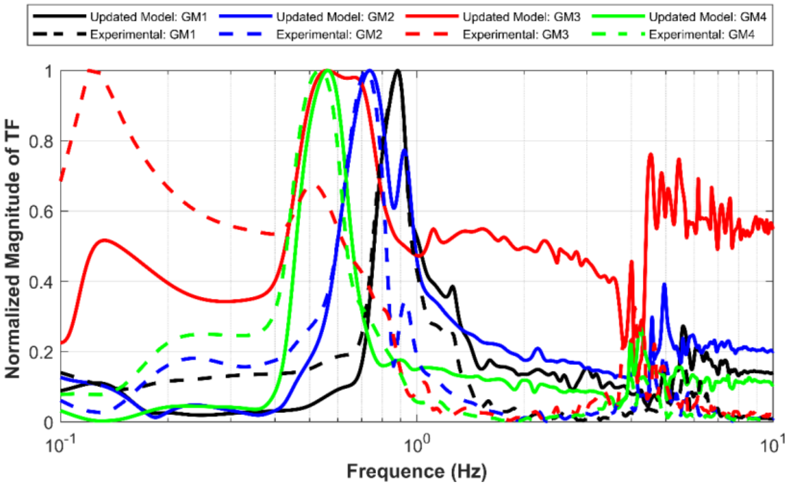

Figure 4-20: Comparisons of the transfer functions between updated model and experimental tests, estimated using the GM accelerations and the superstructure accelerations during GM1 ~ GM4

In order to evaluate the accuracy of the updated FE model, Figure 4-20 shows the comparisons among the transfer functions estimated from the updated models and experimental tests for GM1 ~ GM4. It can be observed that the updated models captured well the natural frequencies and the evolution of the two dominant modes from GM1 ~ GM4. To be noted that the additional mode (at the frequency of 0.14 Hz) during GM3 due to severe damage in the column is also captured, but poorly represented in terms of the magnitude of the transfer functions, which could be due to inappropriate damping model used. As such, it can be concluded that the updated RC column models are capable of representing the damage mitigation during GM1 ~ GM4.

4.6.1.2 Structure stiffness analysis

In addition to the pier drift, the base shear force at the bottom of column is also of interest to engineers. During the test, the base shear force was not measured, and thus estimated approximately as the vibration-induced inertial force. By contrast, the base shear force was recorded directly in the FE models. The comparison between the FE-prediction based on the updated model and the experimental test under GM1 ~ GM4 are presented in Figure 4-21 (a), (b), (c), and (d), in terms of shear-drift ratio hysteresis. It can be observed that despite the residual strain at GM3 and GM4, the base-shear was reproduced well using the updated FE model.

The equivalent stiffness of the RC column can be derived from the base-shear force vs. pier top drift ratio are included in Figure 4-21. It can be revealed that the bridge pier column has an equivalent stiffness at $6.6175 \times 10^7\ N/m$ in GM1, which decreased by 31% in GM2 ($4.5709 \times 10^7\ N/m$). A significant decrease (64%) on the equivalent stiffness can be observed in GM3, which has a value of $1.6427 \times 10^7\ N/m$ and followed by a slightly higher stiffness can be found in GM4 ($E_s = 2.7450 \times 10^7\ N/m$). The change of the magnitude among GM1 ~ GM4 have agreed well with the transfer function analysis, showing the credibility of the updated FE model on representing the damage evolution of the bridge pier column.

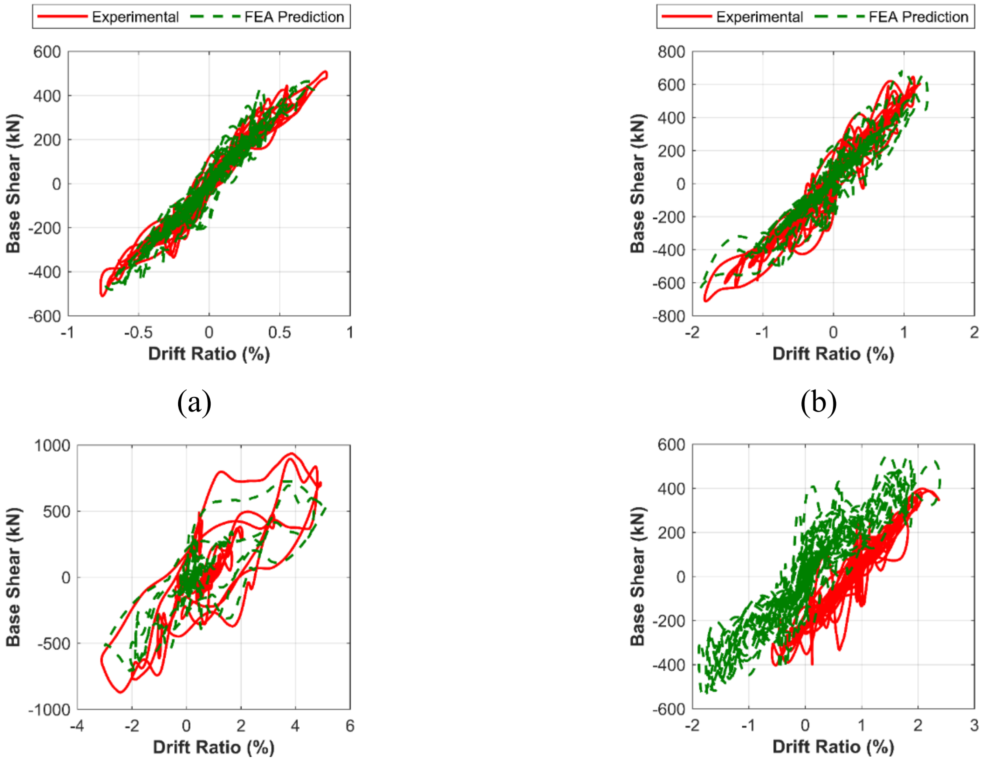

(a) (b)

(c) (d)

Figure 4-21: Comparison of the FEA prediction and experimental observations of hysteresis in terms of base-shear force vs. pier top drift ratio during (a) GM1, (b) GM2, (c) GM3, and (d) GM4

4.6.2 Predictability analysis

The sequential GM tests provided a valuable opportunity to examine the ability of the updated FE models in predicting the structural responses based on historical data. To this end, the four updated FE models are used simulate the seismic response of the RC column subjected to GM1 ~ GM9 separately. The prediction accuracy of the updated FE model for each GM is then quantified using the relative root mean square error (*RRMSE*) between the experimental measurements and the model predictions for the pier drift histories. In addition, the prediction accuracy for non-updated (initial) FE model with and without bond-slip considered are also quantified for comparison.

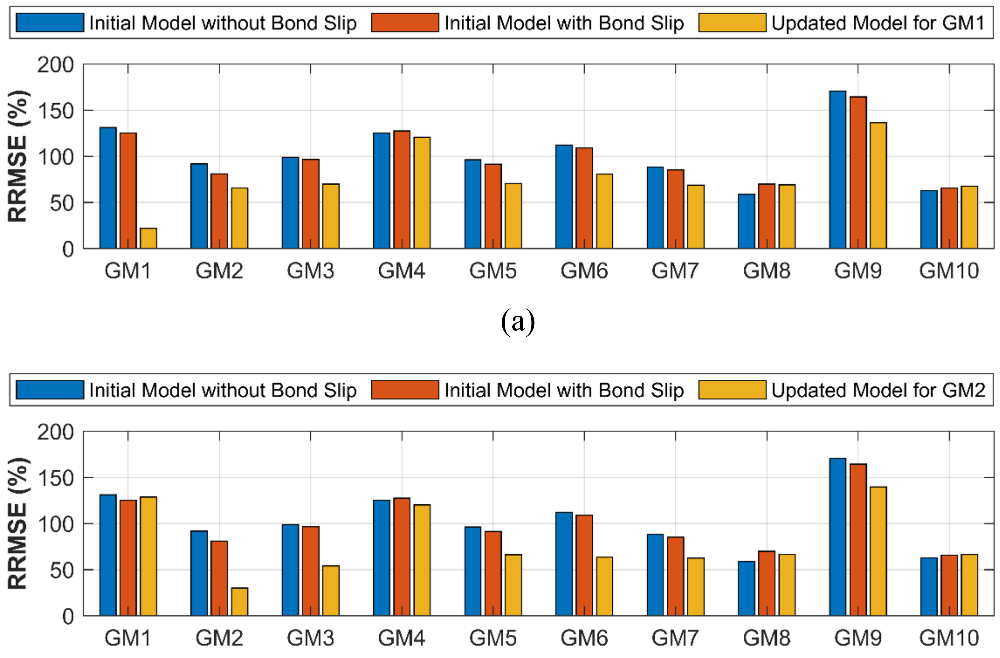

(a)

(b)

Figure 4-22: Comparison of the FE models in predicting seismic response of the RC column during GM1 ~ GM10 before and after updating using seismic data from (a) GM1 and (b) GM2

The prediction accuracy of each FE model under separate runs are summarized in Figure 4-23 and Figure 4-23. Based on the cross-comparison of the modeling accuracy among the three FE models (i.e., initial model without bond-slip, initial model with bond-slip, and updated model), the FEMU can greatly increase the prediction accuracy within the same GM that was used for the model updating. In addition, an increase on the model prediction accuracy can be observed in the next two or three GMs following the GM used for model updating. Furthermore, it can be noticed that the updated model based on measurements from GM1 ~ GM3 does not have significant impact on the model prediction accuracy for GM7 ~ GM10, while the updated model from GM4 could achieve a better prediction for those GMs.

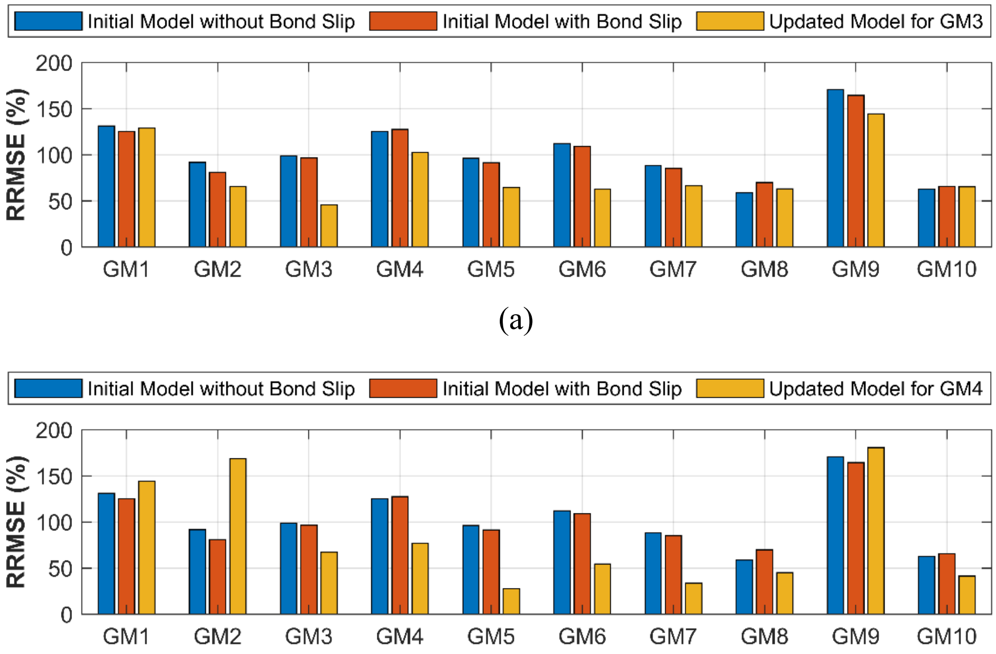

(a)

(b)

Figure 4-23: Comparison of the FE models in predicting seismic response of the RC column during GM1 ~ GM10 before and after updating using seismic data from (a) GM3, (b) GM4

4.7 Summary

In this chapter, the UKF-based FEMU was utilized to identify the key modeling aspects of a full-scale RC bridge column considering bond-slip using shake-table test data. A fiber-based FE model was initially developed for this column based on material coupon tests and empirical judgement. The important material parameters of the developed FE model were identified via a one-at-a-time sensitivity analysis. The optimal values of key modeling parameters were estimated using the FEMU framework introduced in Chapter 3. FE predictions of the models with updated parameters for the bridge column correlated well with the experimental measurements. In addition, the credibility of the updated FE models was further verified by (1) the damage evolution indicated by the frequency change obtained from transfer function analyses and (2) the capability of the updated FE models in predicting the structural responses of the column during other GMs.

CHAPTER 5: NONLINEAR FE MODEL UPDATING FOR BRIDGE COLUMN WITH BOND-SLIP AND REBAR BUCKLING

5.1 Introduction

The study in the previous chapter reveals that structural softening can be caused by bond-slip when the RC column is subjected to GMs of moderate intensity levels. However, as intensity of GMs increases, further softening can be caused as a result of steel rebar buckling. Thus, structural softening effect could not be captured solely by considering bond-slip, and the effect of buckling of steel should be included in the FE modeling of RC bridge columns. According to the test report for the bridge column studied in this thesis [52], longitudinal steel rebar buckling was clearly observed during GM7 and more rebars buckled in in following GMs. Such evidence leads to a conclusion that the rebar buckling is important for FE modeling of RC bridge columns subjected to high-intensity GMs, as pointed out in many existing studies (e.g., [75]–[78]). Various steel material models with asymmetrical stress-strain behavior to account for the buckling effect have been successfully developed and implemented in the FE software framework (i.e., *OpenSees*).

However, the accuracy and robustness of the existing buckling steel material models remains unclear, since they were developed under specific conditions (e.g., with a particular range of slenderness ratios for steel rebars). As such, the performance of four well-known buckling steel material models is evaluated for a wide range of slenderness ratios using experimental data collected from the literature. Two different approaches are used for the material model calibration, including the UKF-based Bayesian optimization and the Simulated Annealing (SA). This will provide a basis for selecting the best or the most versatile buckling steel material model to be used in the RC column modeling.

In the FE model for the RC column developed earlier, *Steel02*, which was used to represent the uniaxial stress-strain behavior of steel rebars without considering buckling effects, is replaced by the buckling steel material model selected. In this chapter, nonlinear FEMU is performed for the RC column considering steel rebar buckling in addition to bond-slip. Note that simulated data with additive Gaussian white noise (AGWN) for GM5 ~ GM9 is used instead of experimental data recorded during the test, to verify the predictability of the UKF-based nonlinear FEMU strategy for buckling effect. The experimental data is not used here for GM5 ~ GM9 because the model uncertainty, mainly due to the damaging effect of pre-applied GMs (GM1 ~ GM4) during the test, is not included.

5.2 Performance assessment of buckling steel material models

To simulate the buckling effect of steel rebars in RC columns, the material model for steel should be capable of representing the asymmetry behavior in the stress-strain relationship. Several material models, such as *Steel4*, *Reinforcing Steel-GA*, and *Reinforcing Steel-DM* available in the *OpenSees* and *C.B. Steel* recently implemented according to Kashani et al. [25], are assessed using experimental data. The stress-strain behavior simulated from the calibrated model is compared with the experimental results. Furthermore, the importance of the model parameters is studied, which can be potentially used to assist selecting crucial updating parameters in the nonlinear FEMU of RC bridge columns when considering steel rebar buckling.

5.2.1 Optimization methods for material calibration

To assess the accuracy and robustness of the existing buckling steel material models, the UKF-based Bayesian optimization, which was used for nonlinear FEMU in the previous chapter, is used for material calibration. Its capability is further verified by the global optimization technique (i.e., SA). These two optimization methods are first illustrated as follows before being used for model calibration using experimental data.

5.2.1.1 UKF-based Bayesian optimization

To verify the ability of UKF-based Bayesian optimization for material model calibration, i.e., identifying the unknown model parameters, simulated data from a material model (i.e., *Steel02*) is used. The true parameter setting of the *Steel02* material, which is used to simulate the stress-strain data for the grade 60 steel, is shown in Table 5-1.

Table 5-1: Initial and true material parameters values for *Steel02* material model

	f_y	E_s	b_{sh}	R_0	cR_1	cR_2
True	520 MPa	196 GPa	0.01	20	0.925	0.15
Initial	413 MPa	165 GPa	0.001	20	0.925	0.15

In addition to the three steel material properties: f_y for the yield strength, E_s for the elastic modulus, b_{sh} for the post-yield strain hardening ratio, the other three material model parameters such as R_0, cR_1 and cR_2, are used to control the elastic-plastic transition in the stress-strain relationship [23].

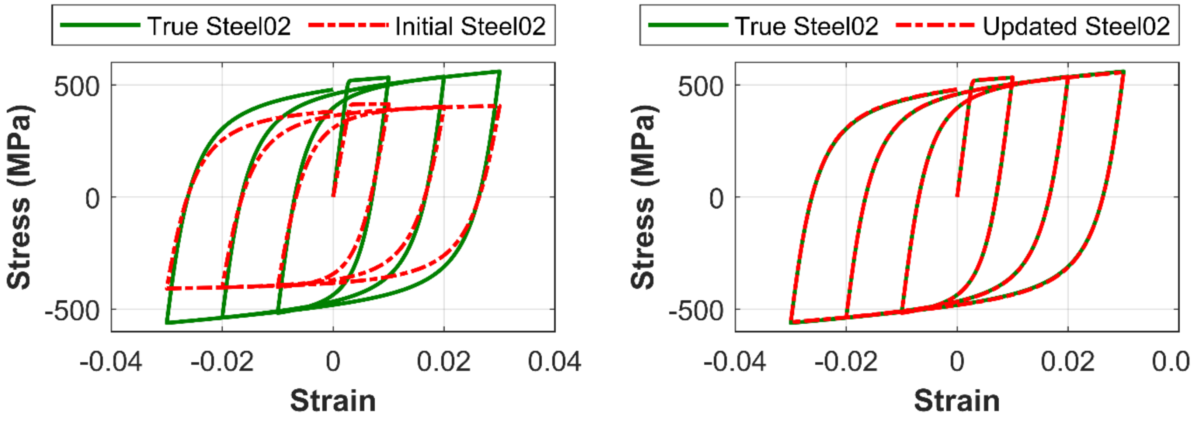

(a) (b)

Figure 5-1: Cyclic behaviors of *Steel02* material model compared with the true stress-strain curve simulated from *Steel02*: (a), before calibration, and (b) after calibration

For the purpose of material calibration, the same material model (*Steel02*) is used first assuming the model is accurate while the parameters are unknown. Without loss of generality, among the six model parameters, f_y, E_s and b_{sh} are chosen to be optimized from the initial guess as presented in Table 5-1. The starting points are chosen intentionally different from the true values and the corresponding stress-strain curve is shown as the dashed line in Figure 5-1(a). The three unknown model parameters considered here are estimated by UKF-based Bayesian optimization ($\boldsymbol{P}$ defined with the coefficient of variation = 0.1 for each parameter and correlation coefficients = 0.01 , $\boldsymbol{R}$ =

10^{-8}, and $\boldsymbol{Q}$ = 10^{-16}), and the calibrated stress-stain curve is shown in Figure 5-1 (b) with comparison to the true stress-strain curve. It shows that the UKF-based Bayesian optimization can successfully calibrate the material model well, when the same material model is used (i.e., with the absence of model uncertainty).

Table 5-2: Material model parameters for *SteelDRC* material used for the cyclic stress-strain measurement.

f_y	E_s	b_{ini}	f_u	b_{ult}
520 MPa	196 GPa	0.01	745 MPa	0.013

To further verify the capability of UKF-based Bayesian optimization for material calibration, an additional case considering model uncertainty is used here. Unlike the previous case, a different material model (*SteelDRC*) is utilized to simulate the true stress-strain curve. Compared to *Steel02*, *SteelDRC* is more capable of representing the stress-strain relationship obtained from the material coupon tests (see Figure 5-2). This is because it uses a higher order formulation for the strain-hardening branch and is capable of modeling the yield plateau as well. The true parameter setting of *SteelDRC* is shown in Table 5-2, in addition to other model parameters as defaulted.

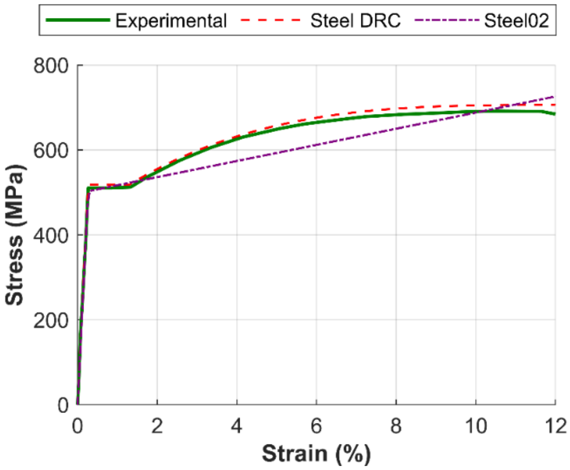

Figure 5-2: Tensile behaviors of *SteelDRC* and *Steel02* compared to experimental coupon test provided by Schotter et al. [52]

To calibrate the aforementioned *Steel02* material model for the stress-strain curve data, which were simulated using the *SteelDRC* material model, additional four modeling parameters (a_1, a_2, a_3, a_4) is further included to account for the isotropic hardening effect. Among these four parameters, two of them (a_1, a_3) are updated in this case [23].

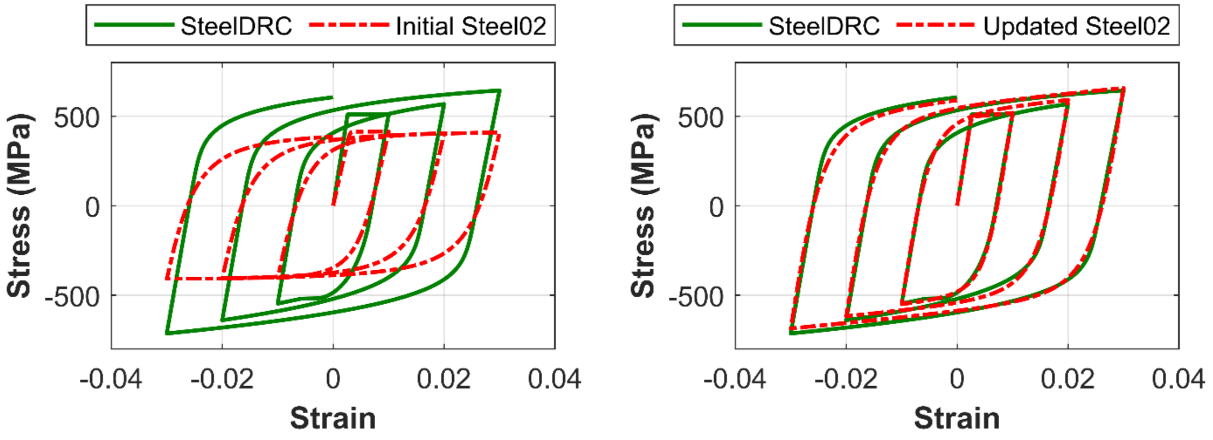

(a) (b)

Figure 5-3: Cyclic behaviors of *Steel02* material model compared with the true stress-strain curve simulated from *SteelDRC* material model: (a) before calibration and (b) after calibration

The true stress-strain curve simulated from *SteelDRC* is plotted with the model prediction before and after calibration, as shown in Figure 5-3 (a) and Figure 5-3 (b), respectively. As can be observed, even with the presence of the modeling uncertainty (inaccuracy) such as the difference in the material formulation, the UKF-based Bayesian optimization can successfully calibrate the material model.

5.2.1.2 Simulated annealing

The simulated annealing (SA) is a technique for approximating the global optimum of an objective function, and this algorithm was developed based on a thermodynamic phenomenon, i.e., physical annealing, SA is useful in finding global optima in the presence of many local minima [79]. SA is then used for material model calibration, where the cyclic stress-strain curve simulated using *SteelDRC* material model is utilized and the *Steel02* material model with isotropic hardening parameters is calibrated. The SA algorithm in this case is designed to seek the optimal parameter values within a given range as shown in

Table 5-3 that could achieve minimal discrepancy when compared with the true data. Here the discrepancy is quantified by the relative root-mean square error (*RRMSE*) between the stress-strain response of *Steel02* material and the *SteelDRC* material.

Table 5-3: Definition of the starting point, lower bound, and upper bound in SA for *Steel02* parameters

	f_y	E_s	b_{sh}	a_1	a_3
Initial value	520 MPa	195 GPa	0.01	0.5	0.5
Lower bound	413 MPa	165 GPa	0.00	0.0	0.0
Upper bound	621 MPa	221 GPa	0.02	1.0	1.0

Table 5-4: Summary of the calibration results for *C.B Steel material* using UKF and simulated annealing

	f_y	E_s	b_{sh}	a_1	a_3	*RRMSE*
UKF	463.53 MPa	172 GPa	0.018	0.053	0.049	0.023
Simulated Annealing	591.29 MPa	172 GPa	0.0098	0.004	0.007	0.038

The comparison of the estimation results between the UKF and SA is summarized in Table 5-4. As revealed from the low values in the *RRMSE*, both UKF and SA have achieved a good correlation with the true response. However, the difference in the material parameters between the calibrated models using the two methods indicates the presence of multiple local minimums. Thus, the overall cyclic behavior is then compared to evaluate the calibration performance. As shown in Figure 5-4, the comparison of the stress-strain curves reveals that the UKF have a more accurate estimation on the yield stress and the isotropic hardening rate. This shows the UKF can achieve equivalent or higher accuracy in the parameter estimation compared to the SA when a finite number of iterations or function evaluations is used (e.g., 1000 iteration steps).

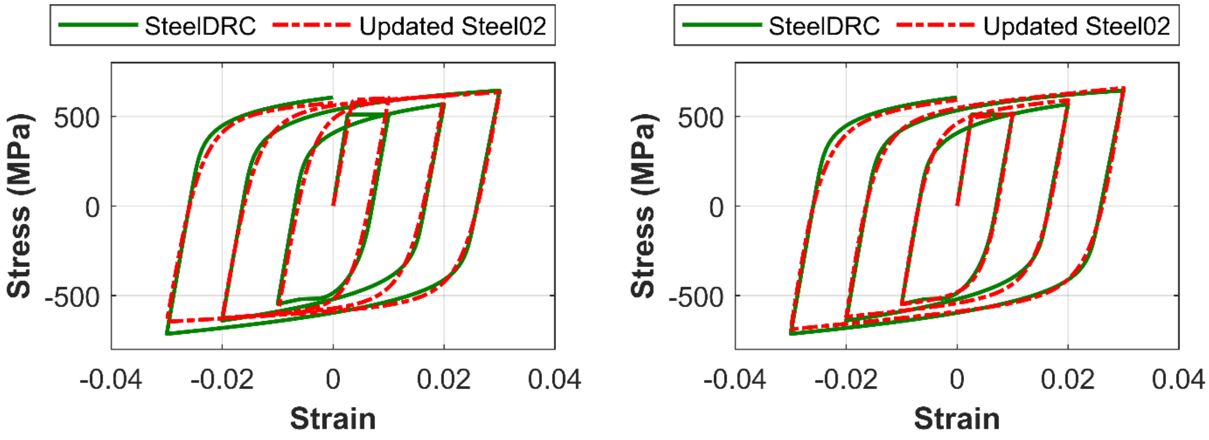

(a) (b)

Figure 5-4: Comparison of *Steel02* material calibration results with different optimization approaches: (a) simulated annealing, and (b) unscented Kalman filter

5.2.2 Material model performance evaluation

5.2.2.1 Experimental measurements

The four buckling steel material models (i.e., *Steel4*, *Reinforcing Steel-GA*, *Reinforcing Steel-DM*, and *C.B. Steel*) are calibrated to five steel rebar coupon tests with buckling. They consist of two sets of experiments, covering a wide range of length-to-diameter ratios (*L/D*). Detailed information for each specimen analyzed in this study is shown in Table 5-5, including the rebar dimensions and the material properties.

Table 5-5: Dimensions and material properties of steel specimen tested by Monti and Nuti [24] and Kashani et al. [80]

Specimen	L/D	$f_{y/Nominal}$	$f_{y/True}$	E_0
#1	5	430 MPa	440 MPa	180 GPa
#2	8	430 MPa	440 MPa	180 GPa
#3	11	430 MPa	440 MPa	180 GPa
#4	10	500 MPa	520 MPa	194 GPa
#5	15	500 MPa	520 MPa	194 GPa

The first set experimental stress-strain data is obtained from the tests conducted by Monti and Nuti [24] [75] [76]. The rebar specimens were made of Italy-made type FeB44 steel, with the yield strength of 440 MPa. This test set consisted of three specimens with an *L/D* ratio at 5, 8, and 11, which are denoted as specimen #1 ~ #3, respectively. Each of the specimen was loaded to have three full cycles with a peak strain at 0.01, 0.02, and 0.03. To be noted that as shown in Figure 5-5, the last cycle for all three cases provided by Monti and Nuti [24] are incomplete.

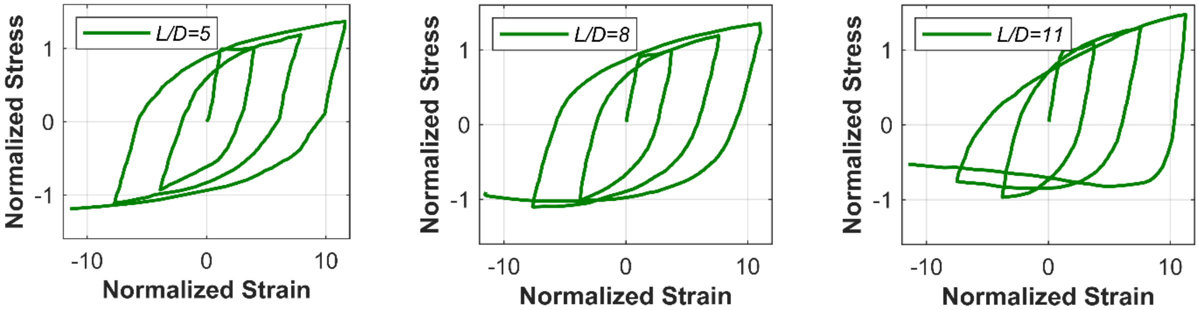

(a) (b) (c)

Figure 5-5: Cyclic stress-strain relationship of steel with different buckling levels associated with different *L/D* ratios [24]: (a) *L/D*=5 , (b) *L/D*=8, and (c) *L/D*=11

The second set of experimental stress-strain data is obtained from the test conducted by Kashani et al. in 2015 [80], where experimental stress-strain relationship of two specimens (namely specimen #4 and #5) were recorded. According to the literature, a cyclic push-over test was performed at each of the specimens, consisted of 4 strain levels and each cycle repeated twice, where only the first cycle is analyzed in this study for simplification purposes (see Figure 5-6).

All test specimens included in such experimental analysis have a 12 mm diameter and casted with British type B500 steel. The in-site coupon test had recorded an actual yield strength of 520 MPa and an actual elastic modulus at 196 GPa. To represent longitudinal steel rebar with severe buckling effect, specimen #4 and #5 were designed with an *L/D* ratio at 10 and 15, respectively.

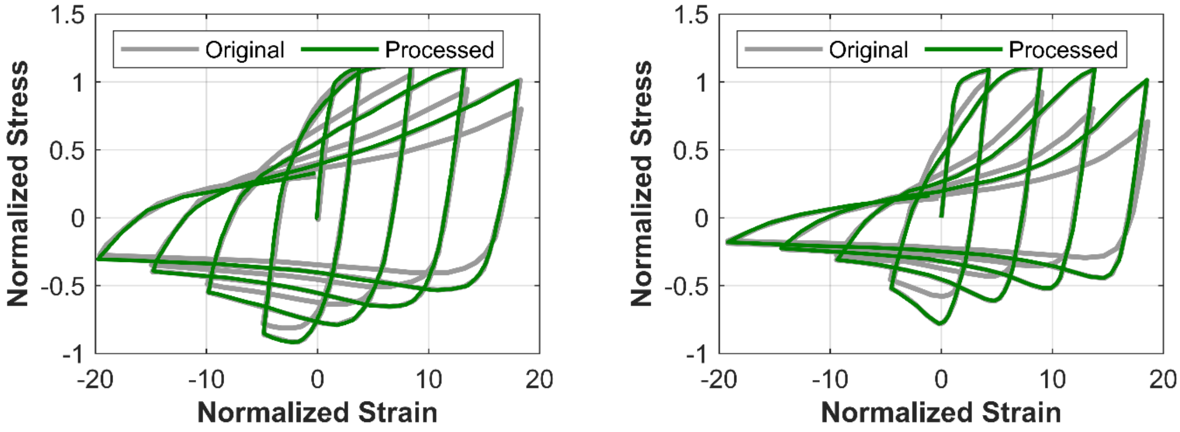

(a) (b)

Figure 5-6: Original and processed cyclic stress-strain relationship of steel with different buckling levels associated with different *L/D* ratios [80]: (a) *L/D*=10, and (b) *L/D*=15

By cross-comparing the stress-strain relationship among the five specimens, it can be noticed that the cyclic stress-strain behaviors of specimen #3 and #4 are significantly different, while a close *L/D* ratio was assigned for specimen #3 (*L/D* =11) and #4 (*L/D* =10). With a closer examination at the monotonic backbone curve of the two specimens (see Figure 5-7), it can be observed that specimen #3 has more hardening compared to specimen #4 , which is potentially the reason behind certain difference between the specimen behavior.

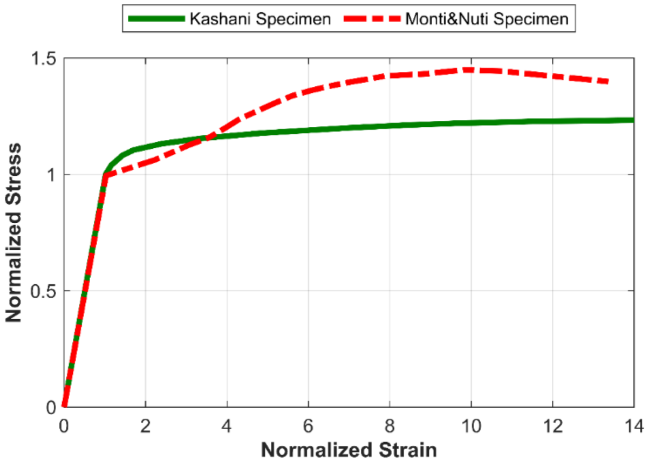

Figure 5-7: Normalized tensile stress-strain relationship of steel material for specimen #1 ~ #3 [24] and specimen #4 ~ #5 [80]

5.2.2.2 *Buckling steel material model calibration for Steel4*

The *Steel4* material model in *OpenSees* is highly versatile and it allows the customization of complex uniaxial material behavior (i.e. with different kinematic and isotropic hardening in tension and compression), including asymmetrical behaviour. The material model parameters can be categorized into four groups: the elastic parameters, the isotropic hardening parameters, the kinematic hardening parameters, and the ultimate strength parameters. Two parameters control the elastic branch, including the yield strength f_y and the Young's modulus E_0. As shown in Figure 5-8 (a), the kinematic hardening model of *Steel4* adopt the Menegotto-Pinto model and is controlled by four parameters, including the hardening ratio b_k and the nonlinear hardening transition parameters (R_0, r_1, and r_2). The isotropic hardening of the *Steel4* material is controlled by another five parameters, including the initial hardening ratio b_i, the saturated hardening ratio b_l, the saturation hardening transition factor ρ_i, the exponential transition factor R_i, and the yield plateau length factor l_{yp} as shown in Figure 5-8 (b). The ultimate parameters include two parameters: the ultimate strength f_u and the transition factor R_u as shown in Figure 5-8 (c).

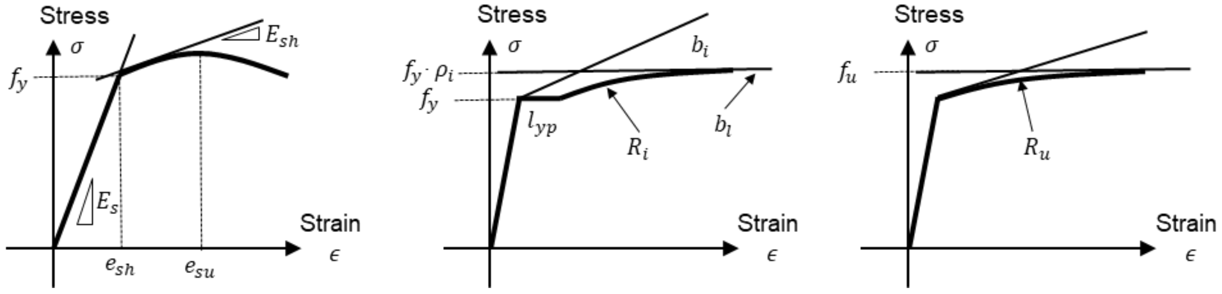

(a) (b) (c)

Figure 5-8: Parameter definition for *Steel4* material: (a) kinematic hardening, (b) isotropic hardening, and (c) ultimate limit

To take the buckling effect into consideration, the asymmetry behavior of *Steel4* needs to be customizable for four more kinematic hardening parameters, four more isotropic hardening parameters (except the yield plateau length factor l_{yp}), and two more ultimate limit parameters. To distinguish the compression-related parameters from the tension-related parameters, a subscript 'c' is added in the notation. (e.g., ρ_{ic} is corresponding to the saturation hardening transition factor for the compression branch). To sum up, it requires a total of 23 material model parameters to define the *Steel4* material with buckling effect considered.

Among all these material model parameters, sensitivity analysis is conducted for obtaining a better understanding of the role of each parameter and further guide the parameter selection for material calibration. To this end, one-at-a-time perturbation analysis is performed by varying the parameter by $\pm 10\%\ \theta_0$ and $\pm 20\%\ \theta_0$ around the center value (θ_0). The center value of the material model is listed in Table 5-6 below, where the tensile and compressive value are partially adopted from work proposed by Mohammed et al. [83]. In addition, the yield plateau is neglected in this study by assuming l_{yp} = 0. The stress-strain backbone curves in both compression and tension are compared. Note that the stress-strain relationships are plotted with dimensionless parameters: the stress and the strain are normalized by the yield stress and the yield strain, respectively.

Table 5-6: Summary of the center value θ_0 used for the perturbation analysis of *Steel4* material

Tensile material parameters										
b_k	R_0	r_1	r_2	b_i	ρ_i	b_l	R_i	l_{yp}	f_u	R_u
0.01	20	0.9	0.15	0.02	3	0.0004	3	0	744 MPa	5
Compressive material parameters										
b_{kc}	R_{0c}	r_{1c}	r_{2c}	b_{ic}	ρ_{ic}	b_{lc}	R_{ic}	-	f_{uc}	R_{uc}
0.01	20	0.9	0.15	-0.048	-5.6	0.02	2		744 MPa	5
Basic material parameters										
f_y	E_0									
520 MPa	196 GPa									

Figure 5-9 presents the perturbation analysis results for the five most sensitive material parameters in terms of the tensile behavior; parameters with low sensitivity are not reported. As can be observed, the two basic parameters, such as f_y and E_0 (see Figure 5-9 a and b) have a high sensitivity, where the f_y mostly affects the yield behavior and E_0 affects the general behavior in the tensile branch. The post-yield behavior is governed by the kinematic hardening ratio (b_k) and isotropic hardening ratio (b_i), where both have shown a similar level of sensitivity. The ultimate strength (f_u) represents an upper limit on the material strength and is only sensitive when the stress of the material is extremely high.

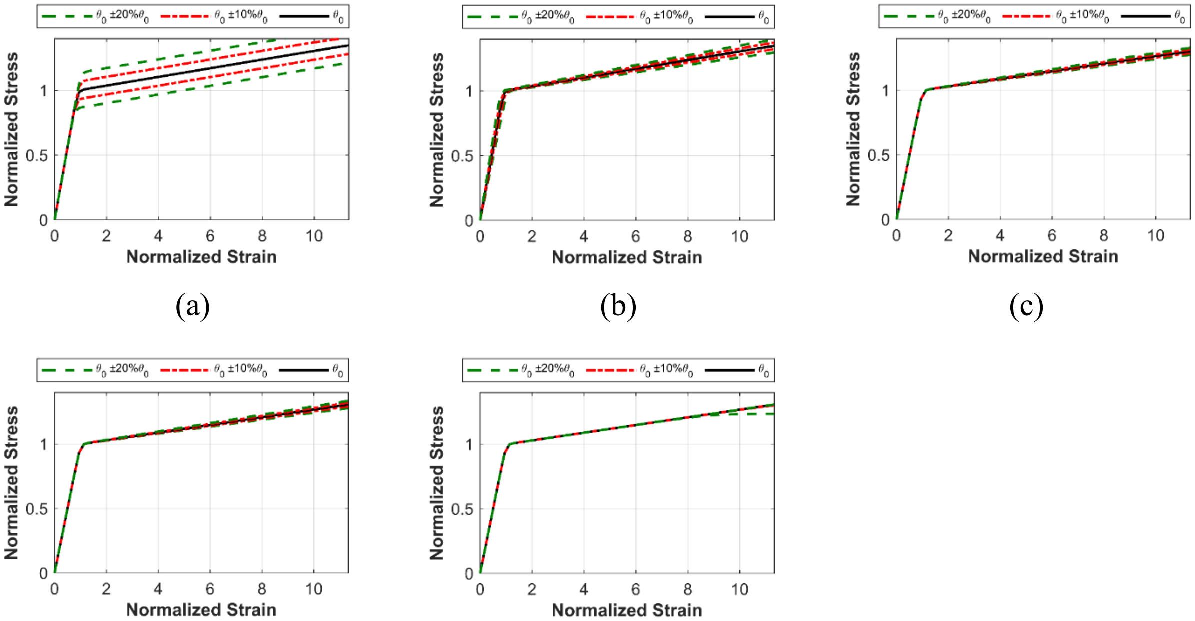

(a) (b) (c)

(d) (e)

Figure 5-9: Perturbation analysis for the tension branch of *Steel4* with parameter: (a) $\theta = f_y$, (b) $\theta = E_0$, (c) $\theta = b_k$, (d) $\theta = b_i$, and (e) $\theta = f_u$

The perturbation analysis results of the six most sensitive material parameters for the compressive branch are shown in Figure 5-10. As can be found in Figure 5-10 (a) and (b), the two basic parameters (f_y and E_0) also have a relatively high sensitivity in the compressive behavior, where the f_y controls the yield stress and E_0 controls the initial slope and the post-yield slope when hardening parameters are fixed. The kinematic hardening parameter b_{kc} also show a certain degree of the sensitivity on the post-yield branch of the compressive envelope. Furthermore, three isotropic hardening parameters (b_{ic}, ρ_{ic}, and R_{ic}) contributes to the post-yield behavior of the steel in the compression branch with different levels.

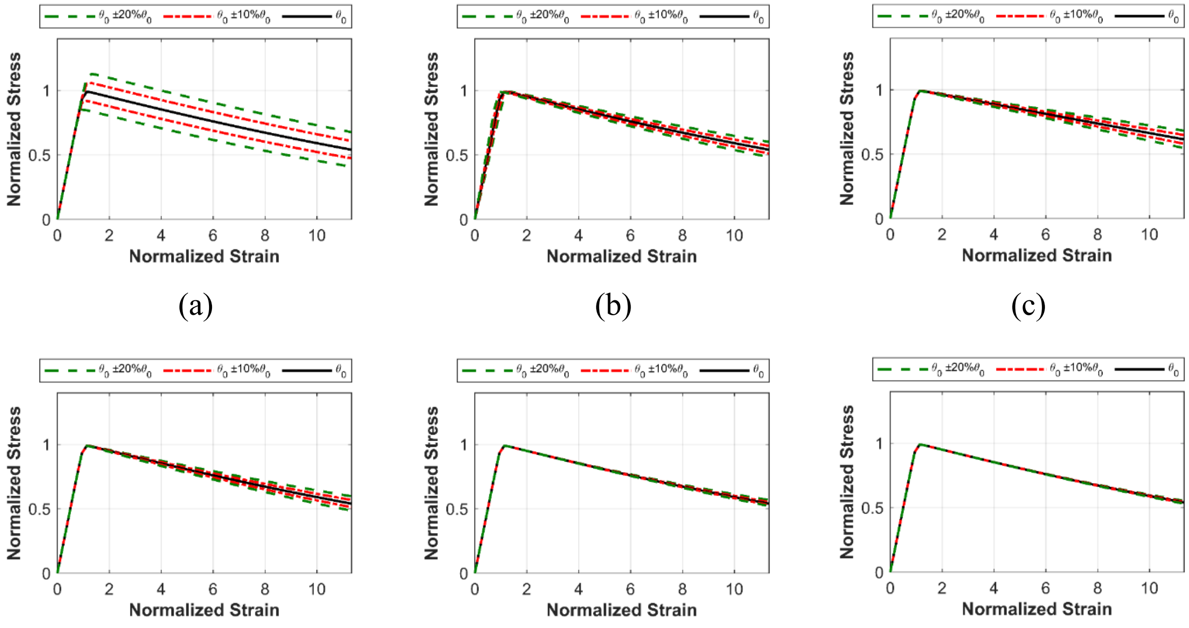

(a) (b) (c)

(d) (e) (f)

Figure 5-10: Perturbation analysis for the compression branch of *Steel4* with parameter: (a) $\theta = f_y$, (b) $\theta = E_0$, (c) $\theta = b_{kc}$, (d) $\theta = b_{ic}$, (e) $\theta = \rho_{ic}$, and (f) $\theta = R_{ic}$

Based on the monotonic behavior of the material model *Steel4*, it can be concluded that the most important 9 material parameters are: f_y, E_0, b_k, b_{kc}, b_i , f_u , b_{ic}, ρ_{ic}, and R_{ic}. The perturbation analysis results for the cyclic behavior for all these 9 material parameters identified is presented in Figure 5-11. As can be observed, the two basic parameters still have the highest sensitivity among all modeling parameters. Secondly, the kinematic hardening parameters b_k and b_{kc} , as well as the isotropic parameters such as b_i, b_{ic}, ρ_{ic}, and R_{ic} have shown a moderate sensitivity on the cyclic behavior. Lastly, the parameter f_u in *Steel4* does not have a significant impact on the cyclic behavior within a reasonable range of strain levels considered in this study.

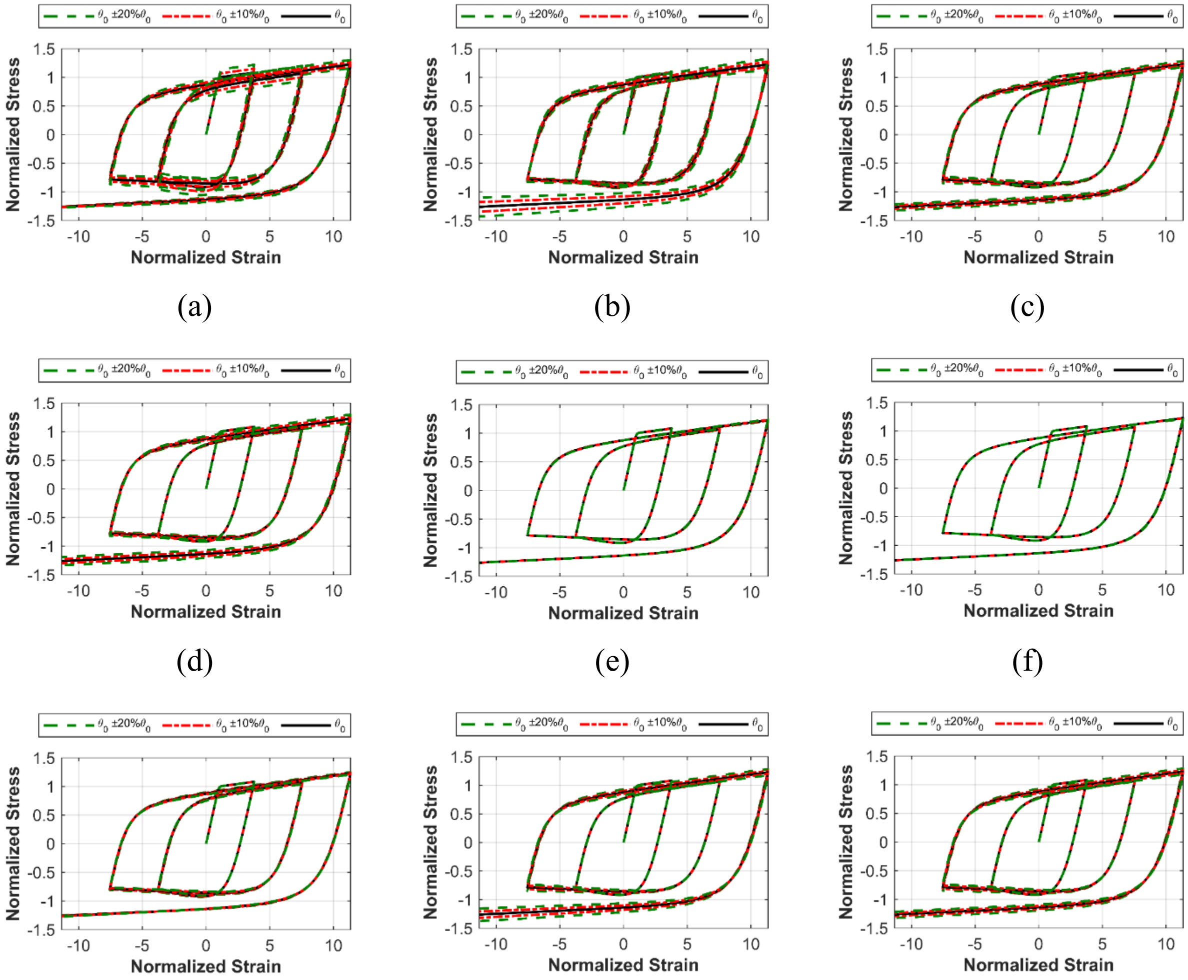

(a) (b) (c)

(d) (e) (f)

(g) (h) (i)

Figure 5-11: Perturbation analysis for the cyclic stress-strain of *Steel4* with parameter: (a) $\theta = f_y$, (b) $\theta = E_0$, (c) $\theta = b_k$, (d) $\theta = b_{kc}$, (e) $\theta = b_i$, (f) $\theta = f_u$, (g) $\theta = b_{ic}$, (h) $\theta = \rho_{ic}$, and (i) $\theta = R_{ic}$

The results from perturbation analysis for the static and cyclic behavior have provided valuable information on the parameter selection. Firstly, the two basic parameters (f_y and E_0) are key for defining the material model. Secondly, the tensile behavior of the *Steel4* material is influenced by the kinematic hardening parameter (b_k) and isotropic hardening parameter (b_i), while the compressive behavior is governed by kinematic hardening parameter (b_{kc}) and isotropic hardening parameters (b_{ic}, ρ_{ic}, and R_{ic}). Lastly, the perturbation analysis for the cyclic behavior has affirmed the significance of the two basic parameters (f_y and E_0), the kinematic hardening parameters

(b_k, b_{kc}), and isotropic hardening parameters (b_{ic}, ρ_{ic} and R_{ic}). As such, these seven material model parameters should be considered for material calibration.

However, since the elastic modulus (E_0) for steel is well known and can be determined readily based on the initial slope of the stress-strain curve, it is excluded from the material calibration process. The yield strength (f_y) , the three isotropic hardening parameters (b_{ic}, ρ_{ic} and R_{ic}) and two kinematic hardening parameters (b_k and b_{kc}) are included considering their importance on both monotonic and cyclic behavior. As such, the UKF-based Bayesian optimization is then used for material calibration with the aforementioned six parameters. Furthermore, SA with a large number (e.g., 1000) of iterations is used for material calibration for the purpose of cross-verification.

The detailed calibration results for specimen #1 with UKF-based Bayesian optimization and SA are compared in Table 5-7, where the performance of the updated material model is evaluated by the relative root mean square error (*RRMSE*) between the simulated stress response and the experimental stress response corresponding to the strain history in the test protocol.

Table 5-7: Summary of the calibration results for *Steel4* using UKF and SA for specimen #1 with *L/D* = 5

	f_y	b_{ic}	ρ_{ic}	R_{ic}	b_k	b_{kc}	*RRMSE*
SA	342 MPa	-0.017	-5.86	1.58	0.036	0.047	0.182
UKF	335 MPa	-0.017	-6.65	2.43	0.041	0.052	0.194
UKF	(440 MPa)	-0.019	-6.33	2.36	(0.04)	(0.04)	0.238

Note: values in () are fixed as predetermined.

The calibrated parameter values from UKF-based Bayesian optimization and SA agree well with each other. This shows that both methods successfully identified the optimum parameter values to minimize the discrepancy between the material model simulation and experimental measurement. A closer examination at the updated cyclic behavior reveals under-estimation of the yield strength (see Figure 5-12), which is caused by neglecting the yield plateau in the first cycle of the experimental test.

In addition to the case where all sensitive parameters are included, one more calibration case is studied to further limit the number of calibration parameters, for example, by eliminating the less important parameters. Note that in this case, the yield strength f_y is well-defined and thus fixed to 440 MPa corresponding to the yield plateau in the experimental stress-strain hysteresis. The kinematic hardening parameters are also excluded as they are less important compared to the isotropic hardening parameters according to the perturbation analyses. Compared to the preceding case, the *RRMSE* for this case is slightly higher, indicating it can possibly reduce the computational cost while leading to less accurate results (see Figure 5-12).

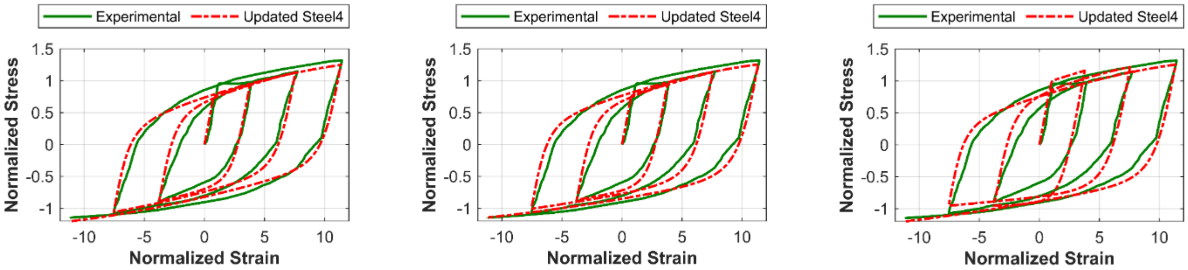

(a) (b) (c)

Figure 5-12: Stress-strain hysteresis comparison between the experiment and the calibrated *Steel4* material model using (a) SA with six parameters, (b) UKF with six parameters, and (c) UKF with three parameters for specimen #1

The calibration results from UKF-based Bayesian optimization and SA for specimen #2 are compared in Table 5-8. These two methods calibrated the material model considering 6 parameters with almost equivalent accuracy. The comparison of the stress-strain hysteresis between the experiment and the calibrated *Steel4* material model for specimen #2 is shown as Figure 5-13. As can be observed, both calibrated models achieved relatively good match with the experimental data, except some minor differences. When considering only three parameters in the material model calibration, the modeling accuracy is still considered to be acceptable with only slight increase in *RRMSE*. This implies that the parameter reduction with a loss of modeling flexibility is considered as reasonable when the slenderness ratio *L/D* = 8 (see Figure 5-13).

Table 5-8: Summary of the calibration results for *Steel4* using UKF and SA for specimen #2 with *L/D* = 8

L/D =8	f_y	b_{ic}	ρ_{ic}	R_{ic}	b_k	b_{kc}	*RRMSE*
SA	367 MPa	-0.017	-5.86	2.21	0.010	0.017	0.134
UKF	360 MPa	-0.014	-5.90	2.17	0.011	0.024	0.141
UKF	(440 MPa)	-0.039	-3.57	1.18	(0.04)	(0.04)	0.178

Note: values in () are fixed as predetermined.

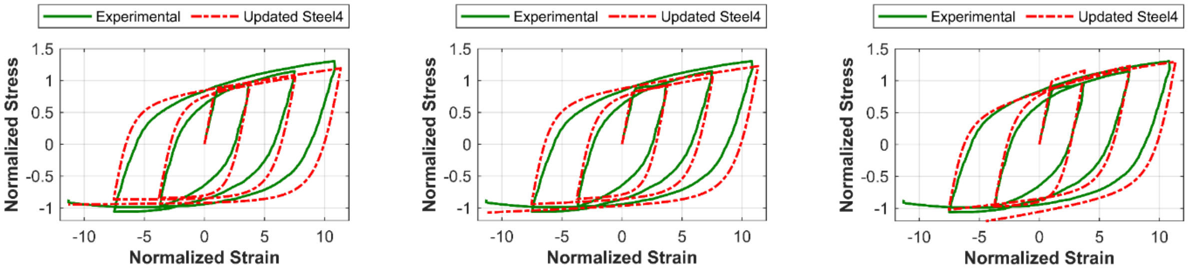

(a) (b) (c)

Figure 5-13: Stress-strain hysteresis comparison between the experiment and the calibrated *Steel4* material model using (a) SA with six parameters, (b) UKF with six parameters, and (c) UKF with three parameters for specimen #2

Specimen #3 represents the steel bar with a large slenderness ratio (*L/D* = 11). The calibrated material parameters and the modeling accuracy for the *Steel4* are summarized in Table 5-9. As can be observed, the difference between the two calibration cases considering six parameters are relatively small and the performance of the calibrated model using UKF is verified by SA (a global optimization technique). The cyclic stress-strain hysteresis of the two *Steel4* material models calibrated are compared with the experimental data, see Figure 5-14 (a) and Figure 5-14 (b). Both approaches led to similar accuracy in representing the stress-strain hysteresis. With a closer look at the stress-strain relationships from both calibrated models (UKF and SA), it can be concluded that both models are capable of achieving excellent match on the compression side while the accuracy on tension side is compromised. As such, it can be concluded that the *Steel4* material is incapable of achieving an acceptable accuracy for the tension and compression response simultaneously of specimen #3. Furthermore, the third case with three parameters calibrated leads to even higher *RRMSE* compared to the cases when considering six parameters (see Figure 5-14 c) as the result of reducing calibration flexibility.

Table 5-9: Summary of the calibration results for *Steel4* using UKF and SA for specimen #3 with *L/D* = 11

	f_y	b_{ic}	ρ_{ic}	R_{ic}	b_k	b_{kc}	*RRMSE*
SA	442 MPa	-0.017	-5.86	2.21	0.036	0.027	0.241
UKF	422 MPa	-0.014	-5.90	2.17	0.031	0.022	0.257
UKF	(440 MPa)	-0.042	-3.54	1.51	(0.04)	(0.04)	0.334

Note: values in () are fixed as predetermined.

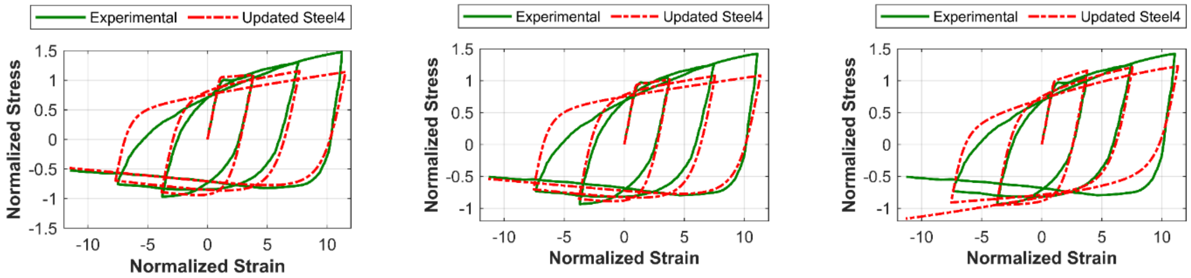

(a) (b) (c)

Figure 5-14: Stress-strain hysteresis comparison between the experiment and the calibrated *Steel4* material model using (a) SA with six parameters, (b) UKF with six parameters, and (c) UKF with three parameters for specimen #3

The calibration results for specimen #4 with SA and UKF are summarized in Table 5-10. The low *RRMSE* values of these two cases indicated excellent accuracy of *Steel4* for specimen #4 (see Figure 5-15). As shown in Figure 5-15 (a) and Figure 5-15 (b), the calibrated the *Steel4* material model agrees well with the experimental data. Furthermore, the third case with three parameters calibrated shows a significantly higher *RRMSE* compared to the case with six parameters calibrated (see Table 5-10). By comparing the stress-strain relationship of the calibrated model and the experimental observations, it can be noticed that the compressive behavior is poorly represented (see Figure 5-15 c). By comparing the calibration result for the six-parameter and three-parameter cases, it can be concluded that parameters f_y, b_k, and b_{kc} are recommend to be calibrated for this specimen to accurately represent its physical aspects.

Table 5-10: Summary of the calibration results for *Steel4* using UKF and SA for specimen #4 with *L/D* = 10

L/D =10	f_y	b_{ic}	ρ_{ic}	R_{ic}	b_k	b_{kc}	*RRMSE*
SA	521 MPa	-0.039	-7.86	2.02	0.021	0.007	0.118
UKF	514 MPa	-0.036	-7.56	2.00	0.020	0.007	0.122
UKF	(520 MPa)	-0.037	-8.32	1.78	(0.01)	(0.01)	0.326

Note: values in () are fixed as predetermined.

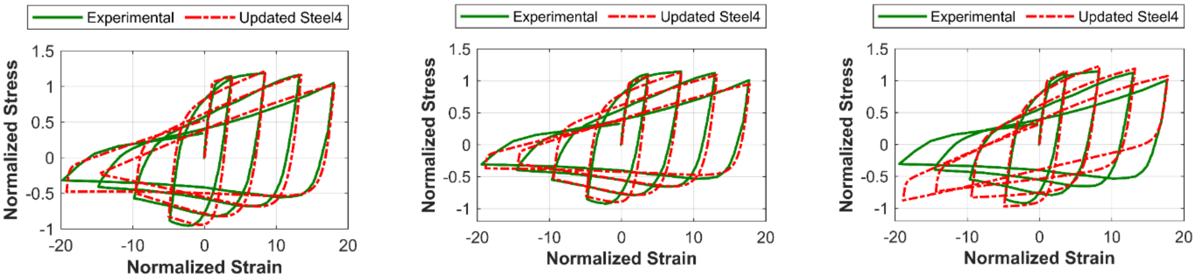

(a) (b) (c)

Figure 5-15: Stress-strain hysteresis comparison between the experiment and the calibrated *Steel4* material model using (a) SA with six parameters, (b) UKF with six parameters, and (c) UKF with three parameters for specimen #4

The calibration results for specimen #5, which represents a steel bar with an extremely large slenderness ratio (*L/D* = 15) accompanied with significant buckling effect, are summarized in Table 5-11. The SA approach has achieved a similar set of material parameter values to the UKF approach after the calibration, showing UKF can successfully identify the optimum parameters. In general, *Steel4* (see Figure 5-16 a and b) failed to represent the material behavior (i.e., the strength degradation on the compression side in the last cycle) of specimen #4. However, with a closer examination at the hysteresis from the calibrated models, *Steel4* model is capable of representing the material behavior with acceptable accuracy when the strain level is not extremely high, (e.g., below $10\varepsilon_y$) where the strain magnitude lower than 0.03. Further reduction in the number of calibration parameters, as in the case considering three parameters in calibration, will sacrifice the accuracy, leading to a relatively larger *RRMSE* and worse match with the experimental stress-strain hysteresis(see Figure 5-16 c). This affirmed that the parameters f_y, b_k, and b_{kc} need to be calibrated for this specimen with a large slenderness ratio.

Table 5-11: Summary of the calibration results for *Steel4* using UKF and SA for specimen #5 with *L/D* = 15

	f_y	b_{ic}	ρ_{ic}	R_{ic}	b_k	b_{kc}	*RRMSE*
SA	424 MPa	-0.045	-8.96	1.66	0.022	0.015	0.361
UKF	428 MPa	-0.044	-8.90	1.67	0.023	0.014	0.369
UKF	(520 MPa)	-0.061	-9.04	1.38	(0.01)	(0.01)	0.445

Note: values in () are fixed as predetermined.

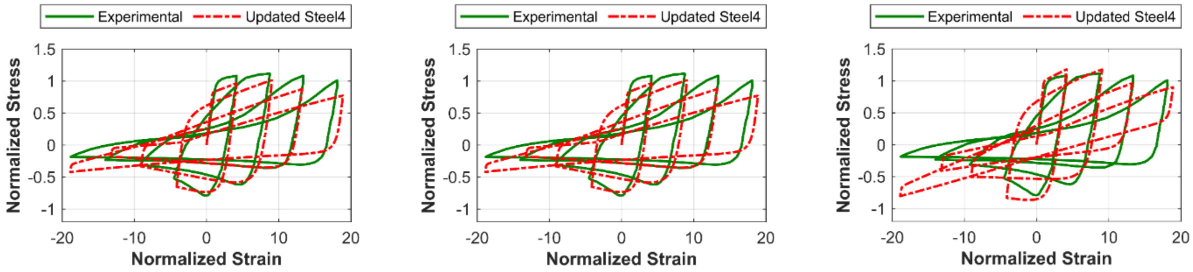

(a) (b) (c)

Figure 5-16 Stress-strain hysteresis comparison between the experiment and the calibrated *Steel4* material model using (a) SA with six parameters, (b) UKF with six parameters, and (c) UKF with three parameters for specimen #5

Based on the calibration results of *Steel4* for all the five specimens considered, it can be concluded that the *Steel4* material model is capable of providing an accurate representation of the stress-strain relationship considering buckling effect of steel rebars with a wide range of *L/D* ratios (e.g., *L/D* = 5 ~ 15) when all six sensitive parameters calibrated. However, the accuracy can be compromised when the strain levels are extremely high (e.g., $\varepsilon > 0.03$). Furthermore, within moderate strain levels (e.g., $\varepsilon < 0.03$), the calibration accuracy is sacrificed little when excluding parameters with less sensitivity (i.e. b_k and b_{kc}) and parameters with low uncertainties (i.e. f_y). Thus, this makes it possible to reduce the computational cost in nonlinear FEMU of bridge structures when *Steel4* is used to model steel rebars with buckling by eliminating these two less important parameters.

5.2.2.3 Buckling steel material model calibration for Reinforcing Steel material

The *Reinforcing Steel (R. Steel)* is a uniaxial material model developed in *OpenSees* to capture physical phenomena, such as buckling, of steel rebars inside RC structures. The *Reinforcing Steel* material model have integrated two optional buckling models: the Gomes and Appleton buckling model (referred to as GA) [84] and Dhakal and Maekawa buckling model (referred to as DM)[85]. In this section, the performance of the two buckling models (i.e., *Reinforcing Steel-GA* and *Reinforcing Steel-DM*) are assessed using the five specimens identified from the literature.

The elastic behavior of the *Reinforcing Steel* material is defined by the yield strength f_y and the Young's modulus E_s; and the tensile hardening is controlled by the ultimate strength f_u, the initial hardening stiffness E_{sh}, the strain corresponding to the initial strain hardening e_{sh}, and the strain at the ultimate strength e_{ult}. In terms of the buckling behavior, the GA buckling model requires four additional parameters, including the slenderness ratio l_{sr}, the amplification factor β, the buckling reduction factor r, and a buckling constant γ are required. In contrast, the DM buckling model is defined by two material parameters, namely, the slenderness ratio l_{sr} and the adjustment constant α.

Table 5-12: Summary of the center value θ_0 used for the perturbation analysis of *Reinforcing Steel* material

Tensile model parameters					
f_y	E_s	f_u	E_{sh}	e_{sh}	e_{ult}
520 MPa	196 GPa	744 MPa	1.96 GPa	$1.5f_y/E_s$	0.15
GA buckling model parameters				DM buckling model parameters	
l_{sr}	β	γ	r	l_{sr}	α
8	1.5	0.5	0.5	8	0.875

Local sensitivity analysis is conducted for obtaining a better understanding of the role of each parameter and further guide the parameter selection for material calibration. This is achieved by one-at-a-time perturbation analysis, in which a parameter is varied by $\pm 10\%\ \theta_0$ and $\pm 20\%\ \theta_0$ around the center value (θ_0), which are listed in Table 5-12. To be noted that in order to avoid numerical problem with this material model (extremely high elastic modulus when $e_{sh} \approx e_{yield}$), the value of parameter e_{sh} is assumed as 1.5 times of e_{yield}, namely, assuming the yield plateau is about a constant percentage (e.g., 50%) of the yield strain.

Figure 5-17 presents the perturbation analysis results for the three most sensitive material parameters for the *Reinforcing Steel* model in terms of the tensile behavior. They are the yield strength f_y, the Young's modulus E_s, and the initial hardening stiffness E_{sh}. It can be observed that the yield strength f_y has the highest sensitivity (see Figure 5-17 a), while parameters E_s and E_{sh} have relatively lower sensitivities and they control the pre-yielding branch and post-yielding branch, respectively (see Figure 5-17 b and c).

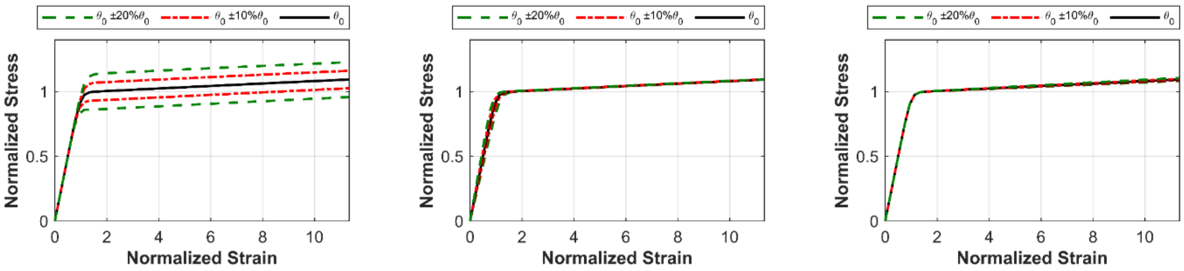

(a) (b) (c)

Figure 5-17: Perturbation analysis for the tension branch of *Reinforcing Steel* with parameter: (a)f_y , (b) E_s, and (c) E_{sh}

Figure 5-18 presents the perturbation analysis results for the four most sensitive material parameters for the *Reinforcing Steel-GA* model in terms of the compressive behavior. They are f_y, E_s , l_{sr}, and r. Parameters f_y and E_s affects the compressive behavior in a similar manner to the tensile behavior, where f_y controls the initial point of the post-yield branch and E_s controls the slope of the elastic branch, and both parameters do not affect the post-yield formulation. As shown in Figure 5-18 (c) and Figure 5-18 (d), the shape of the post-buckling curve is mainly controlled by l_{sr} and r.

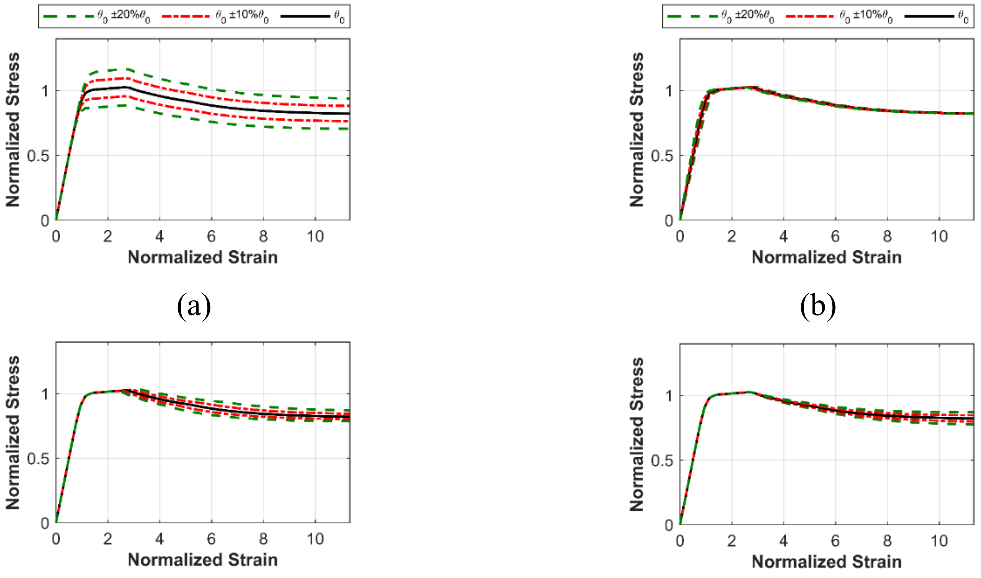

(a) (b) (c) (d)

Figure 5-18: Perturbation analysis for the monotonic stress-strain of *Reinforcing Steel-GA* model on tension branch with parameter: (a) f_y, (b) E_s, (c) l_{sr}, and (d) r

Table 5-19 provides the perturbation analysis results for the cyclic behavior of the five most sensitive parameters of the *Reinforcing Steel-GA* model, which lead to similar conclusions as in the monotonic sensitivity analysis. Specifically, for tensile parameters, f_y and E_s have a high sensitivity and affect both tension and compression sides in terms of cyclic behavior, while the parameter E_{sh} have moderate sensitivity for the monotonic behavior and low sensitivity for the cyclic behavior. Among the four buckling-related parameters, two of them (l_{sr} and r) show a high sensitivity in the cyclic behavior.

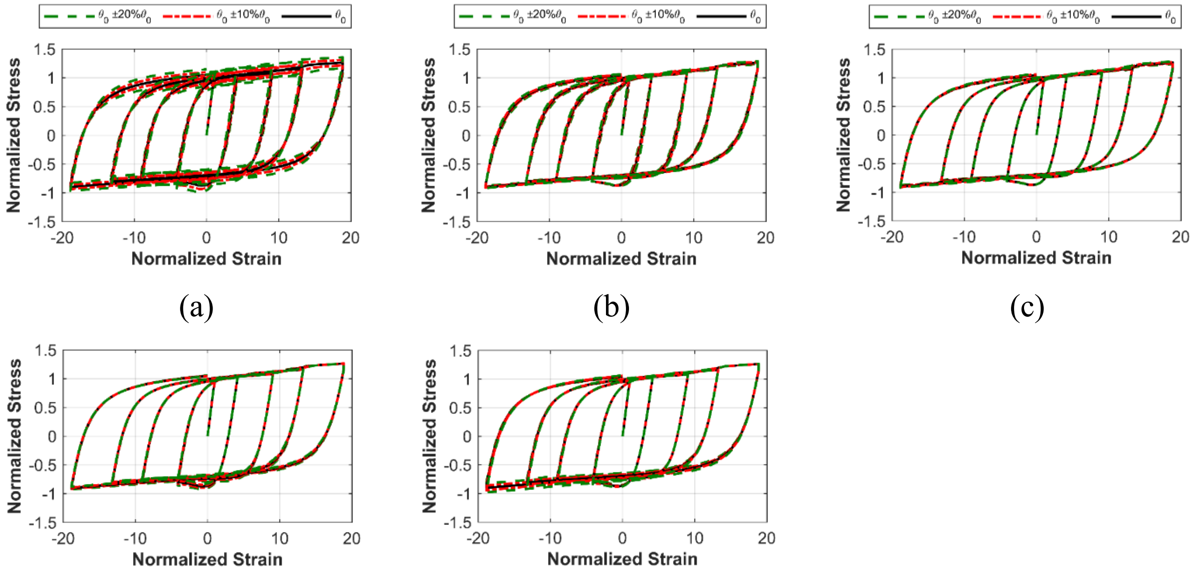

(a) (b) (c)

(d) (e)

Figure 5-19: Perturbation analysis for the cyclic stress-strain of *Reinforcing Steel-GA* model with parameter: (a) f_y, (b) E_s, (c) E_{sh}, (d) l_{sr}, and (e) r

Figure 5-20 presents perturbation analysis results for the four most sensitive material parameters of the *Reinforcing Steel-DM* model in terms of the compressive behavior. The roles of the parameters f_y and E_s are similar as in the GA model, where E_s controls the initial stiffness of the pre- and post-yield branch, and f_y controls the starting stress and strain of the post-yield curvature. On the other hand, the shape of the buckling curve is controlled by parameters l_{sr} and α and both parameters affect the initial slope of the post-yield curve.

(a) (b)

(c) (d)

Figure 5-20: Perturbation analysis for the monotonic stress-strain of *Reinforcing Steel-DM* model on tension branch with parameter : (a) f_y, (b) E_s, (c) l_{sr}, and (d) α

Error! Reference source not found. provides the perturbation analysis results for the most five sensitive parameters of the *Reinforcing Steel-DM* model in terms of cyclic behavior, which lead to similar conclusions as in the monotonic sensitivity analysis. Specifically, parameters f_y and E_s have a high sensitivity and affect both the tension and compression sides in terms of cyclic behavior, while E_{sh} shows a low sensitivity. On contrary, the two parameters (α and l_{sr}) govern the compressive behavior with buckling effect.

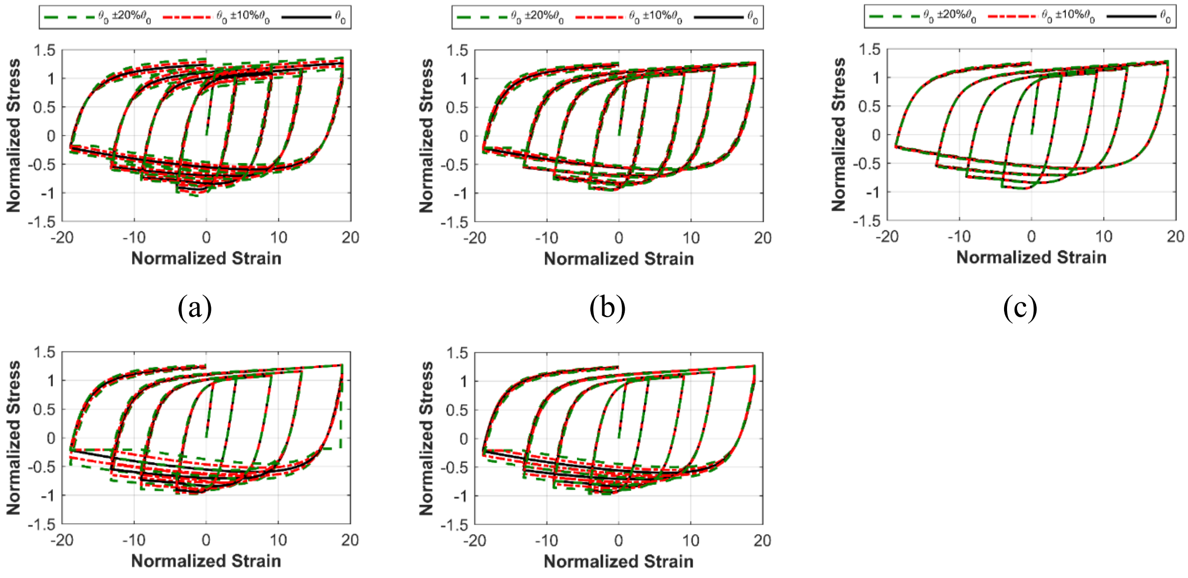

(a) (b) (c)

(d) (e)

Figure 5-21: Perturbation analysis for the cyclic stress-strain of *Reinforcing Steel-DM* model with parameter: (a) f_y, (b) E_s, (c) E_{sh}, (d) l_{sr}, and (e) α

By combining the knowledge obtained from the monotonic and cyclic sensitivity analysis, the calibration parameters can be determined. For both the *Reinforcing Steel-GA and Reinforcing Steel-DM* models, the elastic parameters (f_y and E_s) are very sensitive for both monotonic and cyclic behaviors and are required for material model calibration. In terms of the asymmetrical behavior of the steel rebar considering buckling, two additional parameters (l_{sr} and r) are calibrated for the *Reinforcing Steel-GA* model and two more parameters (l_{sr} and α) are calibrated for the *Reinforcing Steel-DM* model.

To further verify the possibilities in reducing the modeling complexity, an additional case is designed for UKF with fewer material parameters considered for calibration. As such, for both buckling models, parameters f_y and E_s are fixed in this case as measured from the material tests of specimen #1 ~ #5, while the parameter r in the *Reinforcing Steel-GA* model and α in the *Reinforcing Steel-DM* model is also fixed considering that the buckling curve can be controlled by the parameter l_{sr} to a degree.

The UKF-based Bayesian optimization is used for model calibration and the SA approach (with 1000 iterations) is then used for the purpose of cross-verification. The material model calibration results for specimen #1 are summarized in Table 5-13, including the calibrated parameter values from UKF and SA, as well as the modeling accuracy quantified by *RRMSE*.

Table 5-13: Summary of the calibration results for *Reinforcing Steel* using UKF and SA for specimen #1 with *L/D*=5

		f_y	E_s	l_{sr}	β	α	*RRMSE*
Reinforcing Steel-GA	SA	398 MPa	114.2 GPa	4.61	1.48	N/A	0.133
	UKF	403 MPa	113.5 GPa	5.14	1.49	N/A	0.145
	UKF	(440 MPa)	(196 GPa)	9.89	1.50	N/A	0.246
Reinforcing Steel-DM	SA	395 MPa	114.2 GPa	5.75	N/A	0.85	0.124
	UKF	393 MPa	113.6 GPa	6.10	N/A	0.85	0.136
	UKF	(440 MPa)	(196 GPa)	6.44	N/A	0.86	0.253

Note: values in () are fixed as predetermined.

The calibrations results show that the UKF-based optimization can achieve approximately the same results as SA for both *Reinforcing Steel-GA* and *Reinforcing Steel-DM* material models. The low values of *RRMSE* indicate both the DM and GA buckling model with four calibration parameters represent the experimental stress-strain hysteresis reasonably well (see Figure 5-22 a, b, and Figure 5-23 a and b).

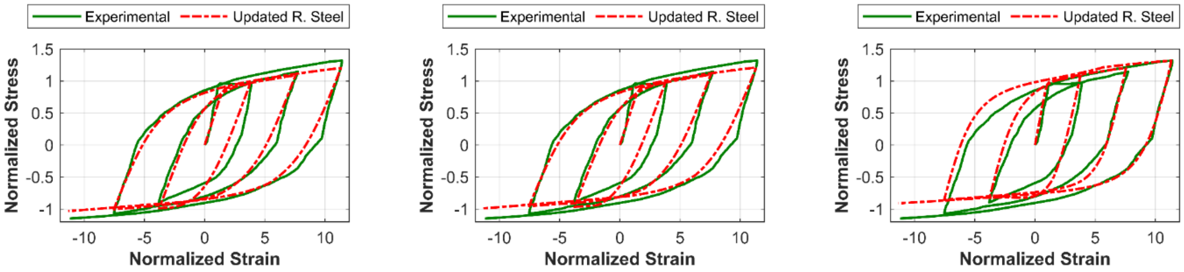

(a) (b) (c)

Figure 5-22: Stress-strain hysteresis comparison between the experiment and the calibrated *Reinforcing Steel-GA* material model using (a) SA with six parameters, (b) UKF with six parameters, and (c) UKF with three parameters for specimen #1

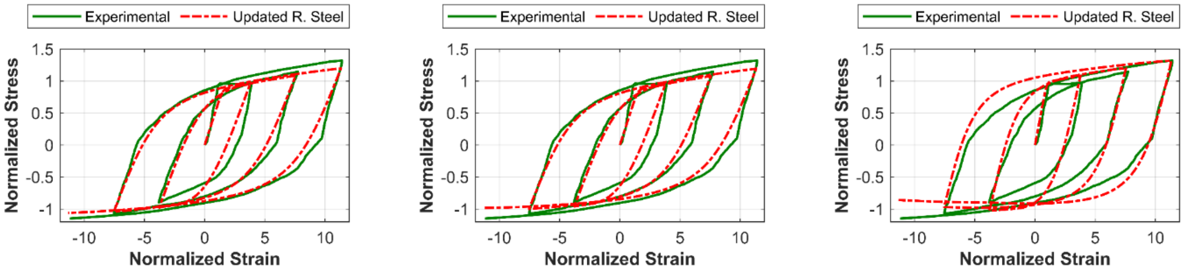

(a) (b) (c)

Figure 5-23: Stress-strain hysteresis comparison between the experiment and the calibrated *Reinforcing Steel*-DM material model using (a) SA with six parameters, (b) UKF with six parameters, and (c) UKF with three parameters for specimen #1

Moreover, the slenderness ratio (l_{sr}) is estimated to be within the range of 4.61 and 6.10, which agrees well with the nominal slenderness ratio (*L/D*=5) for specimen #1. However, the modulus of elasticity E_s is estimated to be much lower than tested value as a compromise to achieve a good correlation with the experimental results. In contrast, when only two parameters are calibrated, both *Reinforcing Steel-GA* and *Reinforcing Steel-DM* models failed to represent the experimental stress-strain hysteresis of specimen #1 (see Figure 5-22 c and Figure 5-23 c)

The calibration results of *Reinforcing Steel-GA* and *Reinforcing Steel-DM* for specimen #2 are summarized in Table 5-14. Low *RRMSE* values indicate that both models with four parameters calibrated can represent reasonably well the cyclic stress-strain behavior of specimen #2, see Figure 5-24 (a), (b) and Figure 5-25 (a), (b).In addition, the close estimate of the material parameter values from UKF and GA verified that the UKF's capability for calibration. It is worth pointing out that, parameters f_y and E_s in both GA and DM buckling model converged to a much lower/higher value compared to the experimental observations, while l_{sr} in is underestimated compared to the nominal slenderness ratio (*L/D*=8), particularly in the GA buckling model. In contrast, the two cases of GA and DM with two calibration parameters show slightly higher *RRMSE* values compared to the cases when four parameters are calibrated (Figure 5-24 c and Figure 5-25 c).

Table 5-14: Summary of the calibration results for *Reinforcing Steel* using UKF and SA for specimen #2 with *L/D*=8

		f_y	E_s	l_{sr}	β	α	*RRMSE*
Reinforcing Steel-GA	SA	320 MPa	241 GPa	3.41	1.49	N/A	0.141
	UKF	331 MPa	230 GPa	3.64	1.49	N/A	0.143
	UKF	(440 MPa)	(196 GPa)	6.45	1.50	N/A	0.185
Reinforcing Steel-DM	SA	331 MPa	237 GPa	5.82	N/A	0.88	0.138
	UKF	337 MPa	230 GPa	6.49	N/A	0.87	0.144
	UKF	(440 MPa)	(196 GPa)	7.57	N/A	0.85	0.158

Note: values in () are fixed as predetermined.

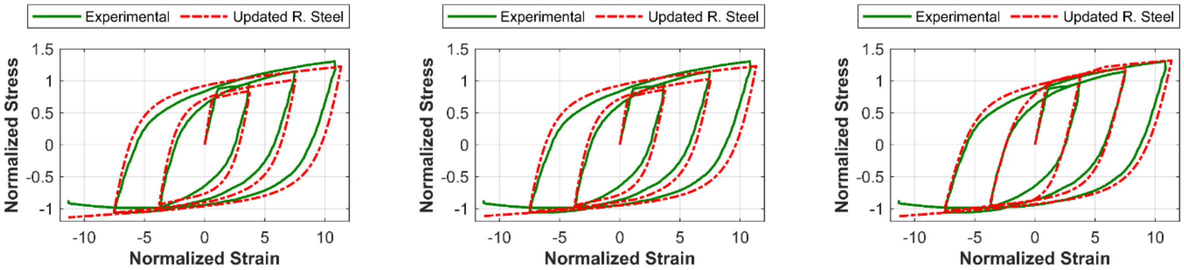

(a) (b) (c)

Figure 5-24: Stress-strain hysteresis comparison between the experiment and the calibrated *Reinforcing Steel-GA* material model using (a) SA with six parameters, (b) UKF with six parameters, and (c) UKF with three parameters for specimen #2

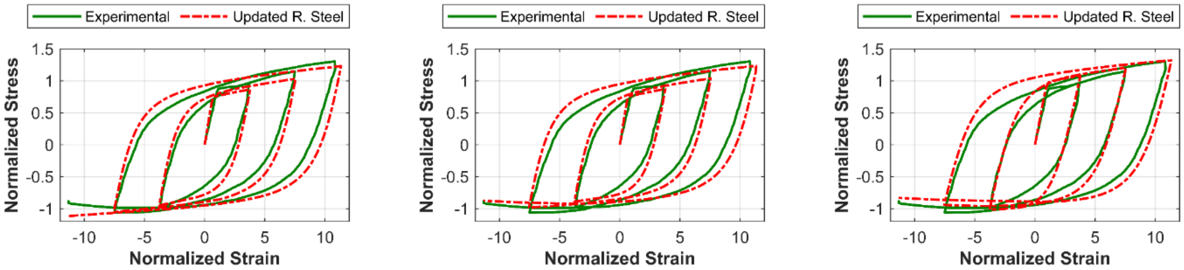

(a) (b) (c)

Figure 5-25: Stress-strain hysteresis comparison between the experiment and the calibrated *Reinforcing Steel-DM* material model using (a) SA with six parameters, (b) UKF with six parameters, and (c) UKF with three parameters for specimen #2

The parametric calibration results of *Reinforcing Steel-GA* and *Reinforcing Steel-DM* for specimen #3 are summarized in Table 5-15. The *RRMSE* values are relatively high (i.e., above 30%), indicating both DM and GA buckling models are not able to model the cyclic stress-strain behavior of specimen #3. The estimate of the parameters is way off as well: for example, the slenderness ratio is significantly underestimated. This is further verified by the comparison of the cyclic stress-strain hysteresis as shown in Figure 5-26 (a), (b), and Figure 5-27(a), (b). The models with fewer calibration parameters (see Figure 5-26 c and Figure 5-27 c) show slightly higher *RRMSE* values and lead to even worse performance.

Table 5-15: Summary of the calibration results for *Reinforcing Steel* using UKF and SA for specimen #3 with *L/D*=11

		f_y	E_s	l_{sr}	β	α	*RRMSE*
Reinforcing Steel-GA	SA	308 MPa	296 GPa	4.91	1.4	N/A	0.325
	UKF	335 MPa	243 GPa	5.39	1.5	N/A	0.330
	UKF	(440 MPa)	(196 GPa)	8.21	1.5	N/A	0.336
Reinforcing Steel-DM	SA	388 MPa	243 GPa	7.76	N/A	0.88	0.303
	UKF	389 MPa	244 GPa	7.64	N/A	0.88	0.311
	UKF	(440 MPa)	(196 GPa)	8.16	N/A	0.87	0.316

Note: values in () are fixed as predetermined.

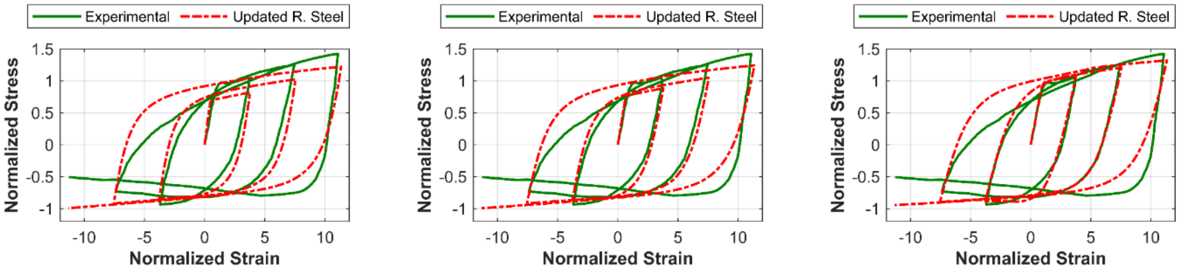

(a) (b) (c)

Figure 5-26: Stress-strain hysteresis comparison between the experiment and the calibrated *Reinforcing Steel-GA* material model using (a) SA with six parameters, (b) UKF with six parameters and (c) UKF with three parameters for specimen #3

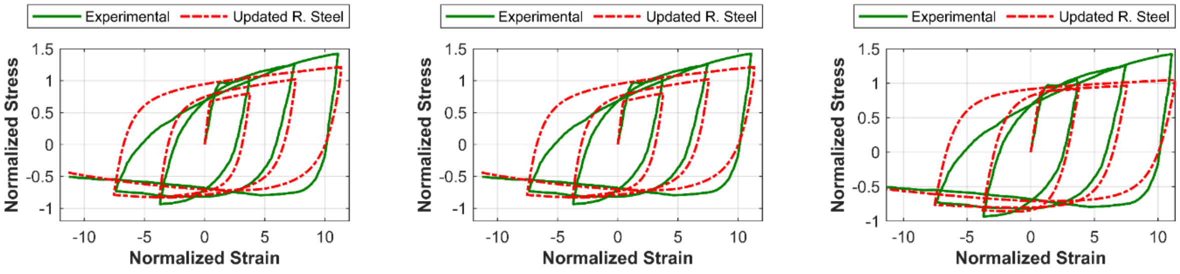

(a) (b) (c)

Figure 5-27: Stress-strain hysteresis comparison between the experiment and the calibrated *Reinforcing Steel-DM* material model using (a) SA with six parameters, (b) UKF with six parameters and (c) UKF with three parameters for specimen #3

The model calibration results for both material models for specimen #4 test data are summarized in Table 5-16. On the one hand, the UKF-calibrated material parameters have shown a good agreement with SA-calibration cases for each buckling model. On the other hand, the *RRMSE* for all four major material calibration cases are above 40%, indicating the *Reinforcing Steel* material failed to achieve a good representation on the physical behavior on specimen #4. This inference have been verified by the stress-strain relationship as shown in Figure 5-28 (a), (b) and Figure 5-29 (a), (b), where the calibrated material model with GA and DM buckling model have failed to reproduce both hardening and the buckling effect in the cyclic behavior. Such inabilities in appropriately modeling the hardening branch have resulted in a severe underestimation of parameter f_y and E_s. Furthermore, the two extra cases (Figure 5-28 c and Figure 5-29 c) have shown a worse modeling accuracy comparing to the cases with full flexibility.

Table 5-16: Summary of the calibration results for *Reinforcing Steel* using UKF and SA for the specimen #4 with *L/D*=10

		f_y	E_s	l_{sr}	β	α	*RRMSE*
Reinforcing Steel-GA	SA	345 MPa	101.2 GPa	5.27	1.48	N/A	0.407
	UKF	347 MPa	96.6 GPa	5.35	1.48	N/A	0.411
	UKF	(520 MPa)	(196 GPa)	16.3	1.51	N/A	0.461
Reinforcing Steel-DM	SA	344 MPa	102.2 GPa	7.20	N/A	0.86	0.413
	UKF	347 MPa	96.6 GPa	7.13	N/A	0.88	0.429
	UKF	(520 MPa)	(196 GPa)	7.85	N/A	0.87	0.493

Note: values in () are fixed as predetermined.

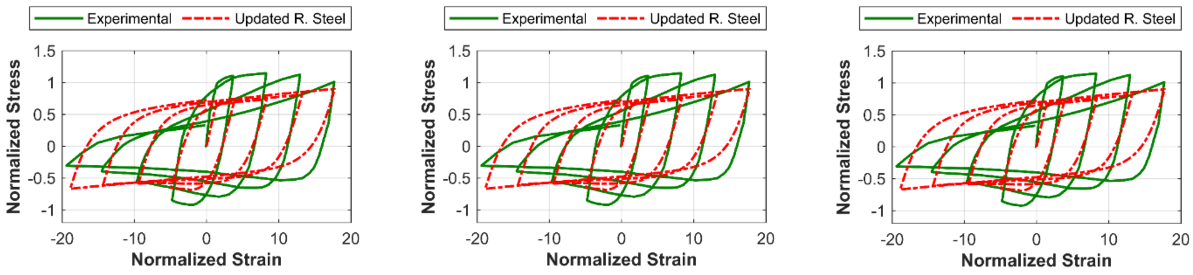

(a) (b) (c)

Figure 5-28: Stress-strain hysteresis comparison between the experiment and the calibrated *Reinforcing Steel-GA* material model using (a) SA with six parameters, (b) UKF with six parameters and (c) UKF with three parameters for specimen #4

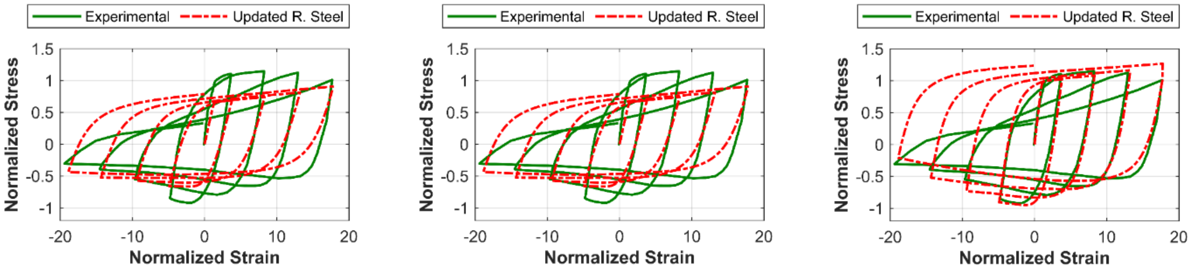

(a) (b) (c)

Figure 5-29: Stress-strain hysteresis comparison between the experiment and the calibrated *Reinforcing Steel-DM* material model using (a) SA with six parameters, (b) UKF with six parameters and (c) UKF with three parameters for specimen #4

The material calibration on *Reinforcing Steel* material for specimen #5 is performed follows a similar analysis scheme and the analysis results are summarized in Table 5-17 below. All six cases have shown a very poor modeling accuracy as the value of *RRMSE* for each case is higher than 65%.

Table 5-17: Summary of the calibration results for *Reinforcing Steel* using UKF and SA for the specimen #5 with *L/D*=15

		f_y	E_s	l_{sr}	β	α	*RRMSE*
Reinforcing Steel-GA	SA	278 MPa	61.2 GPa	6.27	1.48	N/A	0.661
	UKF	242 MPa	45.9 GPa	6.65	1.48	N/A	0.644
	UKF	(520 MPa)	(196 GPa)	8.3	1.51	N/A	0.639
Reinforcing Steel-DM	SA	261 MPa	54.3 GPa	10.39	N/A	0.84	0.622
	UKF	256 MPa	53.6 GPa	9.59	N/A	0.84	0.608
	UKF	(520 MPa)	(196 GPa)	10.55	N/A	0.84	0.702

Note: values in () are fixed as predetermined

The poor modeling accuracy could be further verified by Figure 5-30 (a), (b), and Figure 5-31(a), (b), where both GA and DM buckling model have failed to correctly represent the cyclic behavior in both tension and compression side. The two cases with reduced calibration complexity as shown Figure 5-30 (c) and Figure 5-31 (c) also shown a poor match corresponding to the true response. As such, it can be concluded that the *Reinforcing Steel* material GA and DM buckling model is not able to model specimen #5.

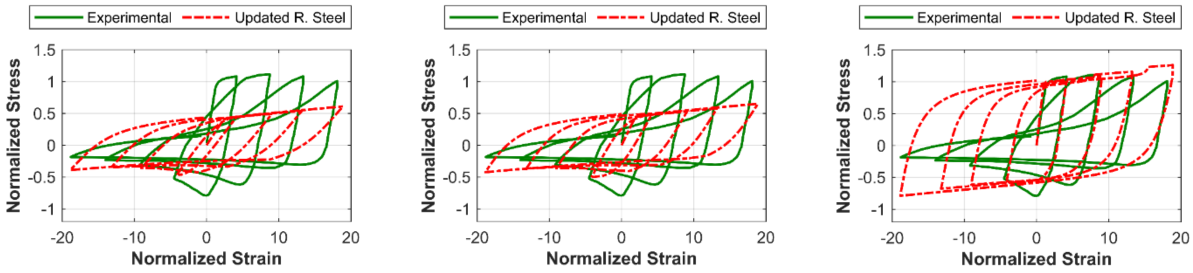

(a) (b) (c)

Figure 5-30: Stress-strain hysteresis comparison between the experiment and the calibrated *Reinforcing Steel-GA* material model using (a) SA with six parameters, (b) UKF with six parameters and (c) UKF with three parameters for specimen #5

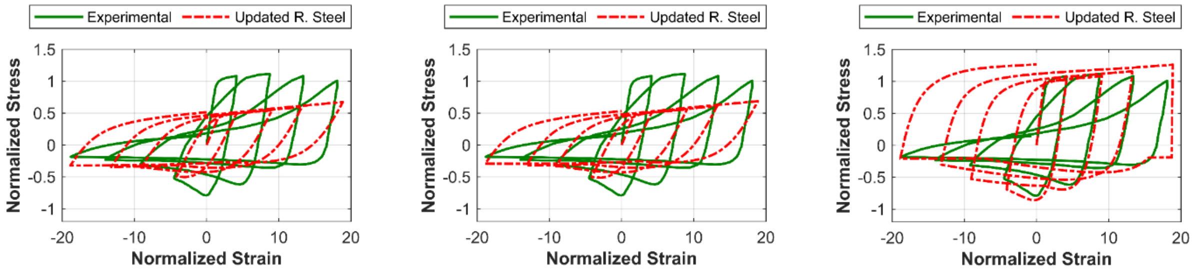

(a) (b) (c)

Figure 5-31: Stress-strain hysteresis comparison between the experiment and the calibrated *Reinforcing Steel-DM* material model using (a) SA with six parameters, (b) UKF with six parameters and (c) UKF with three parameters for specimen #5

Based on the observation among the calibration results of *Reinforcing Steel* at all five specimens, the modeling accuracy is equivalent among the five experimental cases studied. It can be concluded that the *Reinforcing Steel* material with GA and DM model is only capable of providing an accurate representation of the stress-strain relationship in a low *L/D* ratio (i.e. less than 8).

Furthermore, within the effective range of *L/D* ratio the parameter-reduction strategy is capable of sacrificing a reasonable accuracy to achieve a lower computational cost.

5.2.2.4 Buckling steel material model calibration for Corroded Buckling Steel

The *C.B. Steel* (*Corroded buckling steel*) material model, which was developed to represent the buckling effect with optional capabilities of considering different level of corrosion by Kashani, et al.[25], is recently implemented into *OpenSees* in the Structural Modeling and Reliability Analysis research group at the University of Alberta. The tension backbone curve of the *C.B. Steel* material is defined by the modified Giuffre–Menegotto–Pinto (GMP) formulation, where the yield strength f_y, elastic modulus E_s, and initial stiffness-hardening ratio b_{sh} is mandatory. The buckling behavior on the tensile branch is governed by the slenderness ratio *L/D* and the optional corrosion-related material parameters (δ and Cor) are out of the scope of this study and are neglected in this section.

The aforementioned one-at-a-time perturbation analysis is performed on the *C.B. Steel* material parameters to examine their local sensitivity. Each of the modeling parameters are perturbated by $\pm 10\%\ \theta_0$ and $\pm 20\%\ \theta_0$ around the center value (θ_0) defined as depicted in Table 5-18.

Table 5-18: Summary of the center value θ_0 used for the perturbation analysis of *C.B. Steel* material

C.B. Steel material parameters					
f_y	E_s	b_{sh}	L/D	δ	Cor
520 MPa	196 GPa	0.01	8	0.06	0

Figure 5-32 presents the perturbation analysis results for all three material parameters that contributes to the material tensile behavior. Among the three material parameters, the yield strength f_y have the highest sensitivity and governs both yield stress and yield strain. The elastic modulus E_s and strain hardening ratio b_{sh} have shown a moderate impact on the material behavior, which both governs the slope of both elastic and plastic behavior of the material model.

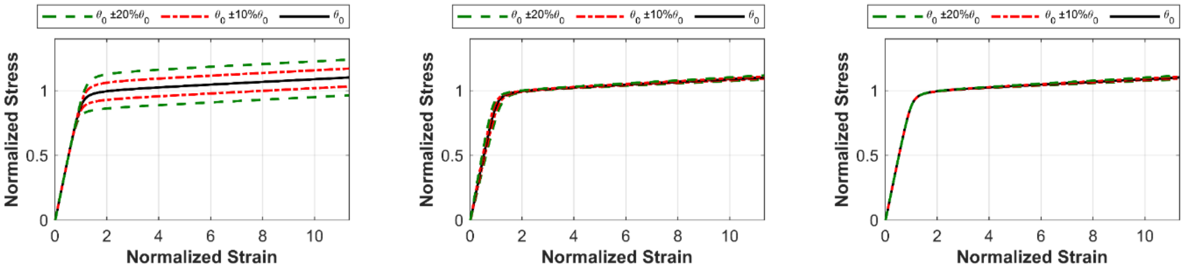

(a) (b) (c)

Figure 5-32: Perturbation analysis for the tension branch of *C.B. Steel* with parameter: (a)f_y , (b) E_s, and (c) b_{sh}

The perturbation analysis results of the three sensitive material parameters for the compressive behavior are shown in Figure 5-33. As can be observed in Figure 5-33 (a) and (b), the elastic parameters are also affecting the compression backbone curve. The yield strength f_y in the compression branch serves as a similar role as the tensile branch, where it controls the yield stress and strain and the elastic modulus E_s expressed a relatively low sensitivity and only affects the stiffness of material elastic behavior. The slenderness ratio L/D is the most sensitive parameter for the buckling effect and contributes the most to the shape of the post-yield relationship by governing the post-yield stiffness (see Figure 5-33 c).

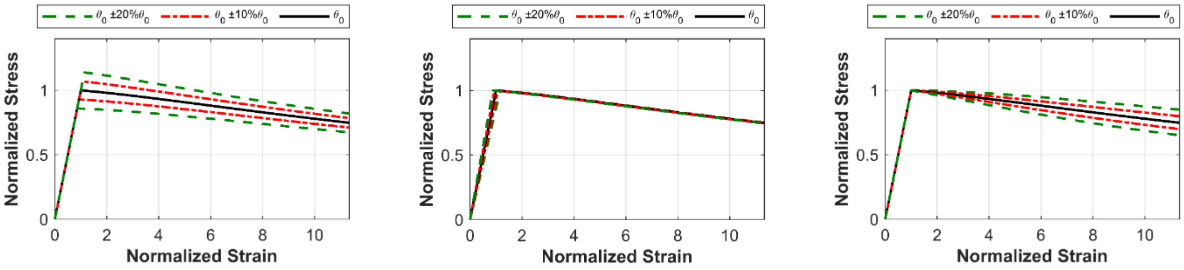

(a) (b) (c)

Figure 5-33: Perturbation analysis for the compression branch of *C.B. Steel* with parameter: (a) f_y, (b) E_s, and (c) L/D

For the four most sensitive parameters (f_y, E_s, b_{sh}, and L/D) identified in the monotonic sensitivity analysis on both tension and compression side, the cyclic sensitivity analysis is performed. The perturbation analysis results for the cyclic behavior for all these four material parameters identified is presented in Figure 5-34. As can be observed in Figure 5-34 (a) and (b), the elasticity parameter f_y and E_s are very sensitive in both tensile and compression branch of the material cyclic envelope. Parameter L/D have shown a significant sensitivity on the buckling behavior only (Figure 5-34 c), while the strain hardening ratio b_{sh}, does not have a significant sensitivity on the material cyclic behavior (Figure 5-34 d).

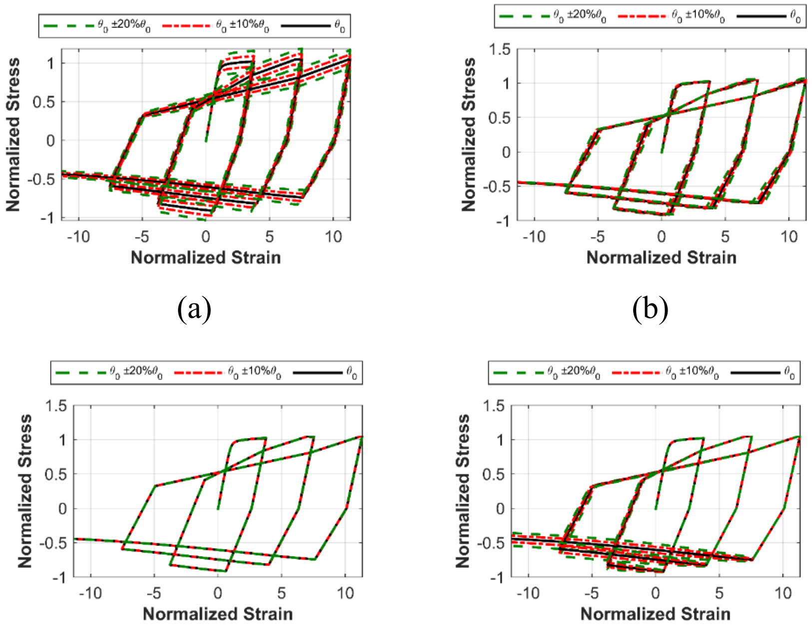

(a) (b)

(c) (d)

Figure 5-34: Perturbation analysis for the cyclic behavior of *C.B. Steel* with parameter: (a) f_y, (b) E_s, (c) b_{sh}, and (d) L/D

The information provided by the parameter perturbation analysis provides valuable information to guide the calibration parameter selection. To sum up, parameters f_y and E_s have significant effects on the tensile hardening and compressive buckling behaviors; L/D has a major influence on the material buckling behavior and thus only the compressive behavior in the cyclic analysis. As such, these three material parameters are calibrated in accordance with the experimental data. In addition to the case where all three sensitive parameters are included, one more calibration case is studied to consider the possibility of reducing the number of calibration parameters, for example, by eliminating the less important or less uncertain parameters (e.g., f_y and E_s). As such, one extra case of model calibration is considered considering that f_y and E_s are typically available if material coupon test data exist, and they can be assumed as known and only the slenderness ratio L/D is calibrated.

The calibration results of *C.B. Steel* material model for specimen #1, including the calibration parameters and modeling accuracy, are summarized in Table 5-19. The calibrated model parameter values from UKF and SA are close, showing that UKF achieved similar calibration accuracy as the SA. The *RRMSE* values are relatively high (i.e., greater than 30%), showing that the *C.B. Steel* material model is not capable of simulating the cyclic stress-strain response of specimen #1 accurately.

Table 5-19: Summary of the calibration results for *C.B Steel material* using UKF and SA for the specimen #1 with *L/D*=5

	f_y	E_s	L/D	*RRMSE*
SA	521 MPa	126 GPa	7.91	0.315
UKF	527 MPa	137 GPa	7.84	0.348
UKF	(440 MPa)	(196 GPa)	5.37	0.379

Note: values in () are fixed as predetermined.

The poor modeling accuracy is revealed by the comparison between the calibrated model and the experimental measurement (see Figure 5-35). With a closer examination, it can be noticed that for both cases using SA and UKF, the hardening effect is underestimated and the buckling effect is overestimated, which result in the over-estimation of the yield strength and underestimation of the elastic modulus. In addition, the third case considering only one calibration parameter (see Figure 5-35 c) shows even worse representation of the steel stress-strain relationship.

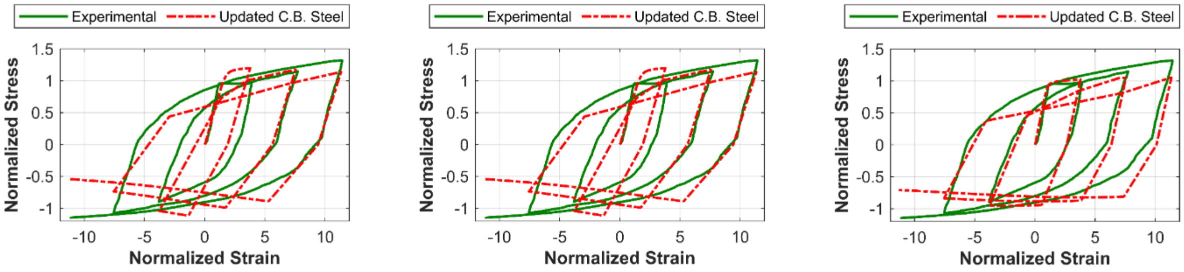

(a) (b) (c)

Figure 5-35: Stress-strain hysteresis comparison between the experiment and the calibrated *C.B Steel* using (a) SA with six parameters, (b) UKF with six parameters, and (c) UKF with three parameters for specimen #1

The calibration results of the *C.B. Steel* material model for specimen #2 for all the three cases and the modeling accuracy are summarized in Table 5-20. Similar as the calibration results for specimen #1, UKF have successfully identified the parameters and the calibrated parameters agree well with those from SA. However, the overall performance of the calibrated model is still poor and the *RRMSE* values of the three cases are higher than 30%, indicating that a low modeling accuracy is achieved after the parameter calibration (see Figure 5-36 a and b). A significant mismatch between the experiment and model prediction can be observed in the cyclic stress-strain hysteresis. In addition. the third case with only one parameter (*L/D*) calibrated also shows poor modeling accuracy, with *RRMSE* = 35% for specimen #2 (see Figure 5-36 c).

Table 5-20: Summary of the calibration results for *C.B Steel material* using UKF and SA for the specimen #2 with *L/D*=8

	f_y	E_s	L/D	*RRMSE*
SA	486 MPa	241 GPa	6.55	0.296
UKF	488 MPa	232 GPa	6.71	0.334
UKF	(440 MPa)	(196 GPa)	6.09	0.348

Note: values in () are fixed as predetermined.

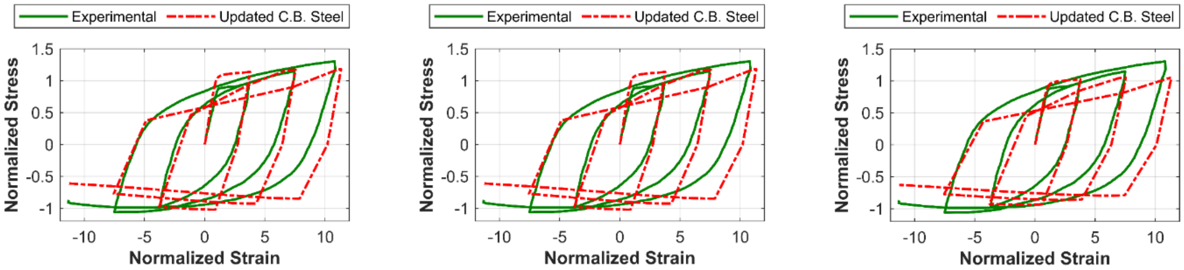

(a) (b) (c)

Figure 5-36: Stress-strain hysteresis comparison between the experiment and the calibrated *C.B Steel* using (a) SA with six parameters, (b) UKF with six parameters, and (c) UKF with three parameters for specimen #2

The parameter calibration results of the *C.B. Steel* material model for specimen #3 are summarized in Table 5-21, where the parameters calibrated by UKF and SA reached a slightly different values. The material model calibrated by SA provides more reasonable estimate of parameters f_y and E_s, which are close to the experimental observations, while UKF suggested higher values of f_y and E_s. The cyclic response of both calibrated models are shown in Figure 5-37 (a) and (b), with the *RRMSE* values for the UKF and SA cases higher than 30%, indicating poor modeling accuracy. The third case with one parameter calibrated also failed to achieve a good representation on the cyclic behavior with a high *RRMSE* (38%). Thus, it can be concluded that the *C.B. Steel* material model is not capable of achieving a high modeling accuracy for specimen #3.

Table 5-21: Summary of the calibration results for *C.B Steel material* using UKF and SA for the specimen #3 with *L/D*=11

	f_y	E_s	L/D	*RRMSE*
SA	445 MPa	202 GPa	6.55	0.326
UKF	488 MPa	317 GPa	6.71	0.352
UKF	(440 MPa)	(196 GPa)	6.09	0.382

Note: values in () are fixed as predetermined.

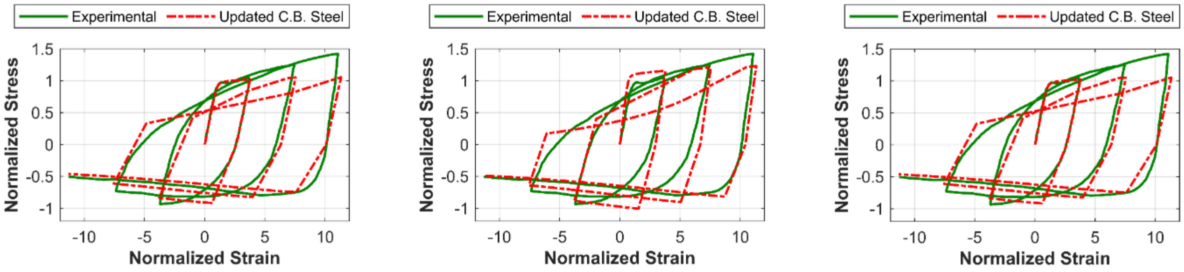

(a) (b) (c)

Figure 5-37: Stress-strain hysteresis comparison between the experiment and the calibrated *C.B Steel* using (a) SA with six parameters, (b) UKF with six parameters, and (c) UKF with three parameters for specimen #3

The material calibration results for specimen #4 are summarized as Table 5-22. UKF led to approximately the same material parameter values as SA. The low *RRMSE* values (less than 20%) suggest a good correlation with the experimental measurement. Despite the minor mismatch on the elastic-plastic transition point, the compression branch matched well with the experimental data (see Figure 5-38 a and b). Furthermore, the third case achieved similar accuracy as the two cases discussed above (see Figure 5-38 c). As such, it can be concluded that an excellent matching with the experimental measurement can be achieved by the C.B steel material for specimen #4 and the one-parameter calibration case is applicable in this specimen.

Table 5-22: Summary of the calibration results for *C.B. Steel material* using UKF and SA for the specimen #4 with *L/D*=10

	f_y	E_s	L/D	*RRMSE*
SA	543 MPa	206 GPa	8.60	0.173
UKF	541 MPa	205 GPa	8.56	0.175
UKF	(520 MPa)	(196 GPa)	8.02	0.192

* Values in () are fixed as predetermined.

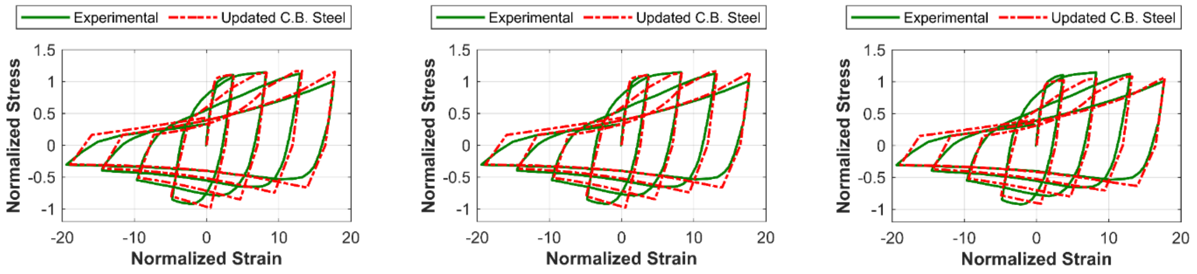

(a) (b) (c)

Figure 5-38: Stress-strain hysteresis comparison between the experiment and the calibrated *C.B Steel* using (a) SA with six parameters, (b) UKF with six parameters, and (c) UKF with three parameters for specimen #4

The material calibration results for specimen #5 is summarized as Table 5-23, where the modeling parameters calibrated by UKF and SA converged to similar magnitude, showing that UKF approximately reached the global optimum identified by SA. Though the *RRMSE* for the three cases are slightly larger than 30%, the cyclic response of the calibrated material model is can represent the general material behaviour reasonably well (Figure 5-39 a and b). In addition, the third case achieved an equivalent accuracy as the two aforementioned cases (see Figure 5-39 c). In sum, the *C.B Steel* material model is capable of achieving a relatively accurate representation on specimen #5.

Table 5-23: Summary of the calibration results for *C.B Steel material* using UKF and SA for the specimen #5 with *L/D*=15

	f_y	E_s	L/D	*RRMSE*
SA	455 MPa	106 GPa	12.87	0.337
UKF	461 MPa	106 GPa	12.64	0.355
UKF	(520 MPa)	(196 GPa)	12.56	0.357

* Values in () are fixed as predetermined.

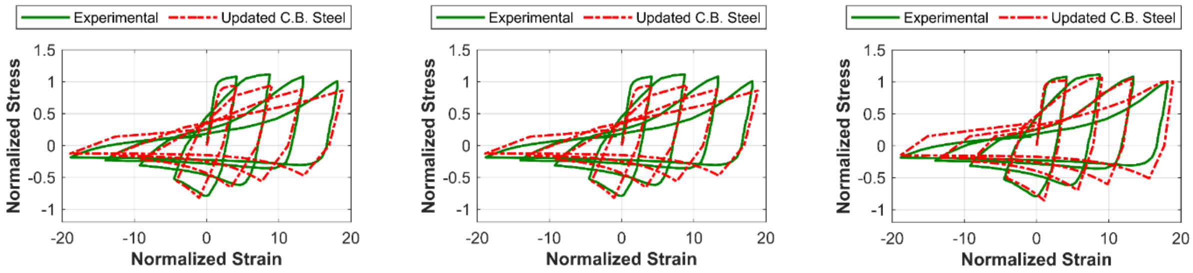

(a) (b) (c)

Figure 5-39: Stress-strain hysteresis comparison between the experiment and the calibrated *C.B Steel* using (a) SA with six parameters, (b) UKF with six parameters, and (c) UKF with three parameters for specimen #5

Based on the observation among the calibration results of *C.B Steel* at all five specimens, the modeling accuracy is poor for specimen #1-3, and an acceptable accuracy is achieved for specimen #4-5. It can be concluded that the *C.B Steel* material is able to provide an accurate representation of the stress-strain relationship in a relative high *L/D* ratio (i.e. larger than 10) in a specific application conditions (i.e. Kashani's material test). On the other hand, the parameter reduction is effective for the calibration in specimen #4-5 and can be implemented for certain cases.

5.2.2.5 Summary

In this section, three materials are calibrated corresponding to the cyclic stress-strain relationship obtained from five specimens in two experiments and the calibration accuracy in terms of *RRMSE* are listed in Table 5-24 below. To begin with, the *Steel4* material has proven to be the most versatile model, which could achieve a good match for reinforcing steel at a wide rang of *L/D* ratio. The disadvantage of the *Steel4* material, on the other hand, is that it requires more parameters to define its tension and compression envelope, which could potentially increase the total computational cost. Secondly, the *Reinforcing Steel* material with both GA and DM buckling model is capable of achieving a good performance for the specimen with slenderness ratio under 8 while the modeling accuracy is not as accurate for the specimen with a higher *L/D* ratio. Lastly, the *C.B Steel* material is not capable of modeling steel bars with low *L/D* ratio (i.e. less than 8) due to the bilinear formulation on the material and only capable of representing a certain type of steel rebars.

Table 5-24: Summary of the calibration results for all steel material model using UKF for the specimen #1 ~ #5

L/D	5	8	11	10	15
Steel4	0.194	**0.134**	**0.241**	**0.122**	0.361
R. Steel (GA)	0.145	0.141	0.330	0.407	0.644
R. Steel (DM)	**0.136**	0.138	0.311	0.413	0.608
C.B. Steel	0.348	0.334	0.352	0.175	**0.355**

5.3 FEMU on RC columns considering bond-slip and rebar buckling

5.3.1 Finite element modeling and model updating scheme

This section studies the tested full-scale RC bridge column considering buckling of steel rebars, in addition to bond-slip as studied in the previous chapter. In order to simulate the buckling behavior of the steel rebars, a buckling steel material model with asymmetrical behavior replaces the uniaxial *Steel02* material model in the fibers. By taking advantage of the performance assessment of four buckling steel material models in Section 5.2.2, the *Steel4* material model is adopted considering its ability of achieving a good correlation with the experimental data in a wide range of slenderness ratios.

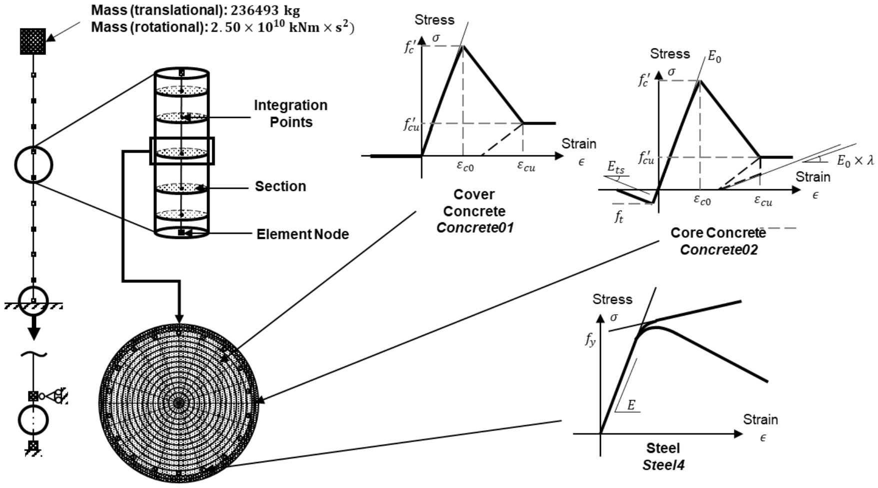

Figure 5-40: Schematic view for the FE model of the shake-table tested RC bridge pier column, with bond-slip and buckling effect considered

In the FE model of the shake-table tested RC bridge pier column considering bond-slip and rebar buckling (see Figure 5-40), other than the change in the steel material model used for the steel fibers, all the other modeling aspects remain the same as the previous model. Specifically, the *Concrete01* material model is used to represent the unconfined (cover) concrete in the column sections and in the zero-length section used to incorporate bond-slip effect. The *Concrete02* material model is assigned to the confined concrete fibers in the column sections and the zero-length section. In particular, in the zero-length section element, the *bond-SP01* material model is assigned to the steel fibers to consider bond-slip effect.

To simulate the column behavior, all the material models for concrete, steel, and zero-length section element to consider bond-slip are defined based on the estimates as described in Section 4.3, which are derived from the in-site measurements and the empirical estimation. The newly introduced *Steel4* material model is defined based on experimental and empirical values, which are the center values defined in Section 5.2.2. Specifically, parameters that has direct measurements or can be easily approximated based on the coupon test, such as f_y, E_0 and b_k/b_{kc}, are evaluated based on the test report provided by Schoettler et al. [52], while other parameters are defined in accordance of the work proposed by Mohammed et al. [83].

In order explore the possibility of using UKF to estimate the advanced modeling aspects for bond-slip and steel rebar buckling, nonlinear FEMU is performed to such an FE model using simulated seismic data. This model, assumed as the one with true parameters, is used to generate seismic data. In order to simulate the measurement error with moderate level of noise, an additive white Gaussian noise (AGWN) with a standard deviation of 3 mm is added into the displacement measurement. It is assumed that only the free-end displacement of the bridge pier column is recorded as the input for nonlinear FE model updating in this chapter. To consider the RC bridge column with various levels of steel rebar buckling, the five GMs (i.e. GM5. GM6, GM7, GM8 and GM9) in the shake-table testing program is used in this chapter.

In addition to the two material parameters, ε_c of the core concrete (*Concrete02*) and S_y for the bonding (*bond-SP01*), to account for the uncertain aspects of concrete and bond-slip, buckling steel related parameters are considered for FEMU. Among the six most sensitive parameters (f_y, b_{ic}, ρ_{ic}, R_{ic}, b_k and b_{kc}) identified from the sensitivity analysis results of *Steel4* material model, two of them (ρ_{ic}, R_{ic}) are selected since the three parameters (f_y, b_k and b_{kc}) can be relatively easily determined from experimental coupon tests and parameter b_{ic} is less significant for the buckling behavior (see Figure 5-34).

Parameter study in Section 3.5 provided a good reference on choosing the system parameter of the FEMU algorithm. As such, for the simulated data FEMU, the variance of the process noise matrix $\boldsymbol{Q}$ is taken as 1×10^{-10}, the variance for the measurement noise matrix $\boldsymbol{R}$ is taken as 1×10^{-6} and the coefficient of variation for the initial prediction of state vector $\boldsymbol{P}_0^{xx}$ is taken as 0.1, respectively.

5.3.2 Nonlinear FE model updating for GM5

Figure 5-41 shows the comparison of the FE-predicted and measured (true) drift ratio histories of the RC bridge pier column under GM5 before and after FEMU. The drift ratio history used as measurement was generated by contaminating the response simulated from the FE column model, with the true model parameters, subjected to the strong motion portion (e.g., 50-second acceleration series) of GM5. The UKF-based nonlinear FEMU framework is applied to the RC bridge column model to estimate the true model parameters, in which the initial model parameters considered (i.e., ε_c^{ini}) are chosen to be 80% of the true values (i.e., $\varepsilon_c^{ini} = 0.8\varepsilon_c^{True}$).

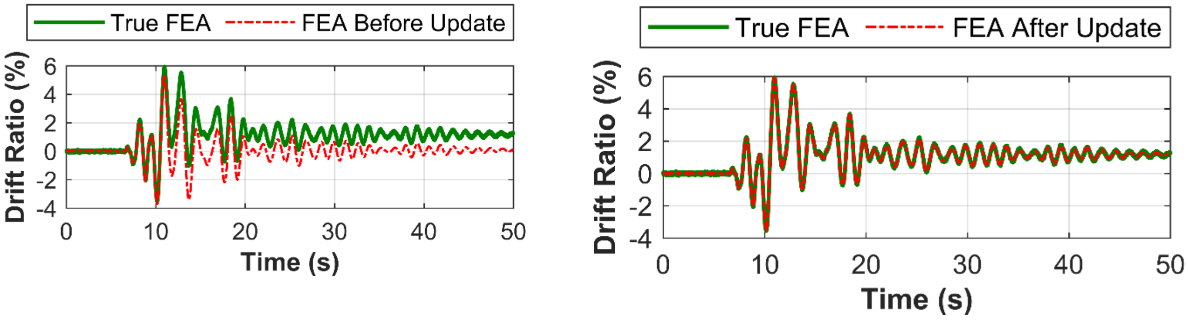

(a) (b)

Figure 5-41: Comparison of the FE-predicted and measured (true) drift ratio history of the RC bridge pier column under GM5: (a) before update, and (b) after update

It can be noticed that the discrepancy between the initial FE-prediction before update and the true response is remarkable, showing the significant effect of inaccurate model parameters (i.e., ε_c, ρ_{ic}, and R_{ic}). In contrast, the updated column model predicts the response well (see Figure 5-41 b), implying that UKF can estimate the true model parameters, as shown later by the modal parameter updating histories (see Figure 5-42).

In Figure 5-42, the model parameter updating histories, including the posterior mean estimate and the boundaries of the 95% confidence interval (i.e., mean ± 2 standard deviation), for all four model parameters considered. As shown in Figure 5-42 (a), (b) and (c), the first three parameters, ρ_{ic}, R_{ic} and ε_c, have converged approximately to the true values. The bond-slip parameter (S_y) is also converged, but to a relatively low value (5% smaller than true value), which is due to its lower sensitivity since a good match can be achieved using the estimated S_y for the drift ratio history.

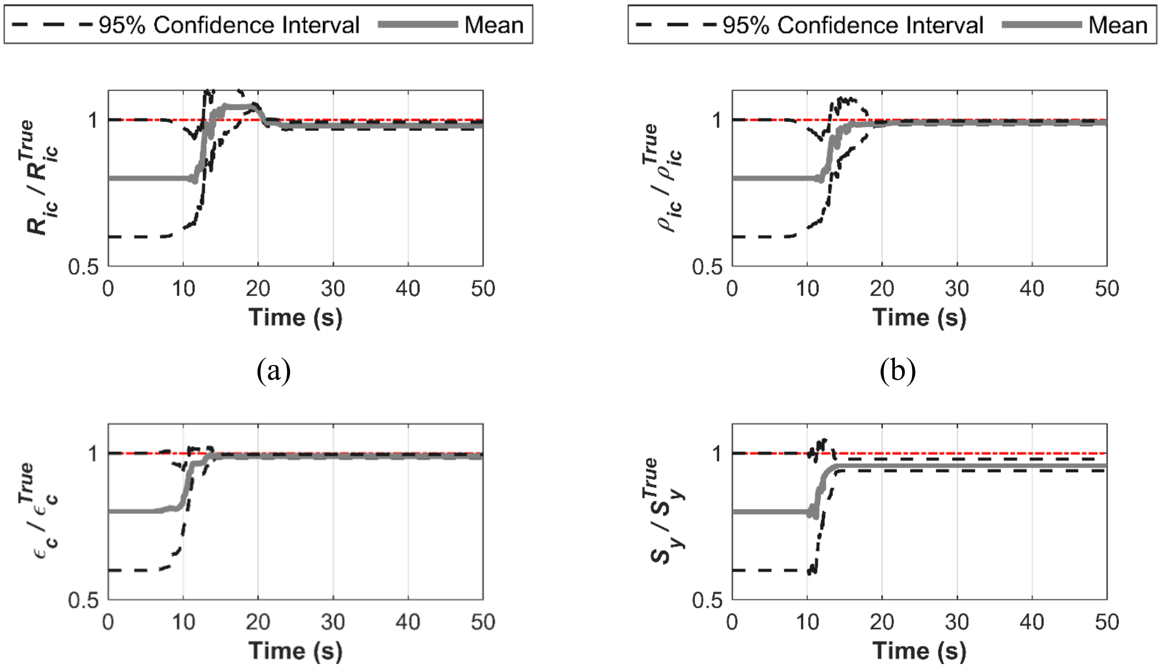

(a) (b)

(c) (d)

Figure 5-42: Model parameter updating histories under GM5 for: (a) ρ_{ic}, (b) R_{ic}, (c) ε_c, and (d) S_y, including the mean value and boundaries of the 95% confidence interval

In order to expose the importance of buckling effect, the stress-strain response for the most exterior steel rebars in the bottom section of the bridge column model is compared with the stress-strain relationship of steel without considering buckling, as shown in Figure 5-43 (a) and (b). It can be found that for both fibers, the softening on the negative side of the stress can be clearly observed, while the kinematic hardening on the positive side is also reduced. Such observations indicate that the buckling effect affect the structural local behavior of the RC column during GM5. The buckling effect is also affecting the global behavior as shown in Figure 5-43 (c), where the behavior of the column model with buckling is compared with the one without buckling.

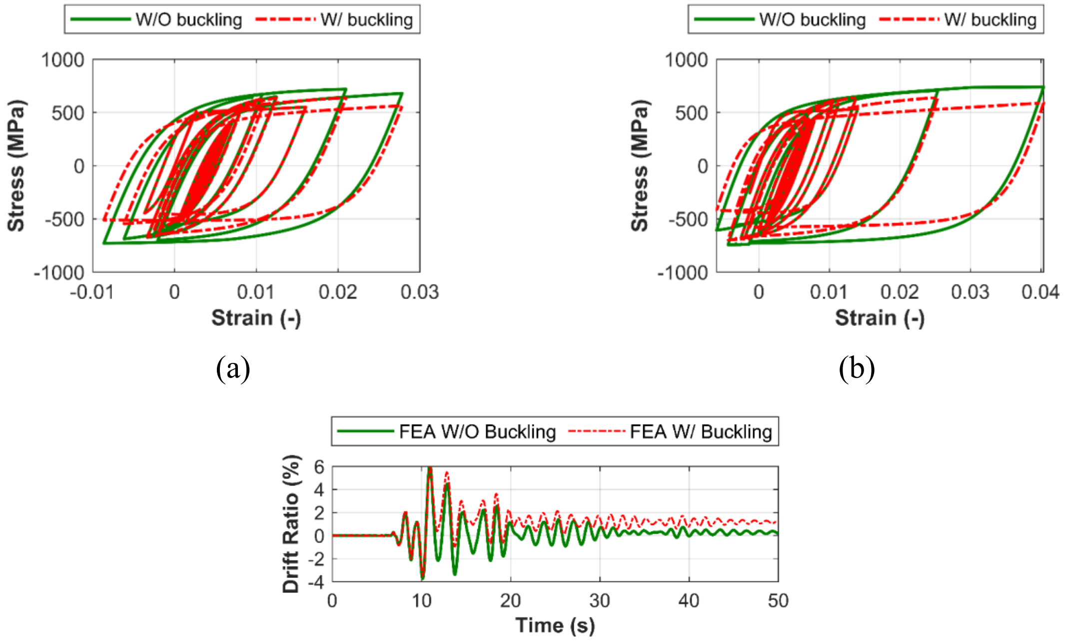

(a)

(b)

(c)

Figure 5-43: Comparison of the exterior steel rebars stress-strain response without and with buckling during GM5 on the: (a) left side, and (b) right side; and (c) the drift ratio comparison of the FE models with and without buckling

5.3.3 Nonlinear FE model updating for GM6

Figure 5-44 compares the FE-predicted and measured (true) drift ratio histories of the RC bridge pier column under GM6 before and after FEMU. The measured drift history was generated in the same way as the case for GM5, which is achieved by contaminating the response simulated from the FE model with an additive Gaussian white noise. To achieve a fair comparison among the different updating cases with different ground motions, similar initial guess of the model parameter values is considered as the FEMU case for GM5, i.e., 80% of the true value of each parameter. From Figure 5-44 (a), it can be noticed that the discrepancy between the initial FE-prediction before update and the measured response is non-negligible, showing the significant effect of inaccurate model parameters (i.e., ε_c, ρ_{ic}, R_{ic}, and S_y).

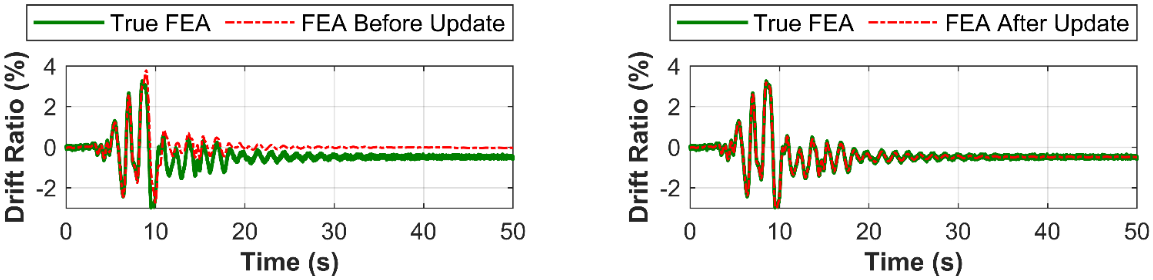

(a)

(b)

Figure 5-44: Comparison of the FE-predicted and measured (true) drift ratio history of the RC bridge pier column under GM6: (a) before update and (b) after update

The updated column model could accurately predict the response (see Figure 5-44 b) and an accurate parameter estimation can be observed from the parameter updating histories (see Figure 5-45), suggesting that the proposed FEMU framework have accurately estimated the true model parameters.

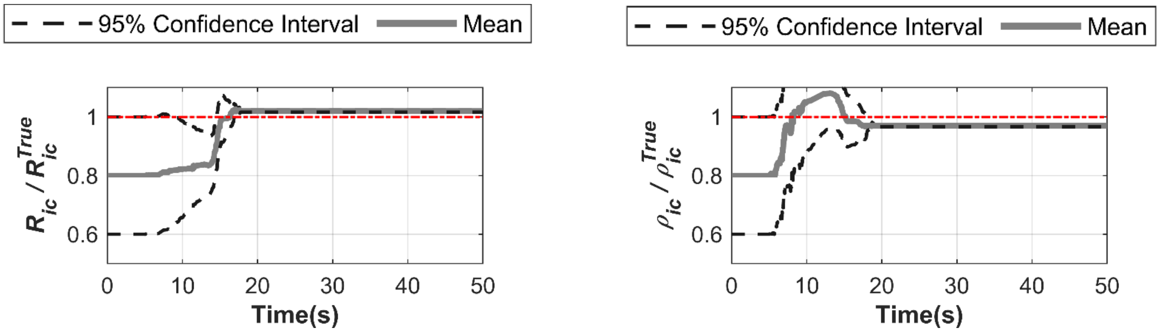

(a)

(b)

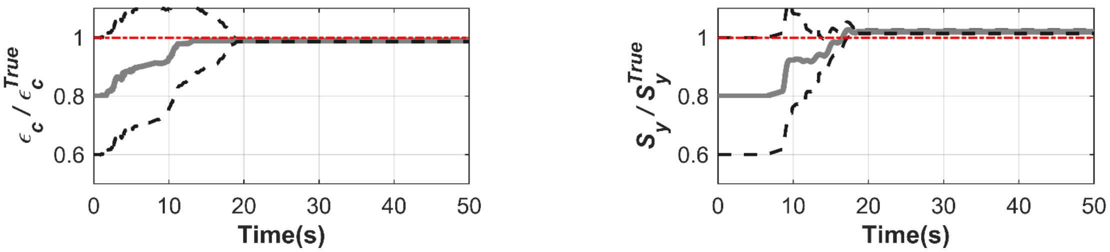

(c)

(d)

Figure 5-45: Model parameter updating histories in GM6 for: (a) ρ_{ic}, (b) R_{ic}, (c) ε_c, and (d) S_y

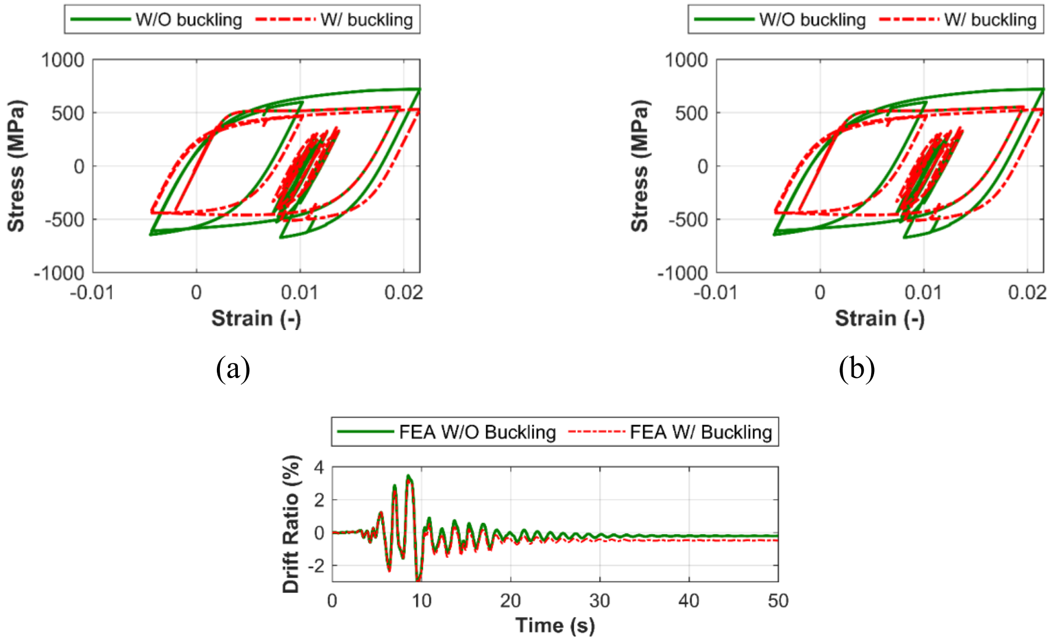

(a)

(b)

(c)

Figure 5-46: Comparison of the exterior steel rebars stress-strain response without and with buckling during GM6 on the: (a) left side, and (b) right side; and (c) the drift ratio comparison of the FE models with and without buckling

The stress-strain relationships of most exterior steel fibers are shown in Figure 5-46 (a) and (b), which shows a lower strain magnitude (-0.005 to +0.021) during GM6 compared to the case with GM5 (-0.01 to +0.03). Significant softening can be observed on the compression side. Compared to the previous case with GM5, the buckling effect on the global behavior is not as significant as the case with GM6 (see Figure 5-46 c), which is because of the lower intensity of.

5.3.4 Nonlinear FE model updating for GM7

Similarly, FEMU was conducted for the bridge column subjected to GM7. As the result of the difference in the initial guess and true model parameters, the FE-predicted drift history is different from the measured response as shown in Figure 5-47 (a).

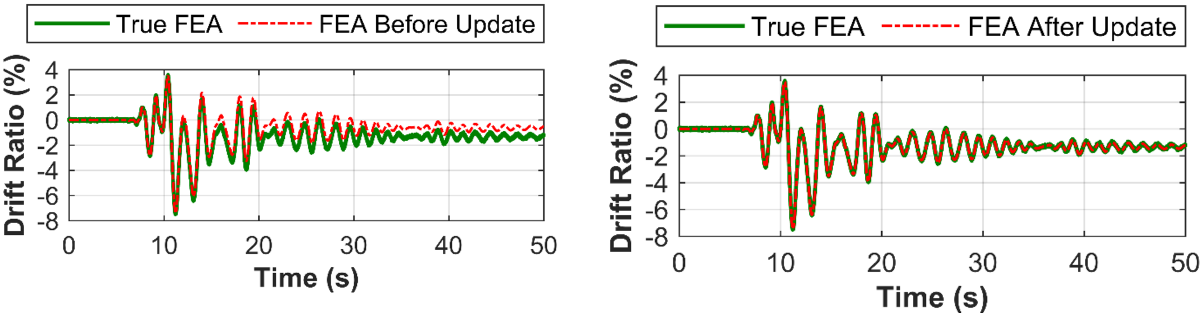

(a) (b)

Figure 5-47: Comparison of the FE-predicted and measured (true) drift ratio history of the RC bridge pier column under GM7: (a) before update and (b) after update

However, the FE-predicted drift history after FEMU shows a significant improvement. Moreover, the parameter updating histories (see Figure 5-48) showed a nearly perfect prediction for each of the four material model parameters considered.

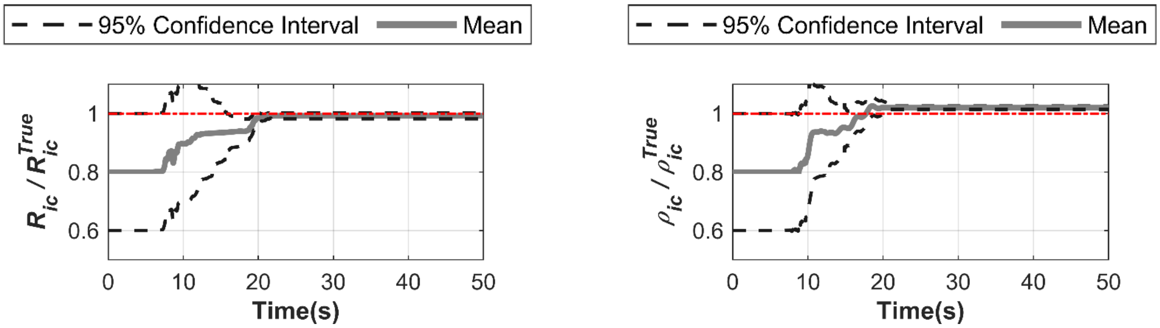

(a) (b)

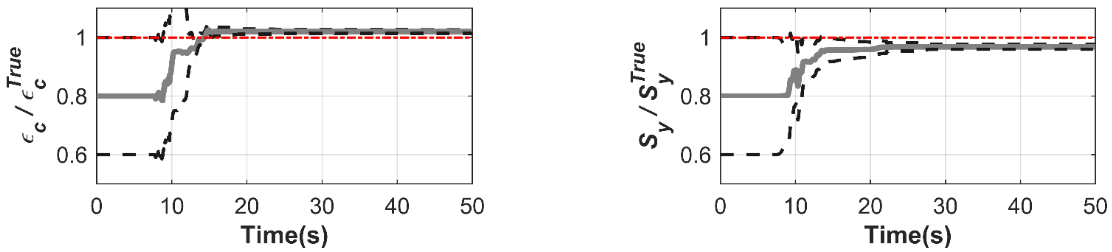

(c) (d)

Figure 5-48: Model parameter updating histories in GM7 for: (a) ρ_{ic}, (b) R_{ic}, (c) ε_c, and (d) S_y

Figure 5-49 (a) and (b) show the local stress-strain relationship for the most exterior steel fiber in the bottom section on the left and right side of the column, respectively, with comparison to the stress-strain relationship without considering buckling. The buckling effect shows a significant impact on the structural response in GM7.

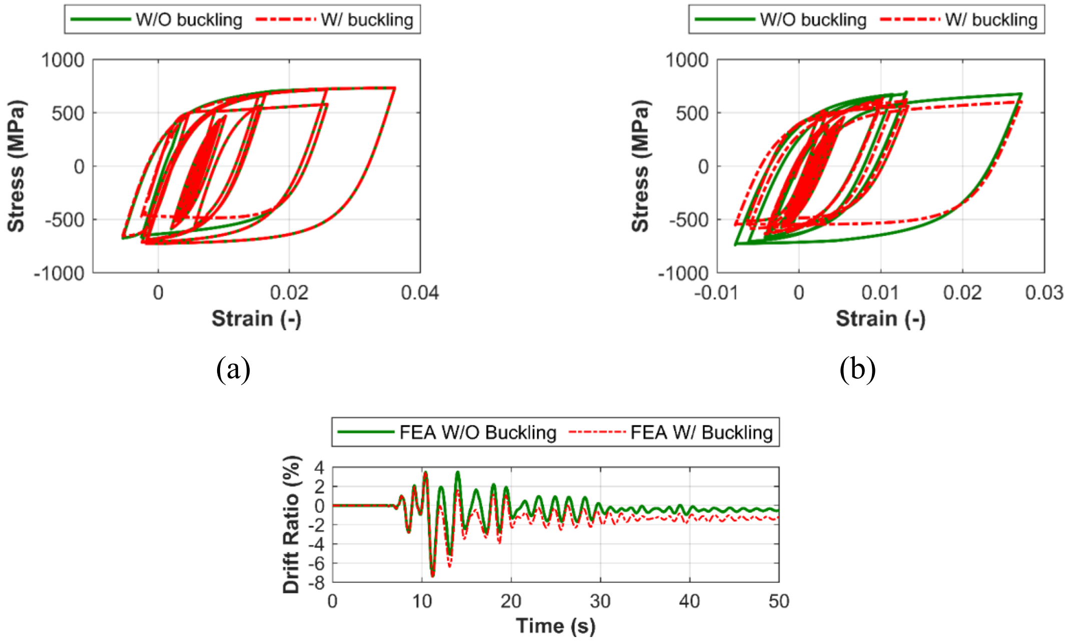

(a) (b)

(c)

Figure 5-49: Comparison of the exterior steel rebars stress-strain response without and with buckling during GM7 on the: (a) left side, and (b) right side; and (c) the drift ratio comparison of the FE models with and without buckling

Furthermore, it is worth noting that a significant softening due to buckling can be observed in Figure 5-49 (b), while the softening due to buckling is less for the steel rebars on the left side of the column. The difference in the drift histories obtained from the FE models with and without buckling effect (see Figure 5-49 c) is more significant compared to those in GM5 and GM6. This is due to the relatively higher intensity in GM7.

5.3.5 Nonlinear FE model updating for GM8 (or GM9)

Similarly, FEMU was conducted for the bridge column subjected to GM8 (or GM9), which is the same as GM8 but applied in the opposite direction) with a much higher intensity than GM7. A significant improvement can be observed on the FE-predicted drift history of the RC column after FEMU (see Figure 5-50).

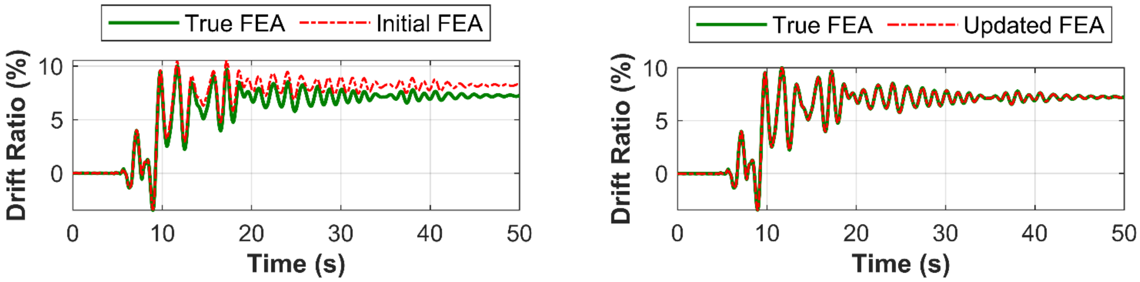

(a) (b)

Figure 5-50: Comparison of the FE-predicted and measured (true) drift ratio history of the RC bridge pier column under GM8 (or GM9): (a) before update, and (b) after update

The four material model parameters are successfully identified, as an accurate prediction for each of the four material model parameters considered can be observed in the parameter updating history as shown in Figure 5-51.

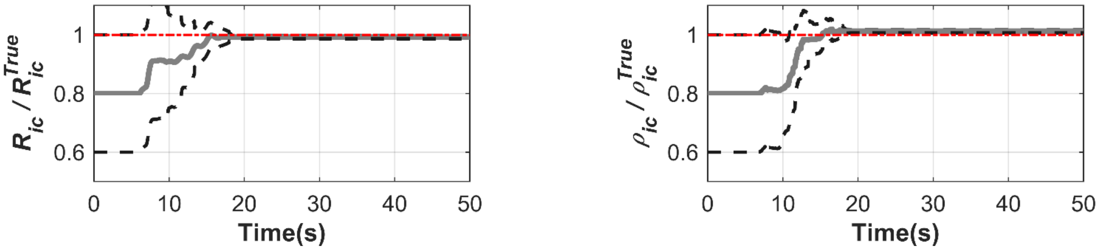

(a) (b)

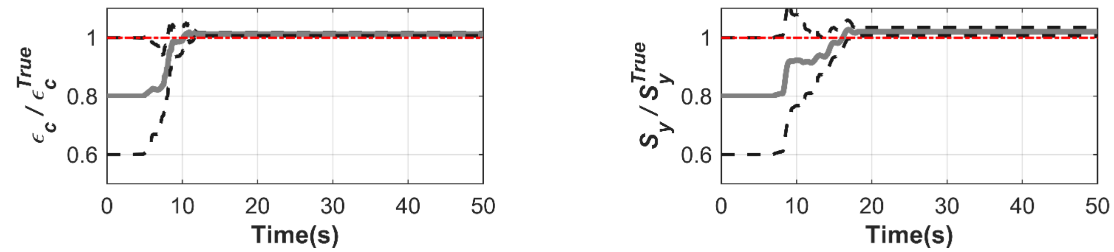

(c) (d)

Figure 5-51: Model parameter updating histories in GM8 (or GM9) for: (a) ρ_{ic}, (b) R_{ic}, (c) ε_c, and (d) S_y

The buckling effect also plays an important role at the local and global structural responses in GM8. Figure 5-52 (a) and (b) show the stress-strain relationship for the most exterior steel fiber in the bottom section on the left and right side of the column, respectively, with comparison to the stress-strain relationship without considering buckling.

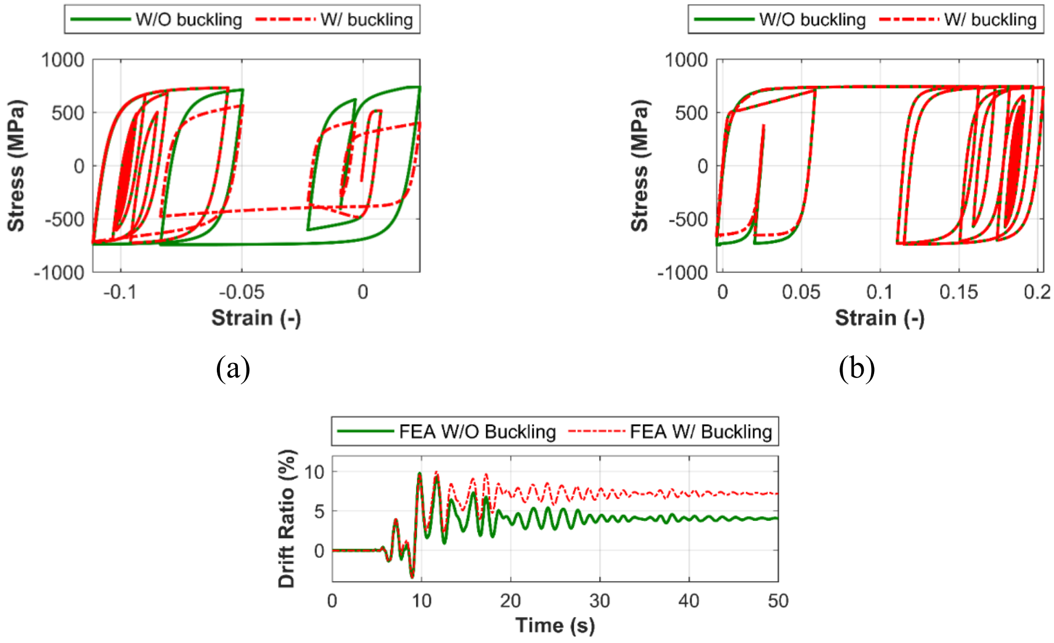

(a) (b)

(c)

Figure 5-52: Comparison of the exterior steel rebars stress-strain response without and with buckling during GM8 (or GM9) on the: (a) left side, and (b) right side; and (c) the drift ratio comparison of the FE models with and without buckling

In addition, it can be observed that inclusion of the buckling effect has resulted in significant difference in the stress-strain behavior of steel fiber on the left side of the column, but no significant effect on the behavior of steel fiber the right side of the column. The drift ratio history obtained from the FE model without buckling effect is significantly different from that predicted from the FE model with buckling (see Figure 5-52 c).

5.4 Summary

In this chapter, the modeling capabilities of four steel material models considering rebar buckling was studied in order to simulate the buckling effect well in the RC column. By taking advantage of the FEMU framework introduced in Chapter 3, the optimal performance of each material model in different conditions were compared. Specifically, the *Steel4* material model was capable of providing an accurate representation of the stress-strain relationship considering buckling effect of steel rebars with a wide range of *L/D* ratios; the *Reinforcing steel-GA* and *Reinforcing steel-DM* material model were proven to be effective for steel rebars with a low *L/D* ratio; and the *C.B. Steel* material model was only effective when representing the stress-strain relationship for steel bars with a relative high *L/D* ratio. Furthermore, the capability of the proposed FEMU framework on identifying the unknown parameters of RC column models considering bond-slip and steel rebar buckling (i.e., *Steel4* material model) was verified with a simulated data from GMs with varying intensities (e.g., GM5 ~ GM9). It was found that the FEMU framework successfully identified the unknown modeling parameters with high accuracy, proving the effectiveness of the FEMU framework in identifying advanced modeling parameters.

CHAPTER 6: CONCLUSIONS AND OUTLOOK

6.1 Summary

Developing an accurate finite element (FE) model is important for engineers to investigate the capacity of a newly designed structure and provide information regarding a damaged structure. The uncertainties involved in various modeling aspects have been one of the major obstacles in obtaining an accurate representation of mechanical behavior of a civil structure. In order to help engineers and researchers appropriately address the uncertainties in modeling, the widely used stochastic model updating approach (i.e., Bayesian inference) needs to be examined for nonlinear finite element model updating (FEMU) of complicated FE models (e.g., considering advanced modeling aspects) and based on experimental data.

To this end, a nonlinear FEMU framework was introduced by combining a stochastic filtering algorithm (unscented Kalman filter, UKF) and an open-source finite element analysis software (*OpenSees*). It was referred as UKF-based nonlinear FEMU framework in this thesis. The accuracy and efficiency of such a framework was first verified through a simple parameter identification example of a two-dimensional (2-D) frame model with elastic and nonlinear reinforced concrete (RC) element, together with in-depth examination of its robustness.

With the introduced FEMU framework, a nonlinear FE model was updated for a full-scale RC bridge column tested on a shake-table subjected to a sequence of earthquake ground motions (GMs) of varying intensity levels. It was found that in the tested RC bridge column, bond-slip effect played a significant role and was thus included in the nonlinear FE model. All modeling aspects, including the definitions for steel, concrete, and bond-slip, were initially determined in accordance with the in-site information and empirical models available from the literature. However, due to the uncertainties in the modeling parameters, the initial FE model was updated using the shake-table test data for the first four GMs in the test program. The updating parameters were wisely chosen by referring to in-site test reports and the knowledge obtained from the local sensitivity analysis performed in this study.

As revealed by the experimental testing of the bridge column, steel rebar buckling was another important phenomenon when the column was subjected to the remaining earthquake GMs with high intensities. To increase the modeling accuracy for the RC column under seismic loads with high intensities, the steel buckling effect was taken into account. To select the most appropriate and versatile model for steel considering rebar buckling, four existing buckling steel material models were assessed using material coupon tests. The material models were calibrated using UKF and simulated annealing, which is a global optimization algorithm. By incorporating the best buckling steel material model, the capability of the RC bridge column model was enhanced, and nonlinear FEMU was conducted for the bridge column with noisy simulated data for the other five GMs in the shake-table test program. It showed that the UKF-based nonlinear FEMU framework was able to estimate the unknown modeling aspects, including the bond-slip and buckling parameters.

6.2 Conclusions

The main conclusions of this research are outlined as follows:

1. To successfully apply UKF to system identification problems (e.g., nonlinear FEMU), the algorithm parameters should be chosen carefully, and some guidance were provided.
2. The zero-length section element approach proved effective to model the bond-slip effect for the RC bridge column subjected to GM1 in the test. Further analysis revealed that the zero-length section element increased the model capability or flexibility, and it played an important role in the dynamic behavior of the RC column considered.
3. The UKF-based nonlinear FEMU framework was proved capable of identifying the bond-slip parameters using simulated data. Its application to the tested RC column using experimental data showed that the nonlinear FEMU framework successfully decreased the discrepancy between the model prediction and the experiment measurement. The credibility of the updated model considering bond-slip was verified by its capability of tracking the damage evolution in the column subjected to a sequence of GMs. The predictability analysis examined the accuracy of the updated models for future GMs, and it showed the role of the FEMU algorithm on predicting the future response based on historical information. This implied its potential application to structural health monitoring and damage assessment.

4. The performance assessment of four buckling steel material models showed that the *Steel4* material model outperformed other three models considered in terms of the versatilities. *Steel4* was considered as the most robust and accurate material model for representing the buckling effect at medium to low strain levels. The nonlinear FEMU for the bridge column considering both buckling and bond-slip using simulated data showed that it was capable of identifying parameters related to the advanced modeling aspects.

6.3 Recommendations for future work

This section describes the limitation in the presented work, and recommendations for future work are suggested as follows:

1. For the tested bridge column, the GMs were applied in a sequential manner during the shake-table test. Nevertheless, nonlinear FEMU presented in this work was performed for each GM separately using the experimental measurement, which means that the historical damage in the column due to earlier earthquakes is not taken in account. This limits the accuracy of the model prediction, and thus the accuracy of separate FEMU is degraded. Therefore, a sequential FEMU using all the measurements during multiple GMs is recommended in the future, but it will require extensive computational resource.
2. Although the FE model developed for the RC bridge column considered advanced modeling aspects such as bond-slip and steel rebar buckling, the shear flexibility was neglected. However, the test results showed that the shear deformation in this column also contributed to the pier top drift. Thus, to further enhance the capability of the FE model developed for the bridge column, shear flexibility needs to be incorporated, and UKF-based nonlinear FEMU can be further used to explore this modeling aspect.
3. The performance assessment of the steel material models considering rebar buckling are based on the measurements from only five cyclic tests of steel rebar coupons available in the literature. Thus, accuracy of the available buckling steel material models needs more steel rebar coupon tests. Additionally, there is need for further development of buckling steel material models appropriate for a wide range of slenderness ratios and high strain levels.
4. The nonlinear FEMU of the RC column considering bond-slip and steel rebar buckling was performed based noisy simulated data. Experimental data should be used to further verify the capability of UKF-based nonlinear FEMU.

REFERENCES

[1] Q. Han, X. Du, J. Liu, Z. Li, L. Li, and J. Zhao, “Seismic damage of highway bridges during the 2008 Wenchuan earthquake,” *Earthq. Eng. Eng. Vib.*, vol. 8, no. 2, pp. 263–273, 2009.

[2] K. Kawashima and S. Unjoh, “The damage of highway bridges in the 1995 Hyogo-ken nanbu earthquake and its impact on Japanese seismic design,” *J. Earthq. Eng.*, vol. 1, no. 03, pp. 505–541, 1997.

[3] Y. T. Hsu and C. C. Fu, “Seismic effect on highway bridges in Chi Chi earthquake,” *J. Perform. Constr. Facil.*, vol. 18, no. 1, pp. 47–53, 2004.

[4] M. J. N. Priestley, F. Seible, and G. M. Calvi, *Seismic design and retrofit of bridges*. John Wiley & Sons, 1996.

[5] D. L. Anderson, D. Mitchell, and R. G. Tinawi, “Performance of concrete bridges during the Hyogo-ken Nanbu (Kobe) earthquake on January 17, 1995,” *Can. J. Civ. Eng.*, vol. 23, no. 3, pp. 714–726, 1996.

[6] G. H. Siqueira, A. S. Sanda, P. Paultre, and J. E. Padgett, “Fragility curves for isolated bridges in eastern Canada using experimental results,” *Eng. Struct.*, vol. 74, pp. 311–324, 2014.

[7] F. McKenna, “OpenSees: a framework for earthquake engineering simulation,” *Comput. Sci. Eng.*, vol. 13, no. 4, pp. 58–66, 2011.

[8] G. Zhao, M. Zhang, Y. Li, and D. Li, “The hysteresis performance and restoring force model for corroded reinforced concrete frame columns,” *J. Eng.*, vol. 2016, 2016.

[9] C. E. Majorana, V. A. Salomoni, G. Mazzucco, and G. A. Khoury, “An approach for modelling concrete spalling in finite strains,” *Math. Comput. Simul.*, vol. 80, no. 8, pp. 1694–1712, 2010.

[10] X. Cao, L. Wu, and Z. Li, “Behaviour of steel-reinforced concrete columns under combined torsion based on ABAQUS FEA,” *Eng. Struct.*, vol. 209, p. 109980, 2020.

[11] S. A. Kaba and S. A. Mahin, *Refined modelling of reinforced concrete columns for seismic analysis*. University of California, Earthquake Engineering Research Center, 1984.

[12] M. S. Zadeh and M. S. Saiidi, "Pre-test analytical studies of NEESR-SG 4-span bridge model using OpenSees," *Rep. No. CCEER-07*, vol. 3, 2007.

[13] W. K. Lee and S. L. Billington, "Modeling residual displacements of concrete bridge columns under earthquake loads using fiber elements," *J. Bridg. Eng.*, vol. 15, no. 3, pp. 240–249, 2010.

[14] B. D. Scott, R. Park, and M. J. N. Priestley, "Stress-strain behavior of concrete confined by overlapping hoops at low and high strain rates," in *Journal Proceedings*, 1982, vol. 79, no. 1, pp. 13–27.

[15] I. D. Karsan and J. O. Jirsa, "Behavior of concrete under compressive loadings," *J. Struct. Div.*, 1969.

[16] M. Hisham and M. Yassin, "Nonlinear analysis of prestressed concrete structures under monotonic and cycling loads," *Univ. California, Berkeley. Ph. D. thesis*, 1994.

[17] J. B. Mander, M. J. N. Priestley, and R. Park, "Theoretical stress-strain model for confined concrete," *J. Struct. Eng.*, vol. 114, no. 8, pp. 1804–1826, 1988.

[18] J. B. Mander, M. J. N. Priestley, and R. Park, "Observed stress-strain behavior of confined concrete," *J. Struct. Eng.*, vol. 114, no. 8, pp. 1827–1849, 1988.

[19] A. Giuffrè, "Il comportamento del cemento armato per sollecitazioni cicliche di forte intensità," *G. del Genio Civ.*, 1970.

[20] M. Menegotto, "Method of analysis for cyclically loaded RC plane frames including changes in geometry and non-elastic behavior of elements under combined normal force and bending," in *Proc. of IABSE symposium on resistance and ultimate deformability of structures acted on by well defined repeated loads*, 1973, pp. 15–22.

[21] W. Ramberg and W. R. Osgood, "Description of stress-strain curves by three parameters," 1943.

[22] Y. F. Dafalias and E. P. Popov, "A model of nonlinearly hardening materials for complex loading," *Acta Mech.*, vol. 21, no. 3, pp. 173–192, 1975.

[23] F. C. Filippou, E. P. Popov, and V. V. Bertero, "Effects of bond deterioration on hysteretic behavior of reinforced concrete joints," 1983.

[24] G. Monti and C. Nuti, "Nonlinear cyclic behavior of reinforcing bars including buckling," *J. Struct. Eng.*, vol. 118, no. 12, pp. 3268–3284, 1992.

[25] M. M. Kashani, L. N. Lowes, A. J. Crewe, and N. A. Alexander, "Nonlinear fibre element modelling of RC bridge piers considering inelastic buckling of reinforcement," *Eng. Struct.*, vol. 116, pp. 163–177, 2016.

[26] M. M. Kashani, A. J. Crewe, and N. A. Alexander, "Nonlinear cyclic response of corrosion-damaged reinforcing bars with the effect of buckling," *Constr. Build. Mater.*, vol. 41, pp. 388–400, 2013.

[27] A. Ayoub, "Nonlinear analysis of reinforced concrete beam--columns with bond-slip," *J. Eng. Mech.*, vol. 132, no. 11, pp. 1177–1186, 2006.

[28] D. Ngo and A. C. Scordelis, "Finite element analysis of reinforced concrete beams," in *Journal Proceedings*, 1967, vol. 64, no. 3, pp. 152–163.

[29] R. Eligehausen, E. P. Popov, and V. V Bertero, "Local bond stress-slip relationships of deformed bars under generalized excitations," 1982.

[30] G. Monti and E. Spacone, "Reinforced concrete fiber beam element with bond-slip," *J. Struct. Eng.*, vol. 126, no. 6, pp. 654–661, 2000.

[31] J. Zhao and S. Sritharan, "Modeling of strain penetration effects in fiber-based analysis of reinforced concrete structures," *ACI Struct. J.*, vol. 104, no. 2, p. 133, 2007.

[32] R. Astroza, A. Alessandri, and J. P. Conte, “A dual adaptive filtering approach for nonlinear finite element model updating accounting for modeling uncertainty,” *Mech. Syst. Signal Process.*, vol. 115, pp. 782–800, 2019.

[33] J. R. Sampson, “Adaptation in natural and artificial systems (John H. Holland).” Society for Industrial and Applied Mathematics, 1976.

[34] S. Kirkpatrick, C. D. Gelatt, and M. P. Vecchi, “Optimization by simulated annealing,” *Science (80-.).*, vol. 220, no. 4598, pp. 671–680, 1983.

[35] E. Asgarieh, B. Moaveni, and A. Stavridis, “Nonlinear finite element model updating of an infilled frame based on identified time-varying modal parameters during an earthquake,” *J. Sound Vib.*, vol. 333, no. 23, pp. 6057–6073, 2014.

[36] A. Teughels and G. De Roeck, “Structural damage identification of the highway bridge Z24 by FE model updating,” *J. Sound Vib.*, vol. 278, no. 3, pp. 589–610, 2004.

[37] P. G. Bakir, E. Reynders, and G. De Roeck, “An improved finite element model updating method by the global optimization technique ‘Coupled Local Minimizers,’” *Comput. Struct.*, vol. 86, no. 11–12, pp. 1339–1352, 2008.

[38] R. Jafarkhani and S. F. Masri, “Finite element model updating using evolutionary strategy for damage detection,” *Comput. Civ. Infrastruct. Eng.*, vol. 26, no. 3, pp. 207–224, 2011.

[39] B. Jaishi and W.-X. Ren, “Structural finite element model updating using ambient vibration test results,” *J. Struct. Eng.*, vol. 131, no. 4, pp. 617–628, 2005.

[40] R. E. Kalman, “A new approach to linear filtering and prediction problems,” 1960.

[41] M. Hoshiya and E. Saito, “Structural identification by extended Kalman filter,” *J. Eng. Mech.*, vol. 110, no. 12, pp. 1757–1770, 1984.

[42] E. A. Wan and R. Van Der Merwe, “The unscented Kalman filter for nonlinear estimation,” in *Proceedings of the IEEE 2000 Adaptive Systems for Signal Processing, Communications,*

and Control Symposium (Cat. No. 00EX373), 2000, pp. 153–158.

[43] E. N. Chatzi and A. W. Smyth, "Particle filter scheme with mutation for the estimation of time-invariant parameters in structural health monitoring applications," *Struct. Control Heal. Monit.*, vol. 20, no. 7, pp. 1081–1095, 2013.

[44] S. Xue, H. Tang, and Q. Xie, "Structural damage detection using auxiliary particle filtering method," *Struct. Heal. Monit.*, vol. 8, no. 2, pp. 101–112, 2009.

[45] K. Foun, "Identification of civil structural parameters using the extended Kalman filter," Massachusetts Institute of Technology, 2009.

[46] S. Sen and B. Bhattacharya, "Online structural damage identification technique using constrained dual extended Kalman filter," *Struct. Control Heal. Monit.*, vol. 24, no. 9, p. e1961, 2017.

[47] Z. Xie and J. Feng, "Real-time nonlinear structural system identification via iterated unscented Kalman filter," *Mech. Syst. Signal Process.*, vol. 28, pp. 309–322, 2012.

[48] H. Ebrahimian, R. Astroza, J. P. Conte, and R. A. de Callafon, "Nonlinear finite element model updating for damage identification of civil structures using batch Bayesian estimation," *Mech. Syst. Signal Process.*, vol. 84, pp. 194–222, 2017.

[49] R. Astroza, H. Ebrahimian, and J. P. Conte, "Material parameter identification in distributed plasticity FE models of frame-type structures using nonlinear stochastic filtering," *J. Eng. Mech.*, vol. 141, no. 5, p. 4014149, 2015.

[50] M. K. Ramancha, R. Madarshahian, R. Astroza, and J. P. Conte, "Non-unique Estimates in Material Parameter Identification of Nonlinear FE Models Governed by Multiaxial Material Models Using Unscented Kalman Filtering," in *Model Validation and Uncertainty Quantification, Volume 3*, Springer, 2020, pp. 257–265.

[51] S. Konatowski, P. Kaniewski, and J. Matuszewski, "Comparison of estimation accuracy of EKF, UKF and PF filters," *Annu. Navig.*, vol. 23, no. 1, pp. 69–87, 2016.

[52] M. Schoettler, J. Restrepo, G. Guerrini, D. E. Duck, and others, “A full-scale, single-column bridge bent tested by shake-table excitation,” 2012.

[53] X. Chen, Z. Guan, J. Li, and B. F. Spencer Jr, “Shake table tests of tall-pier bridges to evaluate seismic performance,” *J. Bridg. Eng.*, vol. 23, no. 9, p. 4018058, 2018.

[54] N. Johnson, R. T. Ranf, M. S. Saiidi, D. Sanders, and M. Eberhard, “Seismic testing of a two-span reinforced concrete bridge,” *J. Bridg. Eng.*, vol. 13, no. 2, pp. 173–182, 2008.

[55] M. S. Saiidi, A. Vosooghi, H. Choi, and P. Somerville, “Shake table studies and analysis of a two-span RC bridge model subjected to a fault rupture,” *J. Bridg. Eng.*, vol. 19, no. 8, p. A4014003, 2014.

[56] P. N. Laplace, D. Sanders, M. S. Saiidi, and B. Douglas, “Shake table testing of flexure dominated reinforced concrete bridge columns,” University of Nevada, Reno, 1999.

[57] K. Kawashima *et al.*, “Shake table experiment on RC bridge columns using E-Defense,” *Proc. 41st Panel Wind Seism. Eff. UJNR, Public Work. Res. Institute, Tsukuba Sci. City, Japan*, 2009.

[58] F. Bianchi, R. Sousa, and R. Pinho, “Blind prediction of a full-scale RC bridge column tested under dynamic conditions,” 2011.

[59] R. Sousa, A. A. Correia, J. P. Almeida, and R. Pinho, “Blind prediction tests as a benchmark to improve the seismic response of fibre models,” 2014.

[60] N. Vila-Pouca, A. Monteiro, A. Arêde, P. Delgado, and R. Delgado, “Numerical simulation of bridge piers’ seismic behavior: A blind prediction methodology,” *Earthq. Eng. Eng. Vib.*, vol. 5, no. 1, pp. 119–131, 2006.

[61] E. N. Chatzi and A. W. Smyth, “The unscented Kalman filter and particle filter methods for nonlinear structural system identification with non-collocated heterogeneous sensing,” *Struct. Control Heal. Monit.*, vol. 16, pp. 99–123, 2009, doi: 10.1002/stc.

[62] C. B. Yun and M. Shinozuka, “Identification of Nonlinear Structural Dynamic Systems,” *J. Struct. Mech.*, vol. 8, no. 2, pp. 187–203, 1980, doi: 10.1080/03601218008907359.

[63] S. H. Cheung and J. L. Beck, “Bayesian model updating using hybrid Monte Carlo simulation with application to structural dynamic models with many uncertain parameters,” *J. Eng. Mech.*, vol. 135, no. 4, pp. 243–255, 2009.

[64] J. Castiglione, R. Astroza, S. E. Azam, and D. Linzell, “Auto-regressive model based input and parameter estimation for nonlinear finite element models,” *Mech. Syst. Signal Process.*, vol. 143, p. 106779, 2020.

[65] R. Astroza, H. Ebrahimian, Y. Li, and J. P. Conte, “Bayesian nonlinear structural FE model and seismic input identification for damage assessment of civil structures,” *Mech. Syst. Signal Process.*, vol. 93, pp. 661–687, 2017.

[66] M. S. Arulampalam, S. Maskell, N. Gordon, and T. Clapp, “A tutorial on particle filters for online nonlinear/non-Gaussian Bayesian tracking,” *IEEE Trans. signal Process.*, vol. 50, no. 2, pp. 174–188, 2002.

[67] A. J. Haug, “A tutorial on Bayesian estimation and tracking techniques applicable to nonlinear and non-Gaussian processes,” *MITRE Corp. McLean*, 2005.

[68] C. D. of Transportation (Caltrans), “Caltrans seismic design criteria.” Caltrans Sacramento, CA, 2006.

[69] M. Kwon and E. Spacone, “Three-dimensional finite element analyses of reinforced concrete columns,” *Comput. Struct.*, vol. 80, no. 2, pp. 199–212, 2002.

[70] M. P. Berry and M. O. Eberhard, *Performance modeling strategies for modern reinforced concrete bridge columns*, vol. 67, no. 11. 2006.

[71] B. Ellingwood, *Development of a probability based load criterion for American National Standard A58: Building code requirements for minimum design loads in buildings and other structures*, vol. 13. US Department of Commerce, National Bureau of Standards, 1980.

[72] S. A. Mirza and J. G. MacGregor, “Probabilistic study of strength of reinforced concrete members,” *Can. J. Civ. Eng.*, vol. 9, no. 3, pp. 431–448, 1982.

[73] P. Geyskens, A. Der Kiureghian, and P. Monteiro, “Bayesian prediction of elastic modulus of concrete,” *J. Struct. Eng.*, vol. 124, no. 1, pp. 89–95, 1998.

[74] E. Musselman, S. Gross, H. Nassif, and others, “SP-284: Andy Scanlon Symposium on Serviceability and Safety of Concrete Structures: From Research to Practice,” *Spec. Publ.*, vol. 284, 2012.

[75] S. T. Mau and M. El-Mabsout, “Inelastic buckling of reinforcing bars,” *J. Eng. Mech.*, vol. 115, no. 1, pp. 1–17, 1989.

[76] M. E. Rodriguez, J. C. Botero, and J. Villa, “Cyclic stress-strain behavior of reinforcing steel including effect of buckling,” *J. Struct. Eng.*, vol. 125, no. 6, pp. 605–612, 1999.

[77] C. R. Urmson and J. B. Mander, “Local buckling analysis of longitudinal reinforcing bars,” *J. Struct. Eng.*, vol. 138, no. 1, pp. 62–71, 2012.

[78] Z. Zong, S. Kunnath, and G. Monti, “Simulation of reinforcing bar buckling in circular reinforced concrete columns,” *ACI Struct. J.*, vol. 110, no. 4, p. 607, 2013.

[79] R. I. Levin and N. A. J. Lieven, “Dynamic finite element model updating using simulated annealing and genetic algorithms,” *Mech. Syst. Signal Process.*, vol. 12, no. 1, pp. 91–120, 1998.

[80] M. M. Kashani, L. N. Lowes, A. J. Crewe, and N. A. Alexander, “Phenomenological hysteretic model for corroded reinforcing bars including inelastic buckling and low-cycle fatigue degradation,” *Comput. Struct.*, vol. 156, pp. 58–71, 2015.

[81] G. Monti and C. Nuti, “Analytical Model of Cyclic Behaviour of Reinforcing Bars with Inelastic Buckling,” 1991.

[82] G. Monti and C. Nuti, “Modellazione del comportamento ciclico di barre in acciaio per

armature di elementi in cemento armato," *Report No. 1/90*. Department of Structural Engineering Rome,, Italy, 1989.

[83] M. A. Mohammed and A. R. Barbosa, "Numerical Modeling Strategy for the Simulation of Nonlinear Response of Slender Reinforced Concrete Structural Walls," *Comput. Model. Eng. Sci.*, vol. 120, no. 3, pp. 583–627, 2019.

[84] A. Gomes and J. Appleton, "Nonlinear cyclic stress-strain relationship of reinforcing bars including buckling," *Eng. Struct.*, vol. 19, no. 10, pp. 822–826, 1997.

[85] R. P. Dhakal and K. Maekawa, "Modeling for postyield buckling of reinforcement," *J. Struct. Eng.*, vol. 128, no. 9, pp. 1139–1147, 2002.